1-1-2004

Opto-VLSI based WDM multifunction device

Selam T. Ahderom
Edith Cowan University

Edith Cowan University

Copyright Warning

Opto-VLSI based WDM Multifunction Device

By

Selam Techeste Ahderom

A thesis submitted for the degree of

Doctor of Philosophy

at

School of Engineering and Mathematics

Edith Cowan University

Principal Supervisor : Prof. Kamran Eshraghian

Co-Supervisor : A/Prof. Kamal Alameh

June 2004

USE OF THESIS

The Use of Thesis statement is not included in this version of the thesis.

DECLARATION

I certify that this thesis does not, to the best of my knowledge and belief:

(i) incorporate without acknowledgement any material previously submitted for a degree or diploma in any institution of higher education;

(ii) contain any material previously published or written by another person except where due reference is made in the text; or

(iii) contain any defamatory material.

Signature .

To Debbie, Yamina and Maryam

Publications

Refereed Journal Articles

S. Ahderom, M. Raisi, K. E. Alameh, and K. Eshraghian. Dynamic WDM equalizer using Opto-VLSI Beam Processing. *IEEE Photonics Technology Letters,* vol. 15, no. 11, pages 1603-1605, Nov. 2003.

M. Raisi, **S. Ahderom,** K. E. Alameh, and K. Eshraghian. Opto-VLSI multiband tunable optical filter. *IEE Electronics Letters,* vol. 39, no. 21, pages 1533-1535, October 2003.

Refereed Conference Papers

S. Ahderom, M. Raisi, K. Lo, K.E. Alameh, and R. Mavaddat. Applications of Liquid Crystal Spatial Light Modulators in Optical Communications. In *Proceedings of the IEEE 5th International Conf. on High-speed Networks and Multimedia Communications, HSNMC'02,* pages 239-242, Korea, July 2002.

S. Ahderom, M. Raisi, K. E. Alameh, and K. Eshraghian. High-resolution Dynamic WDM Equalization Using Opto-VLSI Beam Processing. In *Proceedings of the 7th World Multiconference on Systemics, Cybernetics and Informatics SCI 2003,* pages 179-183, USA, August 2003.

K. E. Alameh, K. Eshraghian, **S. Ahderom** and M. Raisi. Impact of EDFA Gain Fluctuations on the Response of Opto-VLSI based Reconfigurable Photonic RF Filters. In *Proceedings of the 7th World Multiconference on Systemics, Cybernetics and Informatics SCI 2003,* pages 184-188, USA, August 2003 .

K. E. Alameh, K. Eshraghian, **S. Ahderom** and M. Raisi. Opto-VLSI-based Reconfigurable Photonic RF Bandpass Filters Tunable Optical Filters Employing Opto-VLSI Processors. In *Proceedings of the International Conference on Computer, Communication and Control Technologies CCCT 2003,* pages 49-54, Orlando, Fl., USA July 2003.

M. Raisi, **S. Ahderom,** K. E. Alameh, and K. Eshraghian. Tunable Optical Filters Employing Opto-VLSI Processors. In *Proceedings of the International Conference on Computer, Communication and Control Technologies CCCT 2003,* pages 29-34, Orlando, Fl., USA, July 2003.

M. Raisi, **S. Ahderom,** K. Alameh, K. Eshraghian. Microphotonic optical filters. Accepted for publication in *Proceedings of the SPIE,* Dec. 2003.

K. Alameh, A. Bouzerdoum, K. Eshraghian, **S. Ahderom,** M. Raisi. Microphotonic interference mitigation filter for radio astronomy telescopes. Accepted for publication in *Proceedings of the SPIE,* Dec. 2003.

S. T. Ahderom, Mehrdad Raisi, Kamal Alameh, and Kamran Eshraghian. Testing and Analysis of Computer Generated Holograms for MicroPhotonic Devices. In *Proceedings of the IEEE International Workshop on Electronic Design, Test and Applications DELTA 2004,* pages 47-52, Australia, January 2004.

Mehrdad Raisi, **Selam Ahderom,** Kamal E. Alameh, and Kamran Eshraghian. Dynamic MicroPhotonic WDM Equalizer. In *Proceedings of the IEEE International Workshop on Electronic Design, Test and Applications DELTA 2004,* pages 59-62, Australia, January 2004.

Kamal E. Alameh, Kamran Eshraghian, **Selam Ahderom,** Mehrdad Raisi, Mike Myung-Ok Lee, and Rainer Michalzik. Integrated MicroPhotonic Broadband Smart Antenna Beamformer. In *Proceedings of the IEEE International Workshop on Electronic Design, Test and Applications DELTA 2004,* pages 208-212, Australia, January 2004.

K. Alameh, A. Bouzerdoum, **S. Ahderom,** M. Raisi, K. Eshraghian, X. Zhao, R. Zheng, Z. Wang. Integrated MicroPhotonic Wideband RF Interference Mitigation Filter. In *Proceedings of the IEEE International Workshop on Electronic Design, Test and Applications DELTA 2004,* pages 387-390, Australia, January 2004.

Kamal E. Alameh, **Selam Ahderom,** Mehrdad Raisi, and Kamran Eshraghian. MicroPhotonic Reconfigurable RF Signal Processor. In *Proceedings of the IEEE International Workshop on Electronic Design, Test and Applications DELTA 2004,* pages 63-67, Australia, January 2004.

Mehrdad Raisi, **Selam Ahderom,** Kamal E. Alameh, and Kamran Eshraghian. Multiband MicroPhotonic Tunable Optical Filter. In *Proceedings of the IEEE International*

Workshop on Electronic Design, Test and Applications DELTA 2004, pages 391-394, Australia, January 2004.

Selam Ahderom, Mehrdad Raisi, Kamal E. Alameh, and Kamran Eshraghian. Reconfigurable MicroPhotonic Add/Drop Multiplexer Architecture. In *Proceedings of the IEEE International Workshop on Electronic Design, Test and Applications DELTA 2004,* pages 203-207, Australia, January 2004.

Z. Wang, K. Alameh, **S. Ahderom,** R. Zheng, M. Raisi, K. Eshraghian. Novel Optical Router for MicroPhotonic switch. In *Proceedings of the IEEE International Workshop on Electronic Design, Test and Applications DELTA 2004,* pages 213-216, Australia, January 2004.

Other Conference Presentations

S. Ahderom, M. Raisi, K. Alameh, S. Bouzerdoum, K. Eshraghian, Z. Wang, X. Zhao. A novel MicroPhotonic processor for adaptive wideband RF interference mitigation. Presented at International Square Kilometer Array Radio Telescope Workshop, 27 July to August 2 ,2003, Geraldton, Australia.

S. Ahderom,and M. Raisi. Reconfigurable Wavelength Equalization Using Free-Space Optics. In *Proceedings of the Postgraduate Electrical Engineering and Computing Symposium PEECS 2003,* Bentley, Australia, October 2003.

M. Raisi, and **S. Ahderom.** Role of Micro-Photonic processors in future optical communications. In *Proceedings of the Postgraduate Electrical Engineering and Computing Symposium PEECS 2003,* Bentley, Australia, October 2003.

Acknowledgements

I would first like to acknowledge the incredible support and understanding of my wife, Debbie, whose sacrificial help in countless ways made this dissertation possible. Thanks JJ!

I gratefully acknowledge the support and invaluable suggestions of my principal supervisor, Prof. Kamran Eshraghian. I am indebted to my co-supervisor, Prof. Kamal Alameh, without whose deep and constant guidance, encouragement, wisdom and optimism, it is fair to say that this thesis would not have been the same. Thanks Kamal! I gratefully acknowledge the patient guidance of Prof. Rafie Mavaddat, as well as the help of Dr. Daryoush Habibi, especially in the early stages of the course of study. Beyond ECU, I am thankful for the many useful discussions and experimental insight of Prof. Joseph Shamir of Technion University, Israel, and Dr. Timothy Wilkinson of Cambridge University, UK.

Further, it is with pleasure that I acknowledge the assistance – technical, academic and adminstrative – of many individuals, especially of note being David Lucas (help with computer programming among other things), Mehrdad Raisi, Rong Zheng, Dr. Zhenglin Wang, Katherine Frew, Dr. Xialin Zhao and Kourosh Sheikhzadeh and many many others.

I humbly and sincerely thank all the above and all other staff at the School of Engineering for their friendship, which made my time at ECU so much more rich and fulfilling.

I acknowledge with thanks the generous financial support of the Federal Department of Education, Science and Training through its Australian Postgraduate Award, Edith Cowan University through its ECU Excellence Award, and the Australian Research Council.

Abstract

The tremendous expansion of telecommunication services in the past decade, in part due to the growth of the Internet, has made the development of high-bandwidth optical networks a focus of research interest. The implementation of Dense-Wavelength Division Multiplexing (DWDM) optical fiber transmission systems has the potential to meet this demand. However, crucial components of DWDM networks - add/drop multiplexers, filters, gain equalizers as well as interconnects between optical channels - are currently not implemented as dynamically reconfigurable devices. Electronic cross-connects, the traditional solution to the reconfigurable optical networks, are increasingly not feasible due to the rapidly increasing bandwidth of the optical channels. Thus, optically transparent, dynamically reconfigurable DWDM components are important for alleviating the bottleneck in telecommunication systems of the future.

In this study, we develop a promising class of Opto-VLSI based devices, including a dynamic multi-function WDM processor, combining the functions of optical filter, channel equalizer and add-drop multiplexer, as well as a reconfigurable optical power splitter. We review the technological options for all-optical WDM components, and compare their advantages and disadvantages. We develop a model for designing Opto-VLSI based WDM devices, and demonstrate experimentally the Opto-VLSI multi-function WDM device. Finally, we discuss the feasibility of Opto-VLSI WDM components in meeting the stringent requirements of the optical communications industry.

Contents

List of Tables

List of Figures

Chapter 1

Introduction

1.1 Background to the Study

The dawn of the modern "information age" can be traced to the tremendous scientific and technological discoveries of the first half of the twentieth century, leading to the development of electronic devices. In turn, in the second half of that century, the capacity of these integrated circuits was constantly improved, both in the speed and density of the transistors, allowing the development of systems such as the computers that greatly enhanced our ability to process information. The rate of these improvements is popularly dubbed "Moore's Law", after Gordon Moore, onetime CEO of Intel Corp., who predicted in 1965 that the density of integrated circuits will double every year [6,7]. As can be seen in Fig. 1.1, however, it has been argued that improvements in the speed of transistors is likely to taper off in the near future, due to fundamental physical limits of carrier mobility and quantum effects as well as difficulties with lithographic processing at ever smaller transistor sizes. Further, as speed of transistors increases, the crosstalk between adjacent transistors tends to increase, thereby complicating the design of Ultra-Large Scale Integrated circuits.

In parallel to the growth of electronic systems, optical transmission systems, utilizing fiber optic transmission lines and laser transmitters, have been increasing their capacity at an even greater rate. Figure 1.2 shows the increase in capacity of optical fibers in time. It is therefore natural to expect that the combination of the advantages of each technology (i.e. electronic and optical) will further enhance the performance of systems. Indeed, the field of opto-electronics, which mainly attempts to exploit the high bandwidth optical systems and the ease of control in electronic systems, to synthesize systems with better performance

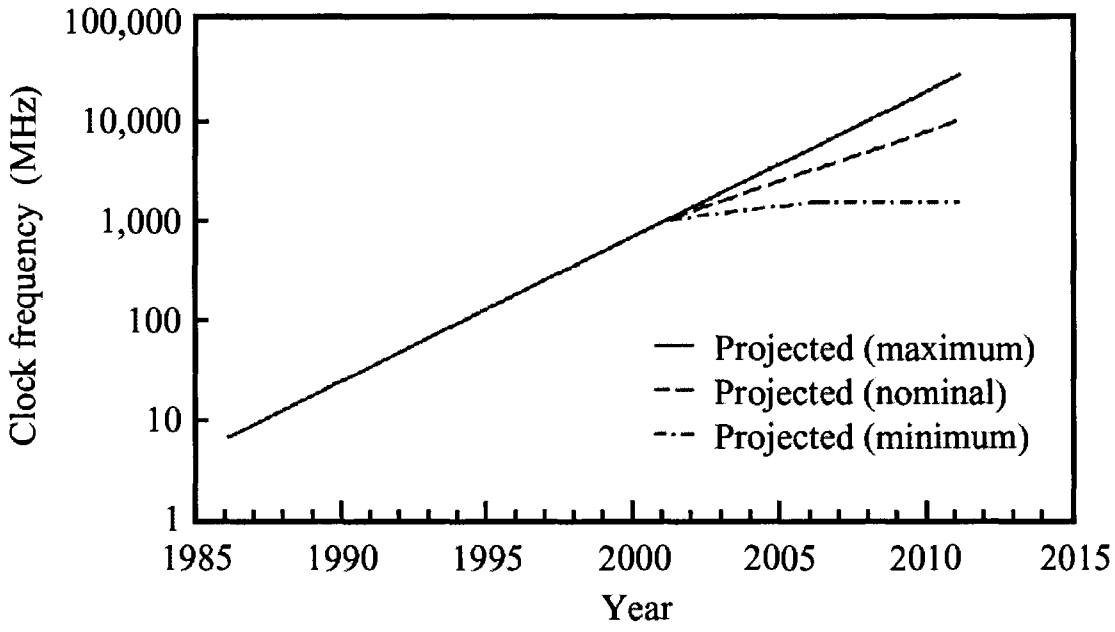

Figure 1.1: Projected trend in microprocessor clock frequency (from IBM Journal of Research and Development, vol. 44, no. 3 (2000))

than purely electronic or optical systems. This study in particular, will deal with the use of Opto-VLSI technology, integrating the electronic processing capacity of silicon VLSI systems with optical modulating devices for application in optical communication systems.

1.2 Introduction to WDM Optical Networks

Wavelength Division Multiplexing (WDM) is defined a communication system whereby many data channels modulate different carrier wavelengths and the modulated carriers are multiplexed into one waveguide (fiber) for transmission. Figure 1.3 shows a point to point transmission system with many wavelength channels being utilized. The optical fiber has very large bandwidth. Using a single carrier frequency, it is not possible to fully exploit this bandwidth, since a very high bit rate modulation technology would be required (>10 Tb/s), which is not available. Therefore, the bandwidth is efficiently utilized by using a large number of concurrent carriers, which are separated by at least twice the modulation frequency, in order not to overlap.

Another advantage of using multiple wavelength channels over a single one, is the ease in managing a multinode network where the wavelength channels can be separated using optical equipment and allow for wavelength based addressing or dividing different types

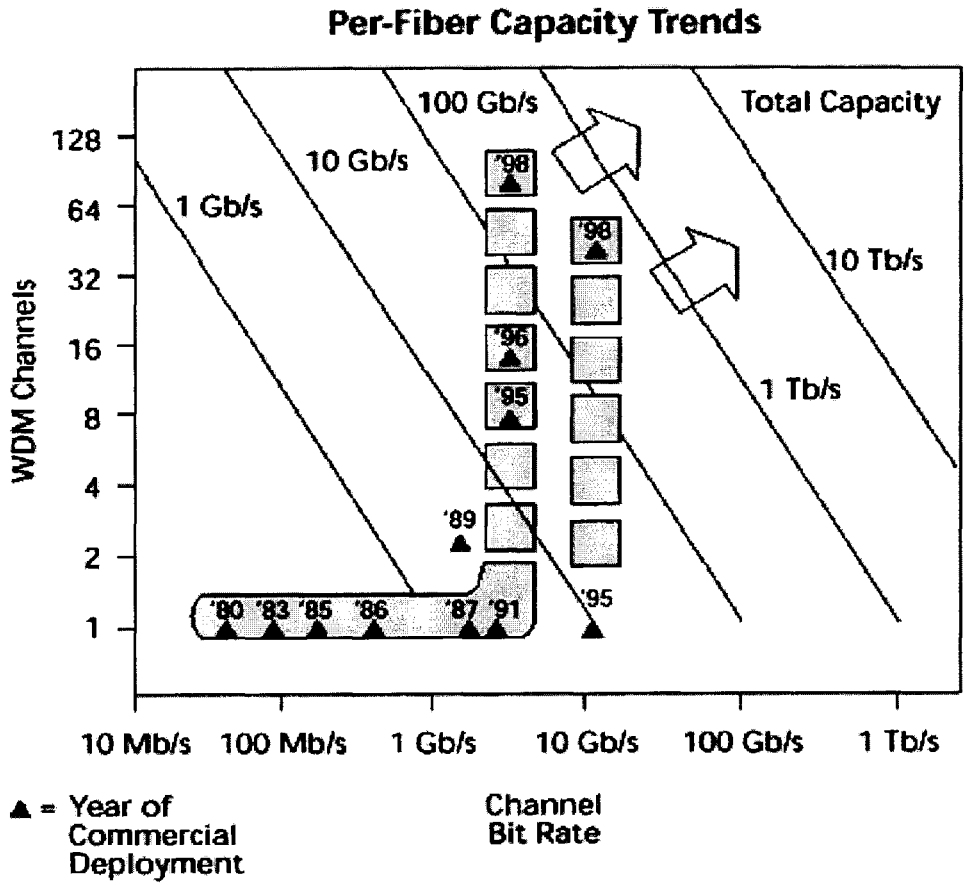

Figure 1.2: Trend in fiber capacity (Bell Labs Technology, vol. 2, no. 2 (1998))

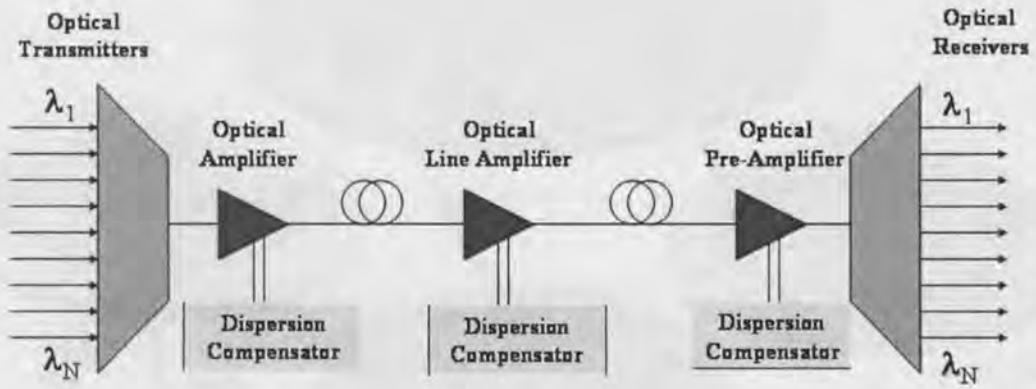

Figure 1.3: WDM Transmission system

of traffic or handling different protocols simultaneously in different wavelength channels. Figure 1.4 shows different types of WDM network topologies, which are used in varying types of networks. For example, metropolitan networks tend to have ring topologies, where each node is a telecommunication station or data center. Optical access networks, on the other hand, tend to use the same optical wavelength channel split among different users through time division multiplexing, since the bandwidth requirement of each user would be relatively small.

The past decade has witnessed a great increase in the demand for higher capacity telecommunication networks, in part due to the explosion of the Internet and the proliferation of other wide area data networks. To meet this demand, considerable research has been conducted to determine the maximum capacity limits of optical fibers. Point-to-point data links with terabit per second capacity have already been demonstrated. Further, significant growth is possible before theoretical limits are encountered [8, 9]. Therefore, the bottleneck is expected in the switching fabrics at the communication nodes. Current switching systems utilizing the hybrid Optical-Electrical-Optical (OEO) technology, are not able to handle the high bit rate per channel required by the demand for high-speed

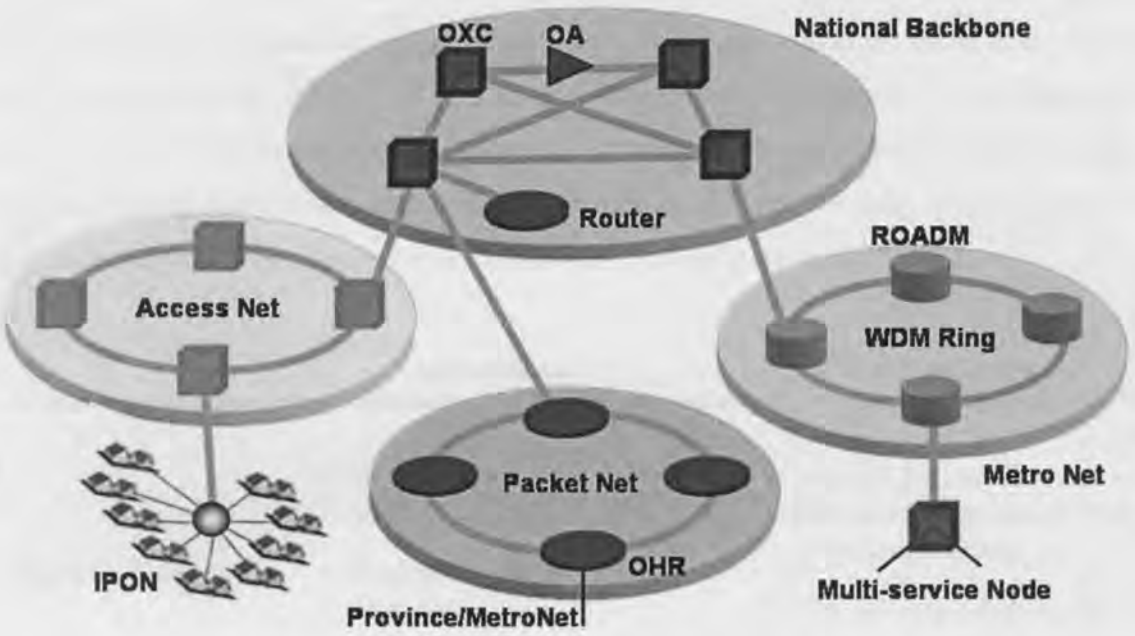

Figure 1.4: Typical WDM Network showing metro, access and longhaul circuits

networks. Therefore, the only feasible switching approach will have to employ optically transparent paths. In this context, this study aims to contribute to the development of optically transparent communication switches using Opto-VLSI technology.

Except for isolated point-to-point communication links, all multi-line networks by definition contain "nodes", where two or more fiber lines meet. At these nodes, a "cross-connect" connects channels from one port to another. There are two basic types of cross-connects:

Hybrid switching: The optically encoded data stream in an optical fiber is converted into electronic data by means of a photo-detector, and then an electronic cross-connection circuit is used to switch between electronic data streams, and finally, the electronic signals are converted back into the optical domain, to be launched into the output fiber [10]. This approach is also referred to as Optical-Electrical-Optical (OEO) switching.

All-optical Switching: The data channels are switched in the optical domain. Since the actual light beams from the input ports are directed (or steered) into output ports, this approach is also called "optically-transparent" switching [11]. Such systems are oblivious to the particular characteristics of the signal itself, and so are transparent to the bit-rate of the light signal and the particular transmission protocols used.

Both of the above switching approaches have inherent strengths, which make them suitable for differing requirements in an optical network. Generally, it is fair to expect that the hybrid approach would be suitable for low bit rate communication links, owing to the convenience of using VLSI circuits as switching fabrics. However, as was shown in Fig. 1.1, as the bandwidth of optical networks increases, electronic switches prove to be less feasible, and optically transparent switches become more attractive [10]. A comparison of the advantages and disadvantages of the two approaches is shown in Table 1.1.

	Advantages	**Disadvantages**
Hybrid Switch	• Well developed VLSI platform • Noise free (electrical) signal regeneration • Packet switching possible	• Limited bandwidth (due to increased cross-talk at high clock frequencies) • Not bit-rate transparent • Not transparent to transport protocol
All-optical Switch	• Low cross-talk possible • Bit-rate transparent • Transport protocol transparent	• Noisy optical amplification • Only wavelength channels switched • Unproved technology

Table 1.1: Comparison of hybrid and all-optical switching

As shown in Fig. 1.2, wavelength division multiplexing (WDM) allows independent signals to be sent on the same fiber using different wavelength for each signal. These so-called "lambda-channels" greatly increase the fiber capacity. At the network node, the fiber signals are de-multiplexed into the individual channels, and then switched to the output ports.

1.3 Need for Reconfigurable WDM Networks

If WDM components used are reconfigurable, the network becomes more efficient by flexibly delivering just the requisite bandwidth to the data services provided, and incorporating fault tolerance for high quality of service [12,13]. The nature of the flexibility of a network determines its ability to reconfigure, and hence the efficiency with which it can utilize its inherent bandwidth [14]. Figure 1.5 shows three different levels of network reconfigurability. In Fig. 1.5a, which corresponds to the first generation of optical networks, has dynamic data services, however, the optical network in the physical layer is completely static and cannot be reconfigured. This severely limits the bandwidth that can be utilized by a real network. Figure 1.5b shows the current technological state, where in addition to the data services, a digital physical layer is available, which is reconfigurable. This physical layer usually consists of digital switches, in setups such as the hybrid O-E-O switches mentioned in the previous section. However, the WDM layer itself remains optically static. The future dynamic system is shown in Fig. 1.5c, where all the layers of the communication system are fully reconfigurable, allowing for efficient use of the network's bandwidth. Therefore, at the optical light path reconfigurable network components have a great potential in future networks.

1.4 Contributions of this Thesis

This thesis deals with a novel class of WDM components, specifically a novel multifunction WDM device. Utilizing the technological strength of optical and VLSI systems, we synthesize a device able to accomplish multiple WDM functions. Specifically, the main contributions of this thesis are:

- Proposed a Multifunction Opto-VLSI based WDM device, that can accomplish four dynamic network tasks simultaneously: optical tunable filtering, optical power equalization, add drop multiplexing and optical port switching.
- Proposed alternative architectures for the Opto-VLSI based WDM multifunction device, that is scalable as the number of channels required grows.
- Analyzed the behavior of the Multifunction WDM devices geometrically.

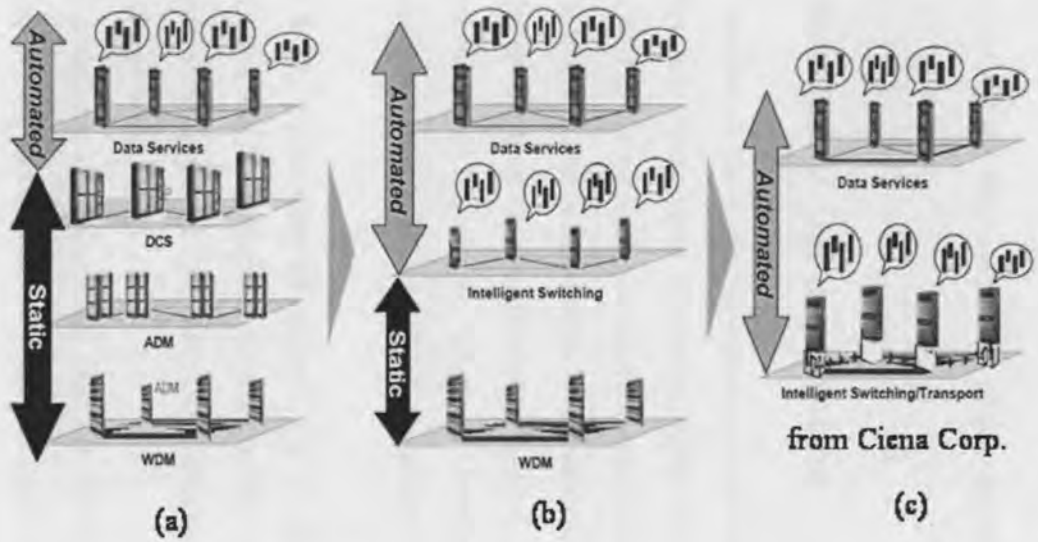

Figure 1.5: Progress of reconfigurable optical networks (a) past static WDM networks (b) Present WDM reconfigurable DCS (c) future fully reconfigurable networks

- Conducted analysis on the insertion loss, bandwidth characteristics and crosstalk performance of the WDM multifunction device.
- Devised algorithms for Hologram generation using arbitrary number of phases optimized for crosstalk and efficiency.
- Experimentally verified model for hologram generation.
- Experimentally demonstrated the functions of the Opto-VLSI multifunction device.
- Devised a method for determining the phase characteristics of the Opto-VLSI processor.

1.5 Organization of the dissertation

The remaining chapters of the thesis are arranged as follows. **Chapter 2** reviews the current WDM component technologies, including filters, demultiplexers, switches, add/drop multiplexers, as well as the technologies used for spatial modulation of light.

Chapter 3 introduces the multifunction WMD device, and determines the geometrical parameters of the device from its specifications. Further, a procedure for determining all the parameters of the device is proposed. An alternative architecture for the multifunction device is also analyzed that is able to meet scalability requirements of (dense) WDM systems.

In **chapter 4**, the propagation of optical fields is used to determine the parameters affecting the insertion loss of the multifunction processor. A method for the determination of the filter response is presented. Further, the dependence of crosstalk performance on architectural features is discussed.

Chapter 5 introduces two algorithms that are used in the generation of holograms. The computer generated holograms are experimentally verified and the efficacy of the methods used compared. Further, the usefulness of the two algorithms for the WDM device is discussed.

Chapter 6 devises a method for characterizing the Opto-VLSI processor and reports on the experimental demonstration of the functions of the multifunction processor. Further, a demonstration of the notch filtering function of the alternative architecture of the multifunction device is reported.

Finally, in **Chapter 7** the feasibility of the multifunction processor in WDM networks is considered, and future work is proposed.

Chapter 2

Literature Review

In this chapter, we review current state-of-the-art WDM technologies, and compare them with the ideal characteristics for the devices. We also present current state of Opto-VLSI spatial light modulation (SLM) approaches and technologies, and some existing WDM architectures utilizing SLM devices.

2.1 Review of WDM technologies

We will first review the existing technological options for certain key components of WDM networks, including optical filters, EDFA gain equalizers, add/drop multiplexers, and optical interconnects. WDM equipment should ideally display the following characteristics:

Low insertion loss: The optical power loss of the component from input fiber(s) to output fiber(s) should be minimal. The more lossy the components, the more optical amplifiers will be required, which in turn increases cost and system bit error rate [15].

Polarization independent loss: The insertion loss should also not depend on the polarization state of the input signals. This is because, typically, the polarization state in a fiber is random, leading to output power levels varying with time [16]. This results in increased bit error rate in the communication system. The maximum variation in loss due to polarization is known as *Polarization dependent loss* (PDL), given usually in dB.

Temperature dependence: The key wavelength and loss characteristics of a WDM device must be independent of temperature. The *temperature coefficient* measures the amount of wavelength shift per unit change in temperature [15].

2.1.1 Optical filters

Optical filters are used in WDM systems for at least two major tasks. They can act to demultiplex WDM signals by blocking all but a selected channel in a WDM terminal, and inversely can multiplex selected channels at the same terminal. Further, filters can be used in wavelength crossconnects and add/drop multiplexers.

In addition to the characteristics of WDM devices noted above, the key characteristics of an ideal WDM filter are:

Flat passbands: The passband of a WDM filter must be flat, so that within the passband, the output power level does not change with small changes in laser wavelength [17]. Wavelength of semiconductor lasers tends to change with time due to various physical mechanisms [18].

Sharp passband skirt: Outside of the passband, the outside of the channel passband should be sharp, in order to minimize crosstalk from adjacent channels [19]. This is measured in the *crosstalk isolation*, which is the ratio of the peak power to the power passed from adjacent channels.

2.1.1.1 Fixed Optical Filters

The most important fixed optical filters are the Fabry-Perot etalons, the Fiber Bragg gratings and the dielectric thin film gratings.

Fabry Perot Etalon: An etalon is formed by two semi-reflective surfaces, with a short cavity between them. An incident beam travels through the first surface and through the cavity onto the second surface. The reflected beam is then partially also reflected by the first surface. This creates an infinite impulse response filter, allowing transmission through the etalon when the total path traveled within the cavity is a multiple of the optical wavelength, or when the cavity length is $m\lambda/2$, where m is a typically large integer [20]. Therefore by choosing a suitable cavity length, a filter can be constructed. However, since the transmission condition will also be satisfied by other wavelengths, the filter cannot function over a wide wavelength range. The bandpass width can be controlled by the reflectivity of the two surfaces, with higher reflectivities leading to narrower filter bandwidth [21].

Fiber Bragg gratings: Fiber-Bragg gratings (FBGs) are constructed by creating small periodic index variations along the length of a fiber, typically with a period d that

satisfies the Bragg condition $\lambda = 2d/n$, where n is a typically small integer. This causes the fiber to selectively reflect a single wavelength while passing through all other wavelengths. FBGs are the most popular forms of optical filters, mainly because they can be manufactured easily to produce filter with sharp skirts and flat passbands [22–24].

Dielectric thin film (DTF) gratings: Thin film gratings are made by depositing films of alternating high index of refraction and low index of refraction onto a transparent substrate, such as glass [25]. The thickness of each layer is chosen to be a quarter wave optical thickness (of the desired filter's center wavelength). Thus, at the desired wavelength the waves interfere constructively, while other nearby wavelengths interfere destructively. The choice the two indices of refraction determine the reflectivity as well as the Q-factor of the filter. The main characteristics of a DTF filters are low band-pass loss (<0.3 dB), good channel spacing (>10 nm) and low interchannel cross-talk (<-28 dB) [26].

2.1.1.2 Tunable Optical Filters

Tunability in optical filters allows for the reconfigurable selection of WDM channels. This leads to better flexibility in fiber-optic capacity management. Some important characteristics of such filters are wide tuning range, arbitrarily shaped response and fast tuning speed [27]. Below we review some of the mechanisms used to tune the above mentioned fixed filters:

Piezoelectric cavity: When a Fabry-Perot filter's cavity is changed, the corresponding wavelength is modified. This can be accomplished by applying a voltage to a piezoelectric material on the surface of the cavity, thereby changing the cavity length. As we noted above, the filter's wavelength is directly related to the cavity length. These filters can achieve wide tuning ranges and narrow filter bandwidths [15]. However, the bandpass skirt is not sharp, which means that the wavelength channels must be separated further apart. This makes the piezoelectric cavity tunable filters unsuitable for DWDM (Dense Wavelength Division Multiplexing) Systems [27, 28].

Ferroelectic Liquid Crystal Cavity: In this scheme, the Fabry-Perot etalon is filled with an anisotropic liquid crystal. When a voltage is applied, the index of refraction in the cavity is changed, which changes the effective cavity length, and hence the wavelength of filter [29].

Stressed/Heated fiber-Bragg gratings: Fiber-Bragg gratings can be made tunable

by mechanically stretching them or applying heat to them, and thus physically changing the period of the grating. According to the Bragg condition mentioned above, the center wavelength of the fiber will change accordingly [30, 31].

Acousto-Optic filter: Acousto-optic filters use, similar to the fiber Bragg gratings, the Bragg condition to set the filter's center wavelength. An acousto-optic material is a material whose index of refraction changes when a surface acoustic wave is applied to it. By adjusting the frequency of the applied RF acoustic wave, a standing wave of high and low index of refraction is created which acts as a filter analogous to an FBG. To change the center wavelength, one changes the frequency of the RF signal, and hence the period of the periodic standing wave on the Material. Lithium Niobate is typically used as the acousto-optic material [32].

Mach-Zender interferometers: A Mach-Zender interferometer is constructed by splitting the incoming optical beam into two beams, and then recombining them after they have traveled unequal paths [33, 34]. When the path difference is $\lambda/2$, the two split beams interfere destructively, while the beams interfere constructively if the path difference is a multiple of λ. The path difference can be controlled by applying heat to portion of one of the paths, thereby lengthening the path, or by applying mechanical compression or stretching. However, if high speed is desired, the path difference can be created by inserting a wavelength dependent Lithium-Niobate material in one path, whose index of refraction can be controlled by an applied voltage, thereby also changing the path difference.

Semiconductor grating assisted vertical couplers: These filters consist of two slab waveguides (usually in the InP-InGaAsP material system) that are stacked in close proximity. The cladding of one layer has a periodic index variation in the guiding direction. The coupling between the two waveguides is dependent on the period of the grating, and couples only a selected wavelength. Therefore, when an electrical current is passed through the grating structure, its optical index of refraction changes, and thus the coupled wavelength is changed. This structure is easily integrated with distributed feedback lasers, since they utilize a similar grating structure [35].

MEMS cantilevers: Another tunable filtering solution consists of Fabry-Perot interferometers that are constructed from a micro-electro mechanical systems. In its simplest form, a cantilever is constructed on top of a reflective surface in Silicon. The cavity length determines the center frequency of the filter. When the cantilever is moved through a

capacitive actuator, the center frequency of the filter can be tuned [36,37].

Some typical values for key functional parameters of various optical filtering technologies are shown in Table 2.1 [27,33,35–37]. The data was compiled from the references to the technologies given above. In general, we may conclude that if a large number of channels (>100) are required, Fabry-Perot filters and Acousto-optic filters are used. However, if speed is required the electrooptic and semi-conductor filters are more appropriate. Further if low loss is a critical parameter, then semiconductor filters are more suitable.

Table 2.1: Comparison of filtering technologies

Filter type	**Technology**	**Insertion loss**	**Crosstalk isolation**	**Tuning speed**
Fixed	Fabry-Perot	3-5 dB	30dB	N/A
Fixed	FBG	<0.1 dB	>25 dB	N/A
Fixed	DTF	<0.3 dB	> 28 dB	N/A
Tunable	Piezoelectric FP	<5 dB	30 dB	1 ms
Tunable	InP coupler	gain possible	30 dB	10 ns
Tunable	FLC-FP	3 dB	30 dB	> 100 μs
Tunable	Stressed/Heated FBG	>0.1 dB	22 dB	> 2 μs
Tunable	AOTF	5 dB	20 dB	10 μs
Tunable	MZI	1 dB	22 dB	<1 μs
Tunable	MEMS	1-2 dB	30 dB	1-10 ms

2.1.2 Optical Multiplexers/Demultiplexers

When a WDM fiber is coupled into an Optical demultiplexer, the individual channels are separated and coupled into different fibers. Similarly, a multiplexer takes many inputs, each containing a WDM channel signal, and with low insertion loss, adds them into the output fiber. There are two major approaches to optical demultiplexing: free-space gratings, and arrayed waveguide gratings.

Free-space gratings: When a WDM signal, containing many wavelengths is shone on a diffraction grating, each channel is diffracted in a different direction. The gratings are usually blazed to impart most of the power in the first diffraction order. For a blazed first order beam, the grating equation will be of the form [38]:

$$\lambda = d(\sin\alpha + \sin\beta) \tag{2.1}$$

where λ is the wavelength, α is the angle of incidence, β is the diffracted angle, and d is the period of the grating. As can be seen from the equation, the angle of diffraction is directly dependent on the wavelength λ. If fiber collimators and couplers are placed at the path of the different wavelengths, a grating demultiplexer is realized.

Arrayed Waveguide Gratings (AWGs): These are interferometic devices consisting of two cavities and an array of waveguides between them [39–45]. First a beam containing WDM signals is launched into the first cavity. This beam is coupled into the array of waveguides linking it to the second cavity. The length of the waveguides are all different, and each beam arriving in the second cavity has a different group delay. Since this group delay is dependent on wavelength, the light coupled out of the second cavity will be at different positions in the output from the second cavity. Hence by placing the output fibers are different points in the second cavity, a demultiplexer is realized. Some of the drawbacks of AWGs are their high polarization dependence and their temperature sensitivity. However, AWGs exhibit a flat spectral response around their center frequency. They typically have 3 dB of insertion loss and better than 35 dB of crosstalk isolation [26].

In order to make demultiplexers smaller and have better crosstalk isolation, a new king of dispersive element, named "Super-prisms" have been made out of photonic crystals. These devices are capable of high spectral dispersion (some 500 times that of typical blazed gratings) [46]. Therefore, these devices could potentially allow much denser WDM channels. Optical multiplexers can be realized by the same methods mentioned above, by simply reversing the input are the single output, and the outputs as the multiple wavelength inputs.

2.1.3 Optical Channel Equalization

It is desirable that the channels in a WDM fiber be all equalized, since a large inequality in optical power between adjacent channels degrades the bit error rate (BER) of the weaker signals, at the photoreceivers. However, some optical components, most notably the Erbium doped fiber amplifiers (EDFAs), introduce a variation in the power levels of the wavelength channels. Another source of power level difference is when the channels are multiplexed from different WDM signal paths, which could have traveled different optical

lengths. A channel equalizer, thus, is a component that equalizes the optical power of the channels in a WDM fiber. It has been shown that if the power profile of channel equalizes can be adjusted dynamically, better quality-of-service (QoS) [18], better flexibility in fiber optic transmission management can be realized. For dynamic channel equalization, in addition to the demultiplexers and multiplexers, variable attenuators are needed to control the power profile of the stronger signals. Optical channel equalization architectures are of two kinds:

Optical Profile equalizers: In this architecture the WDM signal is demultiplexed into wavelength ranges (coarser than the individual channels) covering the wavelengths in the WDM signal, and attenuating each filter as needed and then multiplexing the signals. This is able to effectively create a transmission profile that can effectively equalize the gain profiles of EDFAs. However, channel-by-channel equalization is not possible since the number of filters is less than the number of channels. Such equalizers have been demonstrated using liquid crystal variable attenuators [47], integrated SiON waveguides [48, 49], Acousto-optic filters [50, 51] and micro-electomechanical mirrors [52].

Channel-by-channel equalizers: In this setup, the WDM signal is demultiplexed into its constituent channel wavelengths. Some channels are then individually attenuated to equalize them with the power of the lower power channels, and all the signals are subsequently multiplexed into the output WDM fiber. The advantage of this architecture is the equalization is done on the channel level, and hence, the output signal will always be equalized. Theoretically, the optical profile equalizers will be able to perform channel-by-channel equalization. However, the insertion loss of demultiplexers and the cost of integrating an attenuator for each channel is prohibitive, especially when large number of channels are required, as in DWDM systems [53].

2.1.4 Optically-transparent crossconnects and splitters

For reasons explained in the introduction - pertaining to the extremely high demand for feasible and practical optical networks - the whole field of optical switching technology has attracted an intense and broad attention. Due to the great challenges involved in implementing systems which can meet the stringent telecommunication standards, researchers in this field have tended to cast their nets wide - proposing extremely varied and novel approaches, both in design architectures and material systems. However, two broad classes

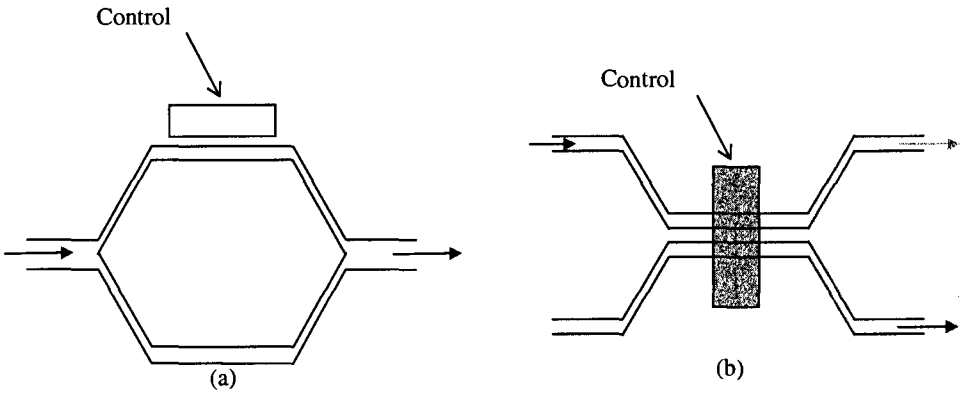

Figure 2.1: (a) Mach-Zender Interferometer, (b) directional coupler (adapted from Saleh and Teich [1]).

of architectures have emerged with consistently more promise: guided wave and free-space systems, each approach having inherent strengths and limitations.

2.1.4.1 Guided Wave Systems

Guided wave switch systems keep the incoming light beam optically confined, just as it is in the fiber. We may categorize the systems in terms of the switching principles applied and the material systems used. In this section, we will look at the three main material systems used - Lithium Niobate, InGaAsP, and planar silica. For re-configurable interconnect, the switching principles may be categorized into two types: Mach-Zender Interferometers (MZIs) and directional couplers.

Mach-Zender Interferometers Switch: In an MZI, the incoming light beam is split into two equal-energy (-3 dB) optical paths. The optical path length of the two beams is varied externally before they recombine. Depending on the optical path difference, the output beam will either be on or off.

Directional Couplers: In this structure, two waveguides are brought close together so that the two guided waves are coupled. Depending on the length of the wave-guides, the beam will hop from one side of the wave-guide to another. This switching depends on the propagation constant of the mode traveling in each wave-guide. Therefore, by externally controlling the propagation constant, the output port can be selected. Figure 2.1 shows the layout of directional couplers and MZIs.

The switch can be constructed, either using the directional coupler alone, or a combination of directional couplers and MZI devices [2]. The 1×2 or 2×2 switches constructed

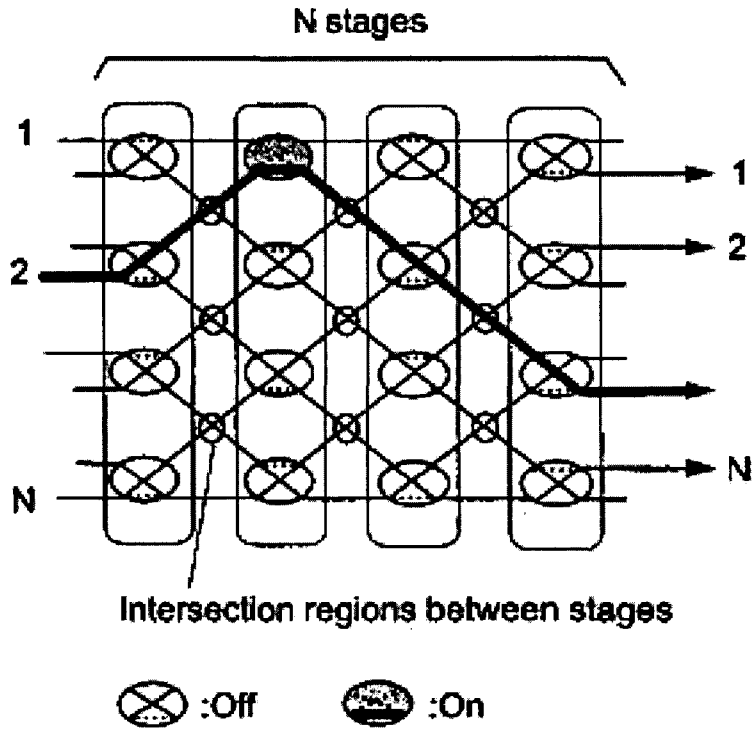

Figure 2.2: Multiple stage $N \times N$ switch constructed from 2×2 switches (from [2]).

from these devices can be scaled to an $N \times N$ switch by cascading them into N stages as shown in Fig. 2.2.

Of the many different types of materials systems in which these wave-guide switches can be implemented, we will briefly discuss the most prominent in the literature:

Lithium Niobate: This material is used as a wave-guide because its refractive index changes when an electric field is applied across it (via the Pockels electro-optic effect [2]), allowing the possibility of creating directional couplers and MZIs. Once the field is applied, the change in refractive index is very fast. Therefore, the limit on the switching speed is mainly associated with the speed of producing the electric field, i.e. the lumped capacitance of the electronic circuit. The change in refractive index is small, therefore for sufficient modulation, a large voltage or a long wave-guide are needed [33]. The high switching speeds possible make it an attractive candidate for optically transparent packet switching applications.

Indium Gallium Arsenide Phosphide (InGaAsP): In the InGasAsP material system, the modulators can be integrated with a host of other electronic and opto-electronic

circuit elements, including lasers, photo-detectors, optical amplifiers and field-effect transistors. ([51, 54, 55]). This material system also exhibits a fast electro-optic response to applied voltage. However, the crystal is anisotropic, hence it is difficult for the device to be polarization-insensitive. Further, it exhibits high optical absorption in the waveguide at telecommunication wavelengths [56].

Silica and Polymer waveguides: Both of these materials are suitable for integration with silicon VLSI circuits. Further, both materials utilize thermo-optic effects, i.e. they use heat to change the index of refraction in a wave-guide. Typically, a conducting film is deposited on the wave-guide, which will heat the wave-guide when current is passed through it. As can be expected, such systems have lower switching speeds (>1 ms) ([2], [57]).

Electro-capillary or "bubble" switches: This is a class of switches not utilizing the directional coupler or the MZI, but rather, a bubble at the junction of two waveguides which can be moved by surface tension or "electro-capillary" effect, which in turn is effected by a thermal source ([58], [59]).

In conclusion, wave-guide switches have the advantage of elegant design and easy integration with the telecommunication fibers. However, since the basic switch device is 2×2, if larger $N \times N$ switches are desired, N stages of switches will have to be cascaded in series. This introduces insertion losses and cross-talk, which limit the scalability of the architecture.

2.1.4.2 Micro-electro mechanical (MEMS) Free-space Systems

Free-space optical switching systems take advantage of the non-interference of optical signals to switch large numbers of optical signals in a single stage, which is not possible in guided wave switches. The two main mechanisms to re-configurable beam steering in this class of devices are holographic diffraction and mechanical steering.

For mechanical beam steering devices, attention seems to concentrate on mirrors using micro-electro mechanical systems (MEMS), where arrays of micro-mirrors are constructed on silicon substrate. Some examples of research in micro-mechanical systems is given in the references ([60], [61], [62], [4], [3]). Typically, there are two architectures in MEMS switches:

Matrix Switches: This approach uses N^2 mirrors arranged in a matrix to switch N inputs to N outputs. The mirrors are arranged in such a way that only one of N mirrors

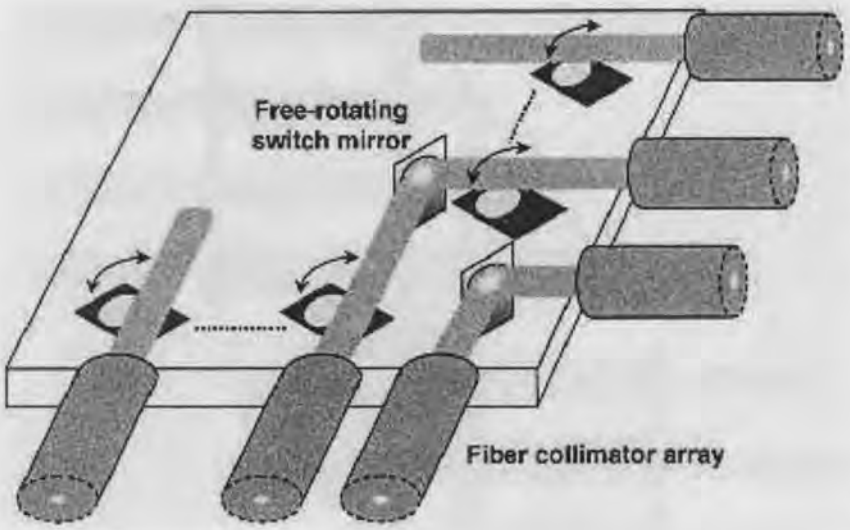

Figure 2.3: Matrix type free-space MEMS switch (from [3]).

on the path of the beam is active, the rest are folded out of the beam's way. Since the mirrors need to be only in two distinct positions - reflecting the beam or out of the way - the mirrors are sometime referred to as "digital mirrors".

Beam-Steering Switches: In this approach, two sets of mirrors are used to switch between the input and output ports. The first mirror receives its corresponding beam, and routes it to a mirror corresponding to the selected output port. The output mirror then re-deflects the beam normal to the selected output port. In this approach only $2N$ mirrors are used in an $N \times N$ switch. However, the mirrors must be able to switch in many different directions, i.e. in an analog manner.

Figures 2.3 and 2.4 show the matrix and beam steering approaches in MEMS switches. The former has advantages in that the accuracy of the mirrors can be set as there is only one direction for reflecting the beam. However, for larger scale switches, the latter approach is feasible, since an $N \times N$ switch would require only $2N$ mirrors. In general, the most significant drawbacks of mechanical switching systems seem to be the difficulty in bulk manufacturing large array of mirrors, and the need for adaptive compensation to counteract environmental vibrations and the unavoidable mechanical wear.

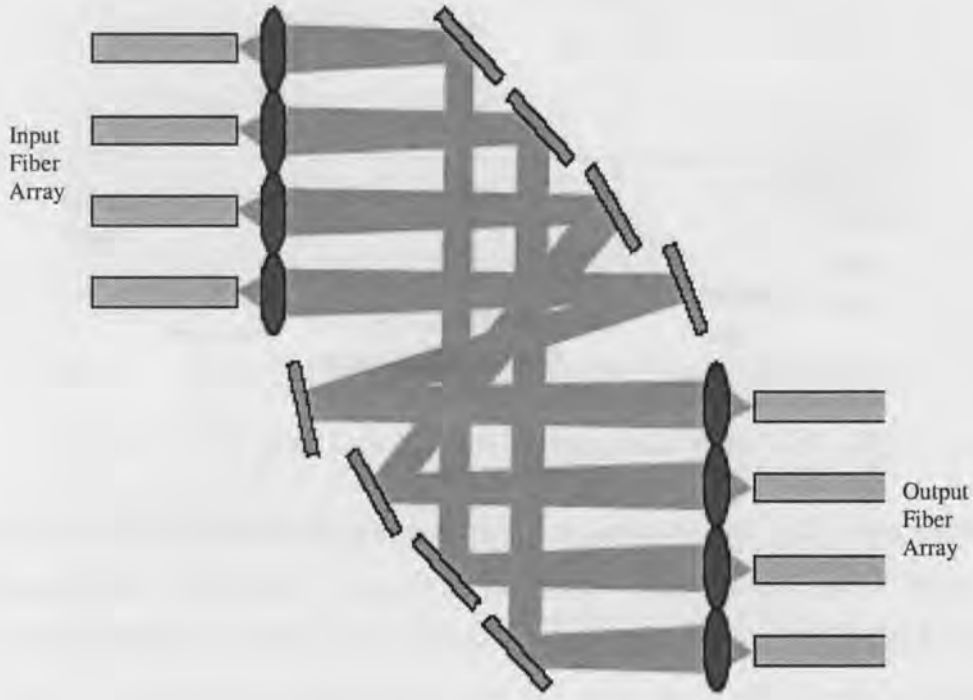

Figure 2.4: Beam steering type MEMS switch (from Harris [4]).

2.1.4.3 Holographic switches

The second type of free-space optical signal processing that is currently a topic of active interest (as well as the focus of this study) is diffractive phase modulation, where an optical signal is redirected using phase holograms recorded on "smart-pixel" spatial light modulators. Several material systems have been proposed for use in such systems, including a few III-V semiconductors (such as InGaAs/InP) and liquid crystal on silicon systems (LCoS) [63]. The advantage of using direct-gap semiconductors is the ease with which active optical components, such as lasers and optical amplifiers, can be incorporated into the smart pixels, thus allowing the possibility of signal boosting at the switching stage. The disadvantage of such materials, of course, is the cost and difficulty involved in large scale manufacture. Some recent work using III-V systems are detailed in the references ([64], [65], [66], [5]).

The LCoS material system appears to be practical as well as easy to integrate with silicon electronic circuits. The typical layout of a holographic switch is shown in Fig. 2.5.

One major shortcoming of the layout shown in Fig. 2.5 is that the single switching plane (SLM) can deliver the beams to the intended ports, however, except for one port,

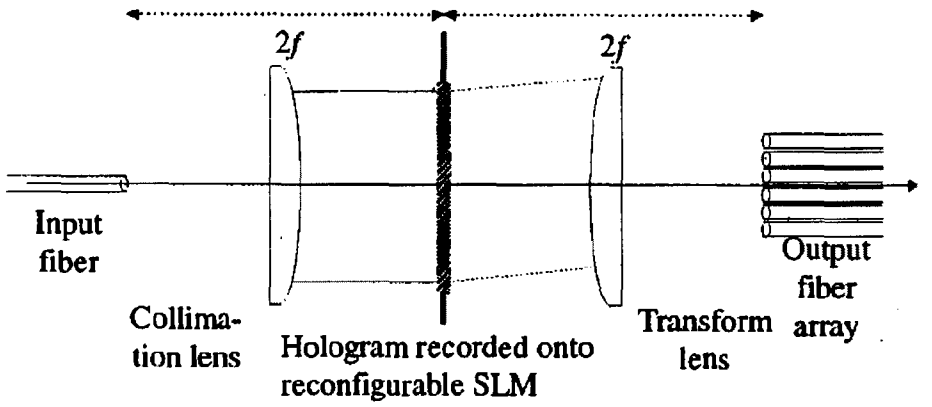

Figure 2.5: Typical Liquid Crystal Holographic Switch (from [5]).

cannot ensure that the beam will arrive at the port normally (head-on). This angular tilt introduces severe optical loss in launching the beam at the output port. Therefore, in this study, we will also consider a "two SLM" system, analogous to the MEMS switch in Fig. 2.4, so that the beam will always arrive at the output port, in a normal direction.

2.1.4.4 Comparison of Optical Switch Approaches

In Table 2.2, the advantages and disadvantages of the various approaches to optical switching described in the sections above are summarized.

2.1.5 Add-drop Multiplexing

Optical Add/Drop multiplexers (OADM) are fundamental devices for the operation of multi-node optical WDM networks. They function basically by extracting a specific set of wavelength channels from one or more WDM fibers (called Drop channels), or insert channel into WDM fibers (called Add channel) at a WDM node. Passive OADMs (P-OADMs) have a fixed add and drop channels while reconfigurable OADMS (R-OADMs) can dynamically select the drop port without physically altering the device's configuration.

As mentioned in the Introduction to the dissertation, the dynamic nature of future WDM networks requires the use of R-OADMs rather than passive OADMs. R-OADMs allow for better provisioning of network bandwidth, smoother integration of dynamic network services. There are two main architectures for add/drop multiplexers:

Switching OADMs: This structure consists of a multiplexer, an optical switch, and a demultiplexer. The the input WDM fiber is demultiplexed into its constituent channels,

Table 2.2: Comparison of optical switch technologies

	Advantages	**Disadvantages**
Lithium Niobate	High-speed switching	Difficult integration with electro-optic circuits
InGaAsP	Monolithic integration with opto-electronic devices; High-speed switching	Polarization dependent; High absorption waveguide
Silica/Poly	Easy integration with Silicon circuits	Slow thermo-optic switching
Thermo-capillary (bubble switch)	Possible integration with silicon circuits	Slow thermo-mechanical switching
Matrix MEMS	Digital mirrors (easier tolerances)	Unscalable at high port count (N2 mirrors)
Beam-steering MEMS	Better scalability (2N mirrors)	Difficult to control "analog" mirrors, need for adaptive control
Holographic Opto-VLSI processor (1 processor)	Non-mechanical steering	Angle of launch loss at output fibers
Holographic Opto-VLSI processors (2 processors)	Non-mechanical steering, lower insertion loss	Doubled diffraction loss as 1 SLM system

and each channel is either switched into the drop port, or coupled into the output multiplexer [67,68]. An add port is also included in the switch, to allow for inserting a channel into the output multiplexer. Generally, if there are m channels in the output port, and n number of Add/Drop ports, the switch size must be $(m+n) \times (m+n)$.

Filter OADMs: In this structure, a 3-port circulator is used with a reflective filter to realize the drop port. Therefore, the input WDM signal enters the first port of the circulator and exits on the second port, and is coupled to the filter. All the channels except the dropped channel pass through the filter and exit onto the WDM output. However, the dropped channel is reflected back from the filter into the second circulator port, and exits out of the third circulator port, which is the "Drop" port. Adding a channel is done in the opposite manner, with the WDM signal first passing through the filter uninterrupted (since it does not yet contained the channel to be added). Then it enters through the first port of the second circulator, and exits out of the second port, which is the WDM output. The wavelength channel to be added is launched into the third circulator port, and exits out of the first port. However, the filter reflects the signal back into to circulator, and the added channel appears in the WDM output port. Typically, the filters used for P-OADMs are fiber Bragg gratings (FBGs) [69]. For R-OADMs, acousto-optic filters [70], or thermally tunable FBGs [71,72] have been reported in the literature.

The large switches required for the Switching type OADMs make them expensive and cumbersome. However, they allow for relatively easy reconfiguration of the network. The filter type OADMs are practical for P-OADMs, however, the large insertion losses of acousto-optic filters and high cross-talk make R-OADM difficult in the architecture.

2.2 Technology for Spatial Modulation of Light

The complex waveform of a beam traveling in a certain direction completely describes the propagation properties of an optical beam. Therefore, the aim of a spatial light modulator (SLM) is to control the wavefront traveling in a particular direction so that the behavior of the beam can be controlled. Often, however, it is sufficient to control either the phase or amplitude of the wavefront, since it is difficult to simultaneously control the complex amplitude of the wavefront. In optical systems, since it is generally desirable to preserve as much optical power as possible in a WDM signal, the control of the phase is the preferred means of controlling the behavior of light.

The spatial light modulator is typically arranged into an array of square pixels, with each pixel independently manipulated to control the region of wavefront impinging on it. SLMs can be addressed in many different ways, electrically, for modulation materials that respond to the electric field or current; or optically, for modulating materials that respond to an optical field. Furthermore, depending on the optical properties of the modulating material, it may be possible for the SLM to work transmissively, that is, the output wavefront passes through the SLM, or reflectively, when the wavefront is reflected by the SLM. In this section, we briefly review some current technologies that are used in the spatial modulation of the optical wavefront.

2.2.1 The Stanford Vector Matrix Multiplier

An important precursor of holographic beam steering is the so-called Stanford Vector Matrix Multiplier (SVMM) [73], which is a series of light valves arranged usually on a plane. Each light valve controls a beam of light transmitted through it, and consists of a material whose anisotropy is electrically controlled (eg. liquid crystals) sandwiched between two polarizers oriented orthogonally to each other. Thus when an electrical field is applied to the anisotropic material, the transmittance of the material changes, and the beam passing through it variably attenuated. The main optical communications application proposed for the SVMM is optical switching [74,75]. In such architectures, for optical switching with M inputs and N outputs, each input is fanned out to N light valves on the SVMM, and M light valves (one from each input) is fanned into each output port. Thus by blocking all the valves except the light valves that route the input beams to the desired output ports, an optical switch is realized. The main shortcoming of this architecture is that the fan out required for each input beam quickly dissipates most of the input power, thus making the design unscaleable.

2.2.2 Self Electro-optic Effect Device (SEED) Modulators

The pixel cell of an Self electro-optic Effect Device (SEED) modulator usually consists of a semiconductor multiple quantum well (MQW) p-i-n structure. The MQW exhibits an optical property, called the quantum confined Stark effect (QCSE) [76], which is able to alter its index of refraction and absorption spectra by electrically changing the p-i-n bias voltage, or optically "biasing" the MQW through shining a control beam. When the

SEED is controlled optically, it is referred to as a symmetric-SEED (S-SEED), since both its inputs and outputs are optical [77–79]. Typically, SEEDs are fabricated using InP-InGaAsP semiconductor material system. The main draw-back of SEEDs is the difficulty of integrating them with large scale integrated electronic circuits [80, 81].

2.2.3 Magneto-optic modulators

Modulation of the optical wavefront magnetically is accomplished through the Faraday effect. When a magnetic field is applied to a magneto-optic material, its anisotropic properties change, and so, the polarization of a beam passing through the material is altered. By placing suitably oriented polarizer/analyzer pair on either end of the material, it is possible to modulate the amplitude of optical field. Most of the magneto-optic materials in use are based on yttrium iron garnets. The control magnetic field is usually generated by winding a conductor around the garnet. Therefore, it is impractical to build large pixel arrays of magneto-optic modulators [82, 83].

2.2.4 Deformable mirror devices (DMDs)

Deformable mirror devices consist of a single reflective membrane that is deformed by an array of actuators below the membrane [84, 85]. These actuators can be controlled electrically, as in the case of piezoelectric actuators, or optically, through the use of materials that exhibit high opto-mechanical effect.

Also in this class are the micromirror array devices that individually control the tilt of arrays of micromirrors (mentioned in Section 2.1.4.2). Although these devices don't modify the wavefront of an incoming beam uniformly across a pixel, they can alter the amplitude of the pixel by applying a linear phase retardation across each pixel.

2.2.5 Liquid crystal based Opto-VLSI processors

The core technology utilized in this thesis for the dynamic manipulation of the optical wavefront is the free-space Opto-VLSI processor (OVP), which consists of an array of liquid crystal (LC) cells, with a VLSI backplane [86, 87]. Liquid crystals are generally birefringent, where the optical axes of the two indices of refraction are controlled by an electric field across the LC cell. Therefore, by applying voltage across the LC cell, the index of refraction in the direction perpendicular to the plane of the cell can be altered [88].

Figure 2.6 shows the structure of a typical LC cell. There are two general types of liquid crystals:

Ferro-electric liquid crystals (FLCs): These are chemically described as chiral smectic C (Sc*) liquid crystals. They have only two stable birefringent orientations, and so allow for only two levels of optical phase modulation, thereby limiting the ability of the SLM to fully control the direction of the optical wavefront. However, these two states can be switched at relatively high speed (<1 μs), and so are desirable for OVPs where the speed of reconfiguration is required [89, 90].

Nematic liquid crystals (NLCs): Nematic liquid crystals typically respond to an applied field by changing the direction of the liquid crystal orientation, thereby allowing for continuous control of the phase retardation by a pixel. However, they respond relatively slowly (>10 ms) to the applied voltage, and so are useful when the speed of the SLM is not important [88].

The OVP can function both as a transmissive and reflective SLM. In the transmissive structure, both electrodes for the generation of the electric field across the LC cell are transparent to the working wavelength. The transparent electrode most often used is Indium-Tin Oxide (ITO), which is a well understood material, and is used in liquid crystal displays. For reflective OVPs, only one electrode is transmissive. The second electrode is made of highly reflective aluminum. The reflective SLM is more preferable since it allows for easy integration of the VLSI backplane below the reflective electrode.

The LC cells are addressed electronically, through use of row/column data addressing of random access memories (RAM). Figure 2.7 shows a typical layout and a cell design of an 8-phase OVP. When an address decoder line is active, the data decoder "loads" the three bit data describing the strength of the electric field onto the memory element of the cell, for all the cells in the row activated by the address decoder. Then at each cell, the a digital to analog converter is able to load the desired voltage onto the aluminum reflective electrode. The ITO is usually not pixellated and is kept at ground voltage.

The fabrication of OVPs is feasible in high-volume, since they require only standard VLSI processing technology for the silicon backplane and driving circuitry, as well as the reflective electrode. Similarly, the liquid crystal layers and ITO are assembled using the mature LC display process. Therefore OVPs are expected to be cost-effective when manufactured in significant quantities.

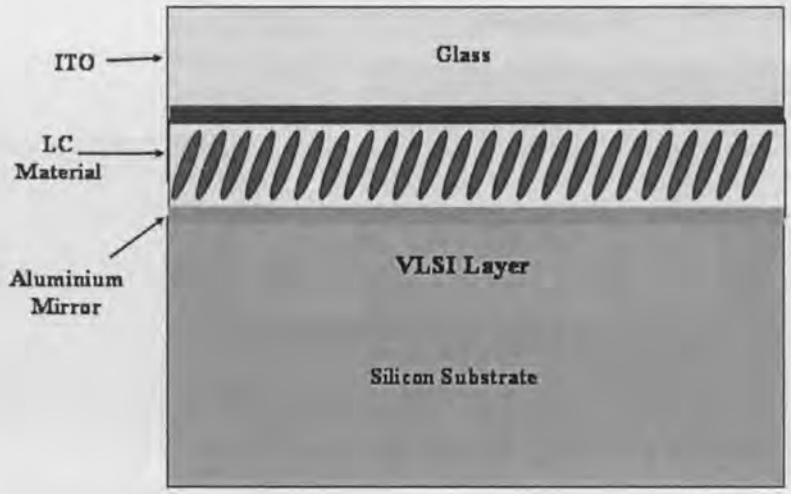

Figure 2.6: Liquid Crystal cell of the OVP

One of the key drawbacks of liquid crystal based OVPs is the sensitivity of the phase retardation of the LC cell to the optical polarization of the wavefront. This has in the past restricted the use of LC SLMs to cases when the polarization state of the input beam is stable. However, the addition of a quarter wave plate between the LC cell and the reflective electrode renders the LC cell polarization insensitive, and this has recently be demonstrated in the literature.

From Eq. (2.1), we can deduce that the maximum steering angle of an OVP is given by

$$\theta_{max} = \frac{\lambda}{2d} \tag{2.2}$$

where d is the pixel size, and λ is the wavelength. For example, an OVP having a pixel size of 5 μm can steer a 1550 nm laser beam by a maximum angle of around 8 degrees . The maximum diffraction efficiency of an OVP depends on the number of discrete phase levels that can be accommodated.

The theoretical maximum diffraction efficiency is given by [12]

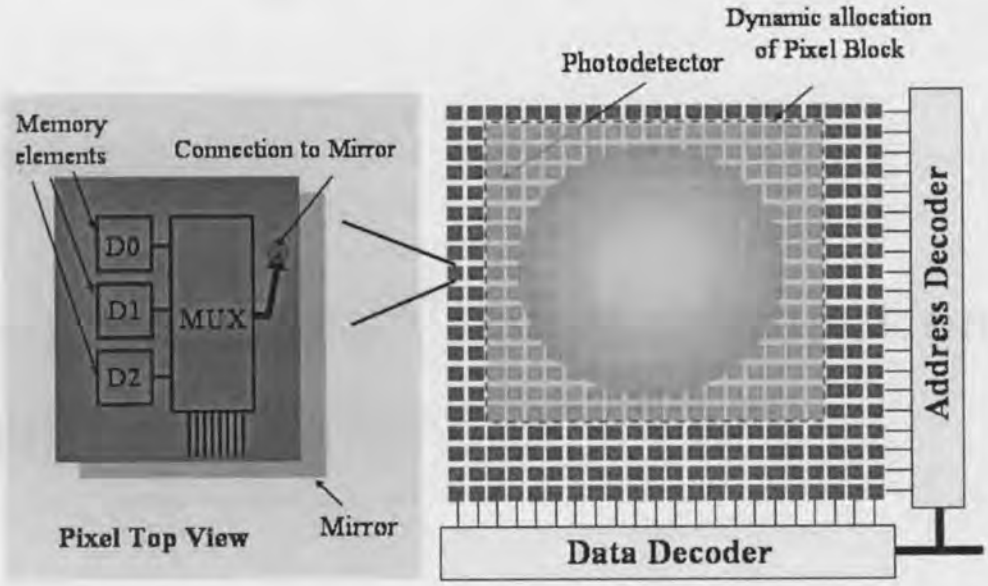

Figure 2.7: Layout of the OVP

$$\theta_{max} = \frac{\lambda}{2d} \tag{2.3}$$

where $n = gM + 1$ is the diffraction order ($n = 1$ is the desired order), M is the number of phase levels, and g is an integer.

Thus an OVP with binary phase levels can have a maximum diffraction efficiency of 40.5%, while a eight phase levels allow for efficiency up to 94%.

2.3 Conclusions

In this chapter, we have reviewed the various technology options for implementation of WDM networks, and attempted to provide a qualitative comparison of their suitability to various requirements of telecommunication systems. Further, we reviewed the basic approaches in use today for beam steering holography. In the next chapter, we present the proposed Opto-VLSI multifunction WDM device.

Chapter 3

Design of Opto-VLSI Multifunction WDM Device

The device proposed in this thesis is an Opto-VLSI based multifunction WDM Device, that would be able to perform several WDM network functions. This single component, we will show, can perform the functions of a dynamic optical gain equalizer and variable attenuator, tunable optical filter, a reconfigurable add/drop multiplexer and a 1×2 switch. We will also consider the multicasting capability of the OVP allowing for the function of channel monitoring, WDM channel multicasting for WDM network broadcasting services.

3.1 Description of Multifunction processor

The structure of the WDM multifunction Opto-VLSI Device (WDM-MD) is shown in Fig. 3.1. The WDM optical signal (WDM_{IN}) passes through an optical circulator and is collimated into a unguided Gaussian beam. The grating then disperses the beam, transmitting each wavelength channel in a different direction. The wavelength channels all arrive at different part of the OVP. Each area on which a beam arrives is steered independently. If the channel is intended to be passed on to the output (WDM_{OUT}), then the OVP steers the channel back exactly to retrace its path back to the grating, and then be coupled back into the collimator. The circulator then directs the beam to the WDM_{OUT} port. The OVP can attenuate the signal reflected back, by decreasing the size of the hologram, by decreasing the diffraction efficiency of the returned beam, or by changing slightly the steering angle. This therefore allows the functions of variable attenuation and channel-by-channel

gain equalization. Further, by placing holograms only in positions corresponding to the wavelengths of the filter's passband, and having no holograms at positions corresponding to the filters stopband, the function of a tunable filter is realized.

The second collimator is placed in a position, such that the beams dispersed by the grating, will have λ_{1B} channel coincide with λ_{1A} channel at the surface of the OVP, and likewise λ_{NB} channel coincide with λ_{NA} channel at the OVP. Thus by suitably choosing a beam steering direction, the added channel will be steered to the output port WDM_{OUT}. The drop channel essentially follows the same path in the opposite direction.

In a slightly different layout, as shown in Fig. 3.2, a single grating is used instead of two gratings. However, the two collimators must arrive at the grating at differing incidence angles. This can be accomplished by arranging the collimators at a converging angle between them, or placing a prism wedge in front of the second collimator. This layout will be considered in this chapter, since it will be the one most readily demonstrated experimentally. However, the analysis can easily be extended to the first layout.

In the following sections, we will look at the geometrical design of the functions in the multi-function processor.

3.2 Number of Channels

First we consider for one port, the number of channels that can be accommodated in the OVP, as shown in Fig. 3.3. Assuming that the angles are small, the beam size on the OVP is the same as the Gausian beam waist. Since the Gaussian beam arriving at the OVP extends to infinity, we need to consider the effect of the finite size of the hologram on the truncation of the beam. Tan et. al. [5] show that if the ratio of the hologram width to the beam radius, $\gamma \geq 3.06$, the truncation power loss, and diffractive losses would be minimal (at least 20 dB or less).

Therefore, the maximum number of channels possible on the processor is:

$$N \leq \frac{D_{OVP}}{3.06w} \tag{3.1}$$

where w is the Gaussian beam radius, and D_{OVP} is the width of the OVP.

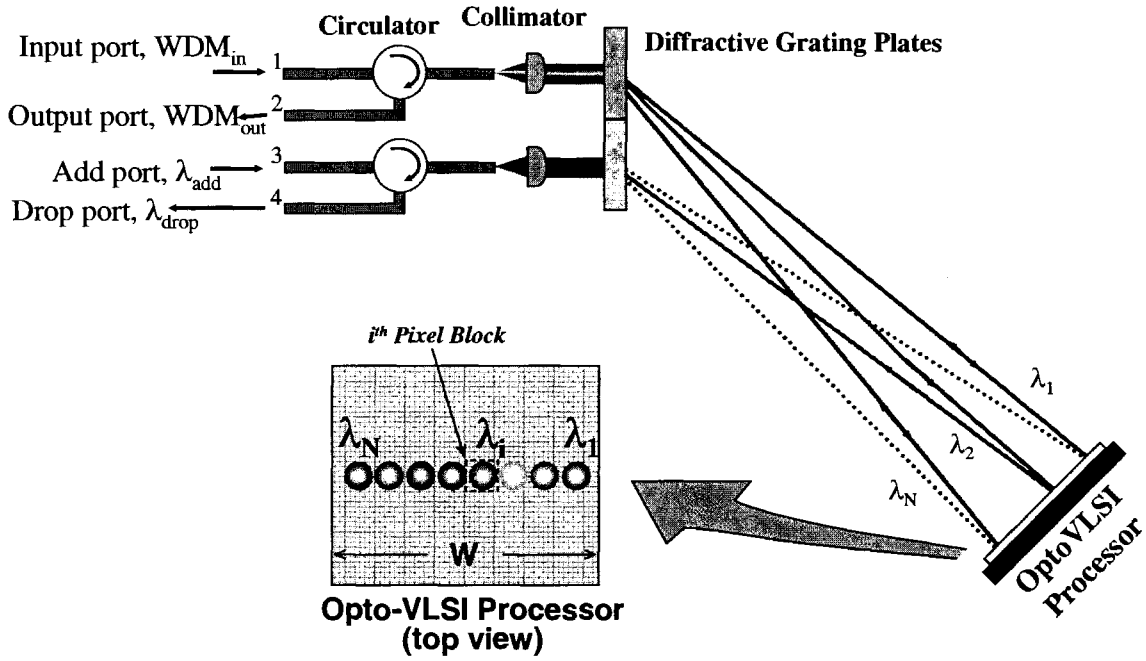

Figure 3.1: Two-grating Layout of Multifunction processor

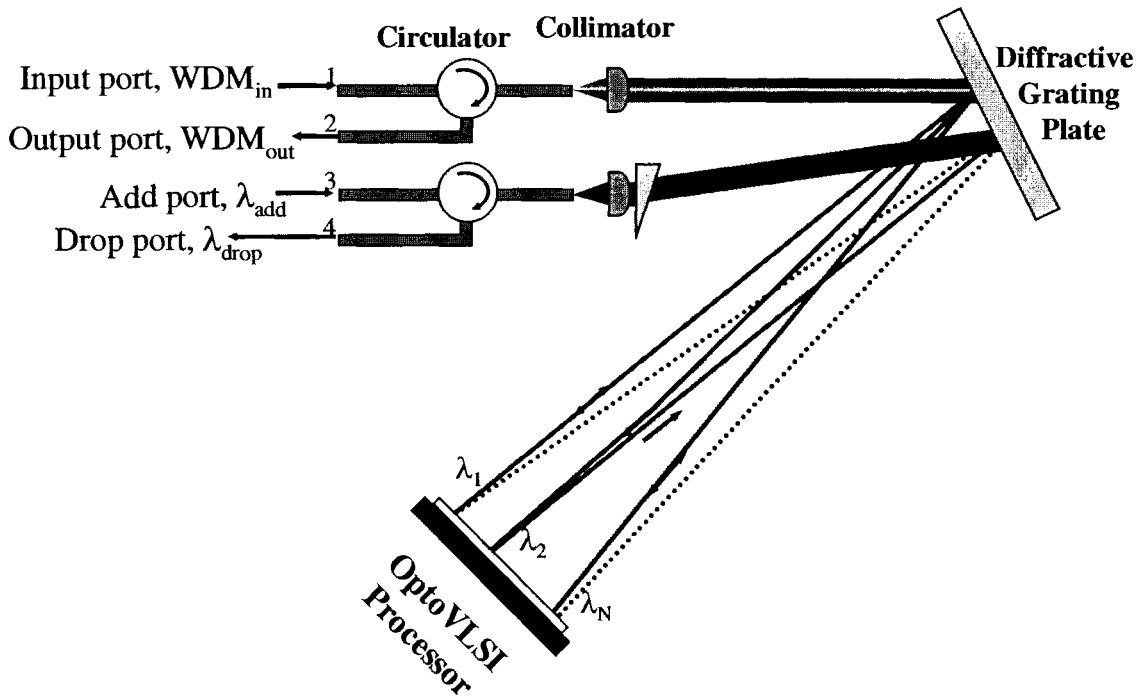

Figure 3.2: Single grating layout of Multifunction processor

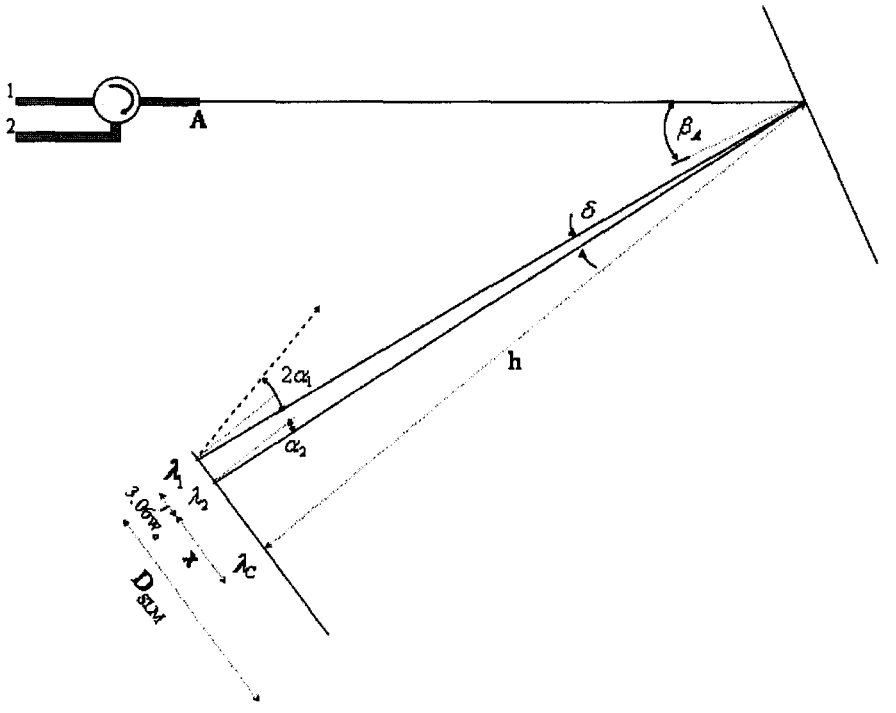

Figure 3.3: Determination of number of channels

3.3 Alignment of the OVP

Typically, the maximum steering angle of the OVP is limited, since the pixel size cannot be made arbitrarily small due to technological limitations. Therefore, careful alignment of the OVP is needed to utilize the available steering capability of the OVP. This can be accomplished by noting that the OVP can steer both in the $+\alpha$ and the $-\alpha$ directions. Therefore, by choosing the steering range of the OVP to span from $-\theta_{max}$ to $+\theta_{max}$ we can utilize the maximum steering possible.

If the center wavelength of the device $\lambda_c = \frac{\lambda_1+\lambda_N}{2}$ is designed to arrive at a normal incidence to the OVP, the maximum steering is required for λ_1 and λ_N, such that the maximum beam steering (as defined in Section 2.2.5) is not exceeded:

$$2\alpha_1 \approx -2\alpha_N \leq \theta_{max} \tag{3.2}$$

Therefore, from knowledge of θ_{max} of the OVP and D_{OVP} the length of the OVP, we can determine h, the maximum possible distance from the center of the OVP to the grating, that will allow both λ_1 and λ_N to be steered by the OVP. From simple geometry

of Fig. 3.4, we can see that the angle between λ_1 and λ_N at the grating is:

$$\Delta\alpha = \alpha_N - \alpha_1 = \sin^{-1}\left(\frac{\lambda_N}{d_g} - \sin\beta_A\right) - \sin^{-1}\left(\frac{\lambda_1}{d_g} - \sin\beta_A\right) \tag{3.3}$$

where d_g is the pitch of the grating. If α_N is small, we can approximate $\Delta\alpha$ by:

$$\Delta\alpha \approx \frac{\lambda_N - \lambda_1}{d_g} \tag{3.4}$$

Therefore, for the OVP to be able to steer a beam in its incident direction, we have to satisfy the following inequality, by controlling d_g and β_A:

$$\sin^{-1}\left(\frac{\lambda_N}{d_g} - \sin\beta_A\right) - \sin^{-1}\left(\frac{\lambda_1}{d_g} - \sin\beta_A\right) \leq \theta_{max} \tag{3.5}$$

If α_N is small, this reduces to:

$$\frac{\lambda_N - \lambda_1}{d_g} \leq \theta_{max} \tag{3.6}$$

At the best condition, the left-hand side of Eq. (3.5) would equal θ_{max}, thereby utilizing the full steering capability of the OVP. In such a condition, the normal distance from the center of the OVP to the grating, h will be:

$$h = \frac{D_{OVP}}{\tan\frac{1}{2}\left(\sin^{-1}\left(\frac{\lambda_N}{d_g} - \sin\beta_A\right) - \sin^{-1}\left(\frac{\lambda_1}{d_g} - \sin\beta_A\right)\right)} \approx \frac{2d_g D_{OVP}}{\lambda_N - \lambda_1} \tag{3.7}$$

For this layout, we can determine the steering required to send the beam back exactly along its incidence angle. This steering angle is denoted as θ_s. Since we have set that λ_c should arrive normal to the OVP, the steering angle for each channel θ_{s_i} should be:

$$\theta_{s_i} = 2\left(\frac{\Delta\alpha}{2} + \alpha_{A1} - \alpha_{Ai}\right) \tag{3.8}$$

3.4 Inter-channel wavelength spacing

The minimum inter-channel spacing can be determined from δ the inter-channel dispersion angle at the grating, as shown in Fig. 3.3. We define λ_1 and λ_2 as being separated by the smallest possible channel wavelength separation, $\Delta\lambda_{min} = |\lambda_1 - \lambda_2|$. From the geometric structure, we can see that:

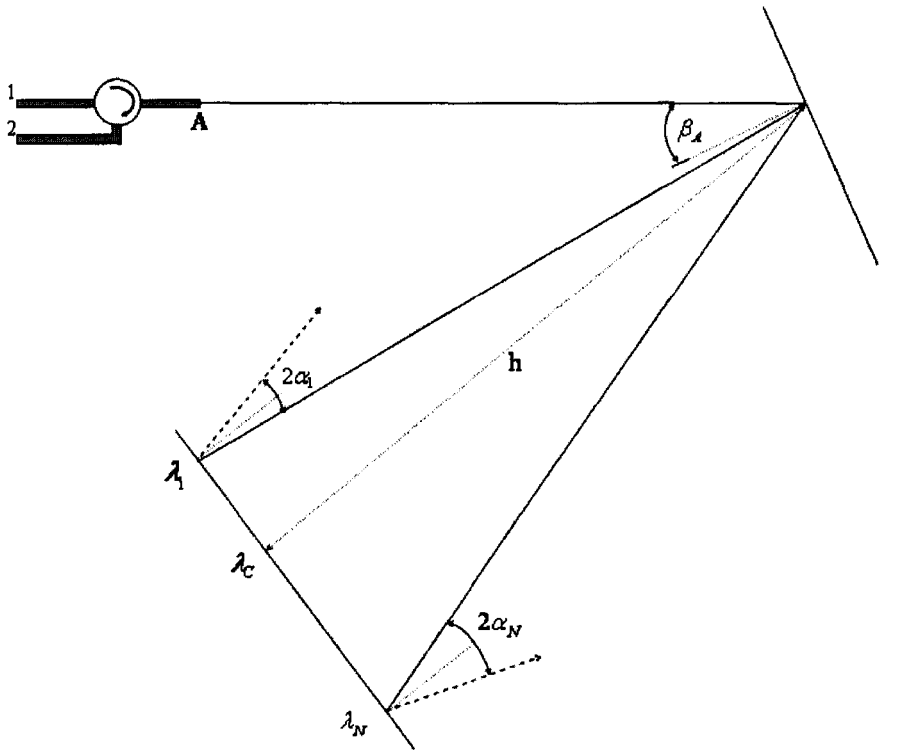

Figure 3.4: Positioning of the Center frequency

$$\delta = \alpha_1 - \alpha_2 \tag{3.9}$$

From Fig. 3.3 we can deduce:

$$\tan \alpha_1 = \frac{3.06w + x}{h} \tag{3.10}$$

and

$$\tan \alpha_2 = \frac{x}{h} \tag{3.11}$$

We can then get the minimum channel wavelength separation, by using the grating equation (Eq. 2.1):

$$\Delta\lambda_{min} \approx d_g \frac{3.06w}{h} \tag{3.12}$$

where h is the normal distance from the OVP to the grating.

3.5 Layout of the two collimator system

Up to this point, we have considered only the alignment of the system with the first collimator "A". In this section we consider the geometry when the second collimator "B" is included.

As explained in Section 3.1, for each wavelength, the beam from collimators "A" and "B" will need to meet at the OVP. From observing Fig. 3.2 carefully, we see that the orientation of the second collimator can be completely described by the distance between the beams "A" and "B" at the grating (which we define as D_1), and the angle between the two collimators, which we define as Θ_{AB}.

We can determine from geometry, that the angle between the two beams A and B from the collimators, is $\Theta_{AB} = \beta_A - \beta_B$. The constraint on the second collimator to be oriented correctly is that all its wavelengths arrive on the OVP, at exactly the position that they arrive from collimator "A". Specifically, we can set the first and last wavelength channels (λ_1 and λ_N) from the second collimator to arrive at the same position on the OVP as the same wavelength channels from the first collimator. For the normal distance of the meeting point from the grating position, this would require that:

$$h_{1A} = h_{1B} \equiv h_1 \tag{3.13}$$

and

$$h_{NA} = h_{NB} \equiv h_N \tag{3.14}$$

where h_{iA} and h_{iB} are the normal distance from the grating plane to the beam's intersection with the OVP plane for the i_{th} channel from collimator "A" and from collimator "B", respectively. Likewise, for the displacement on the plane of the grating from the point where beam "B" is incident, the requirement will be:

$$D_{2A_1} = D_{2B_1} \equiv D_{21} \tag{3.15}$$

and

$$D_{2A_N} = D_{2B_N} \equiv D_{2N} \tag{3.16}$$

where D_{2A_i} and D_{2B_i} are the displacements for wavelength channel i, on the grating plane from the point of incidence of the beam "B", at the OVP plane for the beam originating from "A" and from "B", respectively. Generally, for a beam for wavelength channel i, we can from trigonometric relations determine that:

$$h_i = \frac{D_1}{\tan \alpha_{Ai} - \tan \alpha_{Bi}} \tag{3.17}$$

and

$$D_{2i} = \frac{D_1 \tan \alpha_{Bi}}{\tan \alpha_{Ai} - \tan \alpha_{Bi}} \tag{3.18}$$

As was mentioned in Section 3.1, the beam for the i^{th} channel arriving at the OVP from collimator "A" will have to be steered to collimator "B". For this scenario, the steering required will not be θ_{s_i}, but rather the steering required from "A" to "B" (or vice versa), denoted by θ'_{s_i}, which from geometry considerations can be shown to be:

$$\theta'_{s_i} = \theta_{s_i} + \sin^{-1}\left(\frac{\lambda_i}{d_g} - \sin\beta_A\right) - \sin^{-1}\left(\frac{\lambda_i}{d_g} - \sin\left(\beta_A - \Theta_{AB}\right)\right) \tag{3.19}$$

From Eq. (3.19), we can determine that the maximum steering is required for λ_1 and the minimum steering is required for λ_N. Therefore, combining Eqs. (3.3), (3.8) and (3.19) we get:

$$\theta_{max} = \sin^{-1}\left(\frac{\lambda_N}{d_g} - \sin\beta_A\right) - \sin^{-1}\left(\frac{\lambda_1}{d_g} - \sin\left(\beta_A - \Theta_{AB}\right)\right) \tag{3.20}$$

In order to minimize the steering angle required, it is clear we need to minimize Θ_{AB}. In order to determine the effect of Θ_{AB} on the other parameter (D_1) that has effect on the orientation and position of collimator "B", we formulate, again based on geometrical consideration, a relation for the distance D_1:

$$D_1 = \frac{D_{OVP} \sin\alpha_{A1} \left(\tan\alpha_{A1} - \tan\alpha_{B1}\right)}{2\sin\left(\Delta\alpha/2\right)\tan\alpha_{A1}} \tag{3.21}$$

where α_{B1} is of course given by:

$$\alpha_{B1} = \sin^{-1}\left(\frac{\lambda_1}{d_g} - \sin\left(\beta_A - \Theta_{AB}\right)\right) \tag{3.22}$$

From Eq. (3.21) we can see that as Θ_{AB} decreases, D_1 also decreases, to the point where, if $\Theta_{AB} = 0$, then $D_1 = 0$. However, this is impossible, since collimators "A" and "B"

cannot occupy the same space. Therefore, the minimum angle Θ_{AB} will be determined by the minimum distance possible between the centers of the collimators. This will generally be determined by the size of beam from the collimators and the distance of the collimators from the grating. Assuming that the collimators will be brought close to the grating, then D_1 will have to be approximately equal to the chosen beam diameter for the system. We will further study the effects of beam diameter in Chapter 4.

3.6 Area of the Multifunction Device

In this section, we will consider the area of the multifunction processor. Achieving smaller "footprint" (smaller area) for a WDM device is an important design consideration for a few reasons:

- Can be accommodated in existing telecommunication device holders: "racks"
- Allows for easier integration with other WDM devices
- Can be designed more accurately to have mechanical integrity and temperature insensitivity

Therefore, we will consider the geometric parameters that affect the size of the WDM Multifunction Device (WDM-MD). First we define the minimum area of the WDM-MD, $\Re$ as the four sided area defined by the two lengths D_{OVP} and D_1. Of course, this does not include the two collimators. However, we justify this by noting that the collimators can come arbitrarily close to the minimum area defined, and so do not contribute to the minimum area possible. From simple geometry, the area $\Re$ is therefore:

$$\Re = \frac{1}{2}\left(h_N D_1 + h D_{OVP}\right) \tag{3.23}$$

where h is defined in Eq. (3.7). Inserting Eqs. (3.7) and (3.17) in Eq. (3.23), we get:

$$\Re = \frac{1}{2}\left\{\frac{D_1^2}{\tan\alpha_{AN} - \tan\alpha_{BN}} + \frac{D_{OVP}^2}{\tan\frac{1}{2}\left[\sin^{-1}\left(\frac{\lambda_N}{d_g} - \sin\beta_A\right) - \sin^{-1}\left(\frac{\lambda_N}{d_g} - \sin\beta_A\right)\right]}\right\} \tag{3.24}$$

Figure 3.5 shows the variation in area for various values of D_1, the separation between the beams from the collimators at the grating, as a function of the maximum steering

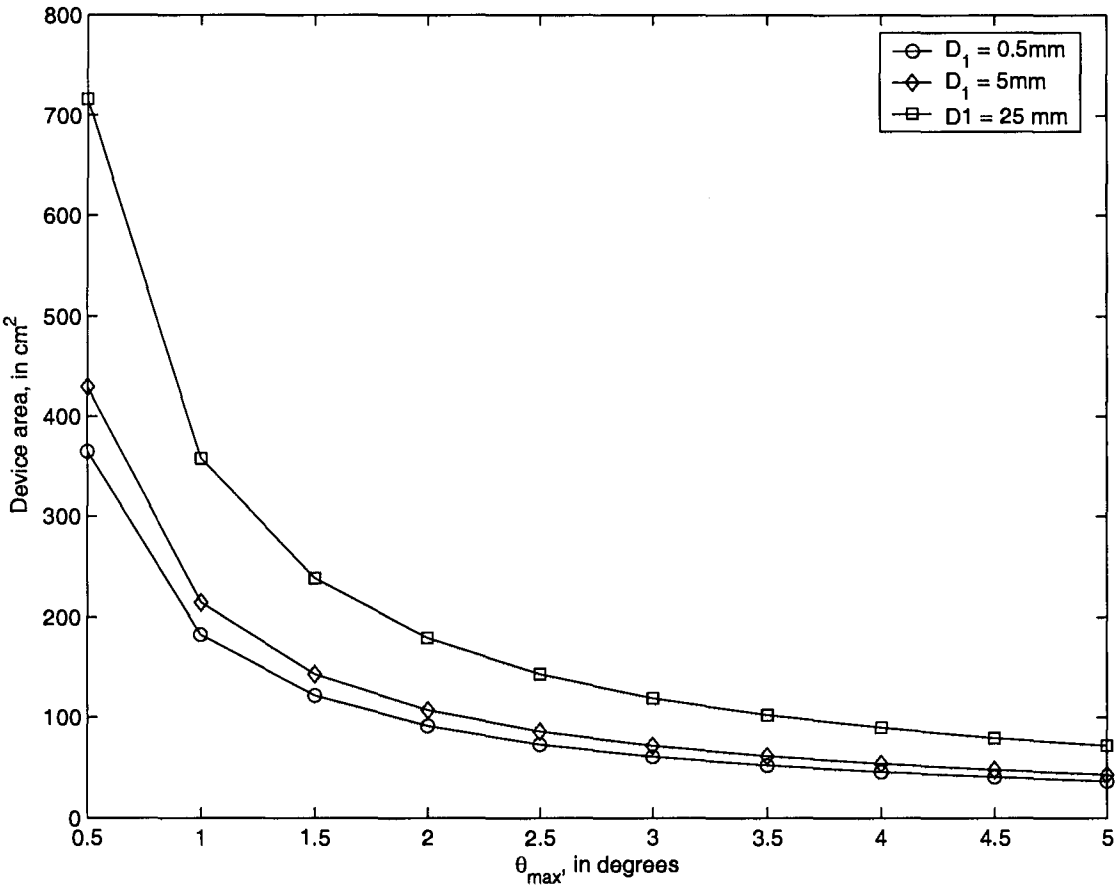

Figure 3.5: Area occupied by multifunction device as a function of D_1 and θ_{max}

angle θ_{max}. This calculation was made for $D_{OVP} = 25$ cm, $\lambda_1 = 1530$ nm and $\lambda_N = 1580$ nm, the beam radius $w = 0.25$ mm and number of channels $N = 100$. As the maximum steering angle increases, and varying the grating period, d_g, so that all the wavelengths between λ_1 and λ_N fall within the OVP.

In conclusion, the area of the WDM-MD is a strong function of the orientation of the two collimators, as determined by D_1, and the maximum steering capacity of the OVP. Therefore, if we increase the OVP's maximum steering angle (by decreasing the pixel pitch), the area of the device can be decreased. Further, decreasing D_1 decreases the area of the mulfunction processor. However, as was noted earlier, the value of D_1 cannot be less than that necessary to keep the two collimators separate. This in turn will be dependent on the size of the beam, which is discussed in Chapter 4.

3.7 Procedures for Designing WDM-MD devices

In this section, we describe a possible design procedures for realizing the multifunction device described and analyzed in the preceding sections.

1. Identify specifications of the multifunction device: the number of channels, N, as well as their wavelengths $\lambda_1, \lambda_2 \cdots \lambda_N$, in which the multifunction device will operate.

2. Identify technological constraints: the steering capability of the OVP, θ_{max} may be limited. Further, the period of the grating d_g may also be inflexible, if acquired off-the shelf.

3. Identify the beam width desired, w. Typically, $w \geq 0.25$ mm in order that the beam remain collimated and efficiently couple back into the collimators. If the path traveled by the beam is long (> 100 mm) the minimum value of w would need to also increase (as described in Chapter 4).

4. Calculate the required D_{OVP} and channel beam width such that Eq. (3.1) is satisfied.

5. Select values for d_g and β_A such that Eq. (3.5) is satisfied. If off-the-shelf gratings are used, the β_A would be the only free variable. Calculate $\Delta\alpha$ using Eq. (3.3).

6. Calculate h using Eq. (3.7).

7. Select the minimum value for D_1. This will be limited by how close the collimators can be to each other. Assuming the collimators are brought the closest possible to the grating without block the diffracted beam from the grating, the minimum value for D_1 will be: $D_1 \geq w$.

8. Choose a value for Θ_{AB}, such that Eq. (3.21) is satisfied. This ensures that the minimum area is taken by the multifunction device, since Θ_{AB} and D_1 are directly related.

9. Check that Eq. (3.20) is satisfied. If the right hand side of the equation is more than θ_{max}, go back to Step 5 and decrease d_g or increase β_A such that $\Delta\alpha$ is decreased. If the right hand side of Eq. (3.20) is less than 95% of θ_{max}, also go back to Step 5 and increase d_g or decrease β_A such that $\Delta\alpha$ is increased.

10. Calculate the area $\Re$ the area required for the device.

The above procedure is easily automated by programming into the computer. Using the procedure, a device is designed to work in the range 1530 nm to 1580 nm including 100 WDM channels, using an OVP with a commercially feasible pixel pitch of 7.4μm, corresponding to a $\theta_{max} = 6^o$. The results are listed in Table 3.1.

Specifications	
N	100
λ_1	1530 nm
λ_N	1580 nm
θ_{max}	6^o
Calculated values	
w	0.25 mm
D_{OVP}	25.00 mm
d_g	0.476μm (2100 lines/mm)
D_1	1.4 mm
Area	41 cm^2

Table 3.1: Calculated geometrical parameters of the multifunction processor for a set of specifications

3.8 Alternate design of multifunction device

One shortcoming of the WDM-MD design so far considered is that as we increase the desired number of channels and the wavelength range of the device, the steering angle needed also increases. This can severely limit the scalability of the device for dense-WDM (DWDM) systems. Therefore, we propose an alternative design of the Opto-VLSI based WDM Multifunction device (WDM-MD-A) is shown in Fig. 3.6.

3.8.1 Description of alternate design

In this design, the WDM_IN signal passes, as before, through the circulator and is collimated by the collimator at "A". The beam is incident on the center of the first lens (L_1). Therefore, the lens does not deflect the *direction* of the beam, however, it modifies the wavefront's radius of curvature. The beam then passes through a transmissive grating and is dispersed into its constituent wavelength channels. A second lens (L_2)is placed at a distance from the grating. The distance of the second lens from the intersection of beam "A" with the grating is set to be equal to its focal length (f_{L2}). The optical axis of the

second lens is set to coincide with the optical axis of the first lens. The incident angle of the beam "A" on the lens L_1 is chosen such that the the center wavelength channel from "A" is dispersed by the grating to be exactly along the optical axis. We denote this center wavelength, as usual, by λ_c, and is defined as:

$$\lambda_c = \frac{\lambda_1 + \lambda_N}{2} \tag{3.25}$$

where $\lambda_1, \lambda_2 \cdots \lambda_N$, are the N wavelength channels in the WDM system. From ray optics we conclude that all the wavelength channels will be incident on the OVP exactly normally. Therefore, the the OVP does not steer the channels. All the wavelength channels will return to the WDM_{OUT} port, retracing their paths in reverse. Therefore, this would function as filter, because the OVP can stop each channel by steering it in another direction. Further, considering the ability of the OVP to reflect the beam only partially, by either steering the beam back partially, or steering the beam slightly to decrease the coupling efficiency, the function of variable attenuation is realized, thereby allowing the device to work as a wavelength equalizer.

The second collimator ("B") is placed parallel to collimator ("A"), and so impinges on the first lens (L_1) off its optical axis. It is then deflected by the lens toward the optical axis of L_1 and L_2. Therefore, by choosing the focal length L_1 appropriately, the dispersed wavelength channel beams from collimator "B" also arrives at exactly the same points in the OVP. The angle at which they arrive at the OVP will no longer be normal. However, all channels from collimator "B" arrive at the OVP at *identical incidence angles.* Therefore, if a channel is to be added, the corresponding position at the OVP will steer it to return in the normal direction.

Another advantage of this design is that, as the collimators are parallel to each other, there can possibly be a many port device, by adding additional parallel collimators. All beams of the same wavelength channel from all collimators would arrive at the same spot in the OVP, but arrive at different angles of incidence (with collimator "A" as a special case having an angle of incidence of zero). Therefore, the functions of add/drop multiplexing is realized, since any channel from "A" can be steered to be or return to "A", and likewise for collimator "B" and any additional collimators. Further, the inclusion of additional collimators would allow a multiport cross-connect to be realized using a single grating and a collimator array.

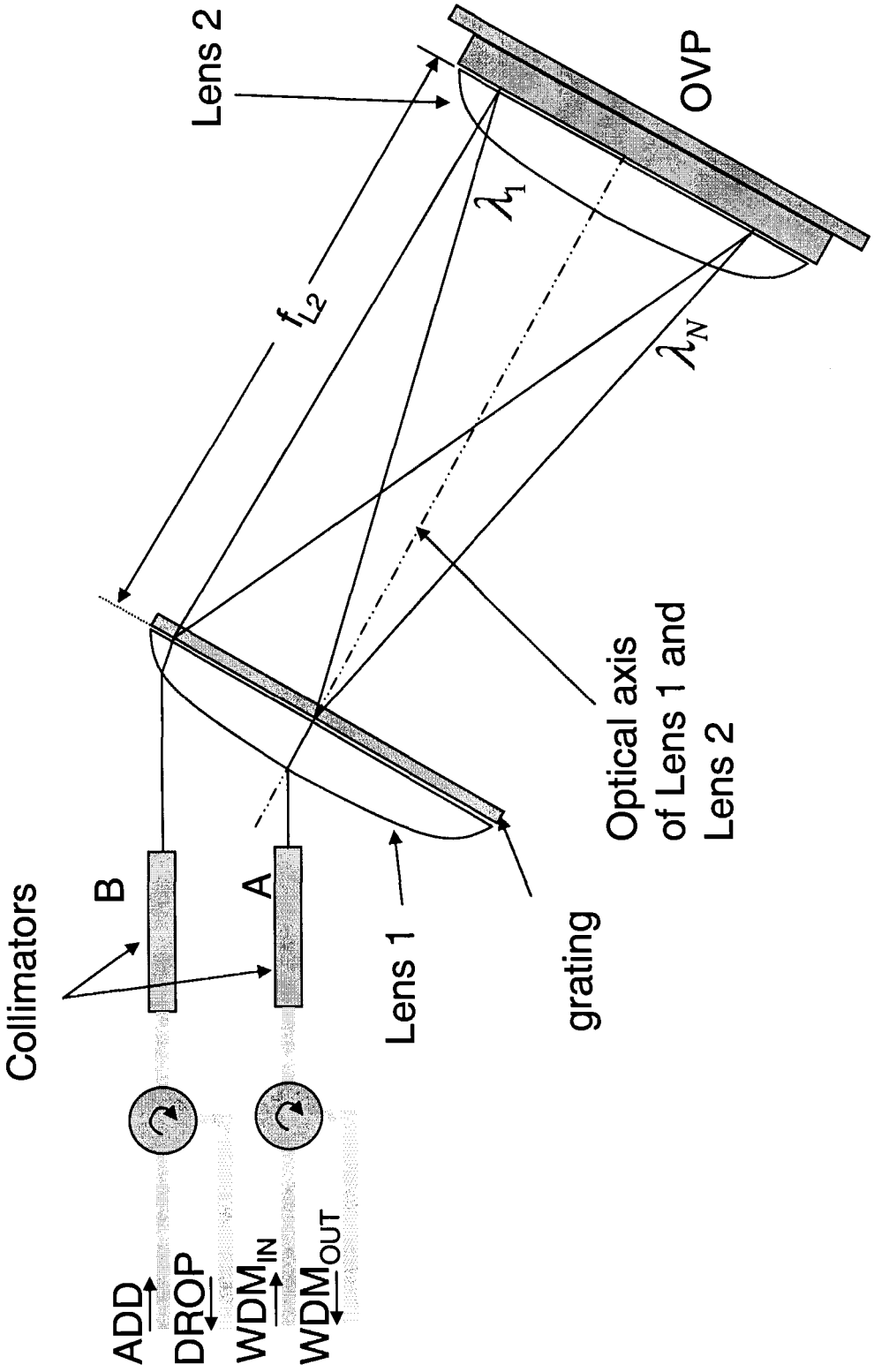

Figure 3.6: Alternate design of multifunction device

3.8.2 Geometry of alternate design

As noted in Section 3.8.1, the angle of incidence of the beam from collimator "A" on the optical axis of L_1 and L_2, denoted by β, remains unchanged by L_1. The value of β is chosen such that the center beam λ_c is diffracted in the direction of the optical axis of the L_1 and L_2. Therefore:

$$\beta_A = \sin^{-1} \frac{\lambda_c}{d_g} \tag{3.26}$$

where, as usual, d_g is the grating period. Assuming that D_{OVP}, the width of the OVP is fixed, we can determine the angle at which the beams will be diffracted by the grating for a range of wavelengths λ_1 to λ_N:

$$\alpha_{Ai} = \sin^{-1} \frac{\lambda_c - \lambda_i}{d_g} \tag{3.27}$$

Therefore, the acute angle between the diffracted λ_1 and λ_N channels, $\Delta\alpha$ will be:

$$\Delta\alpha = \sin^{-1} \frac{\lambda_N - \lambda_c}{d_g} + \sin^{-1} \frac{\lambda_c - \lambda_1}{d_g} \tag{3.28}$$

if the angles α_1 and α_N are small, we can again approximate $\Delta\alpha$ by:

$$\Delta\alpha \approx \frac{\lambda_N - \lambda_1}{d_g} \tag{3.29}$$

Therefore, from the knowledge of D_{OVP} we can determine the required focal length of the lens L_2, denoted by f_{L2}:

$$f_{L2} = \frac{D_{OVP}}{2\tan(\Delta\alpha/2)} \tag{3.30}$$

In order to determine the focal length of the lens L_1, we use the vector representation of beams in geometrical optics, where the beam is described by its declination gradient direction from the optical axis and its displacement from the optical axis. Therefore, we can describe the "ray" from collimator "B" incident on the lens L_1 as:

$$\mathbf{R_B^{L1^-}} = \begin{bmatrix} \frac{4\beta}{\pi} \\ d_{AB} \end{bmatrix} \tag{3.31}$$

where d_{AB} is the displacement from the optical axis of the incident beam from "B" on L_1. Since the collimators parallel, the angle at which the ray from collimator "B" is incident

on L_1, is the same as the incidence angle from collimator "A", β. The units of β has been changed from radians to gradient, through multiplying by a factor of $4/\pi$. This is because, at large incidence angles, the approximation $\sin\theta = \theta$ does not hold, and thus we convert the angle to gradient. The superscript of the the ray vector $\mathbf{R}$ simply describes the position of the ray, $L1^-$ denoting that it is arriving at L1, and the subscript "B" notes that the beam originates from collimator "B".

In order to describe the beam after passing through L_1, we multiply $\mathbf{R_B^{L1^-}}$ by the lens matrix, as described by the ABCD matrix formulation [1]. We use the thin lens approximation, where the lens is assumed to change the direction, but not the position of the ray passing through it. The ray vector after passing through the lens is:

$$\mathbf{R_B^{L1^+}} = \begin{bmatrix} 1 & -\frac{1}{f_{L1}} \\ 0 & 1 \end{bmatrix} \begin{bmatrix} \frac{4\beta}{\pi} \\ d_{AB} \end{bmatrix} = \begin{bmatrix} \frac{4\beta}{\pi} - \frac{d_{AB}}{f_{L1}} \\ d_{AB} \end{bmatrix} \tag{3.32}$$

Therefore, the beam from collimator "B" will be incident on the grating at the angle $\beta - \pi d_{AB}/4f_{L1}$. Therefore, the diffracted beams from collimator "B" will be:

$$\alpha_{iB} = \sin^{-1}\left[\frac{\lambda_i}{d_g} - \sin\left(\beta - \frac{\pi d_{AB}}{4f_{L1}}\right)\right] \tag{3.33}$$

Therefore, since the center wavelength λ_c impinges at the center of the OVP, we can determine the required focal length f_{L1} from the following implicit equation.

$$f_{L1} = \frac{\pi d_{AB}}{4\left[\beta - \sin^{-1}\left(\frac{\lambda_c}{d_g} - \frac{1}{\sqrt{1+\left(\frac{f_{L2}}{d_{AB}}\right)^2}}\right)\right]} \tag{3.34}$$

Similar to the original multifunction device, the area of the minimum area of the alternate design is simply the region between the lens/grating and the lens/OVP planes, since we can bring the collimators arbitrarily close to the lens/grating plane. We can express the area of the alternate device, $\Re'$ as:

$$\Re' = \frac{1}{2}\left[f_{L2}\left(D_{OVP} + d_{AB}\right)\right] \tag{3.35}$$

The above expression for $\Re'$ is simple: The area depends directly on the distance between the grating plane and the OVP, as well as the distance between the two collimators and the width of the OVP. The width of the OVP directly determines the number of channels that can be independently utilized by the device (as per Eq. (3.1)), and the value

of d_{AB} would, in any case, be made small compared to D_{OVP} if the collimators are close to each other. Therefore, the only free variable available to minimize $\Re'$ is the parameter f_{L2}. From Eq. (3.30), we determine that we can reduce f_{L2} by increasing $\Delta\alpha$, which in turn is increased by decreasing d_g. Therefore, there is a significant scope in reducing the size of the device by using more dispersive gratings. A practical performance limit for decreasing the size, of course, is aberrations introduced as f_{L2} is made small, while the diameter of L_2 must necessarily be kept at D_{OVP}, thereby creating more aberration.

Therefore in order to design the alternate multifunction processor layout, we can use the following procedure:

1. Identify the desired characteristics of the multifunction device as well as the inflexible device parameters. Examples for the former are the wavelength range $\lambda_1 - \lambda_N$, and number of channels. Some of the inflexible device parameters could be the technological limitations on the steering capability of the OVP, as well as the width of the OVP, D_{OVP}. In any case, the number of channels possible is determined using Eq. (3.1), and is directly dependent on D_{OVP} and the width of the beams from the collimators.

2. Choose suitable values of d_g and f_{L2}, such that Eqs. (3.28) and (3.30) are satisfied. If there is no technological constraint on d_g (for example, if it is possible to writing gratings on the substrate), then proceed to the next step.

3. Select a value for d_{AB} such that the space between the two collimators is minimized, as there is no advantage to having a larger device. In terms of the distance between the centers of the two collimators D_{AB}, the value of d_{AB} is simply:

$$d_{AB} = \frac{D_{AB}}{\cos\beta} \tag{3.36}$$

4. Calculate the value of f_{L1} using Eq. (3.34). If the value of d_g was not set in Step 2, choose suitable values of f_{L1} and f_{L2} based on focal lengths of easily available bulk lenses, such that Eqs. (3.30) and (3.34) are both satisfied. The area of the device will then be as given in Eq. (3.35).

Using a similar specification to that given in Section 3.7, we can determine the characteristics of the alternate design. Therefore, for $\lambda_1 = 1530$ nm, $\lambda_N = 1580$ nm and $N = 100$.

As explained earlier, the actual steering capability of the OVP is not important, and so we only set the size of the OVP, $D_{OVP} = 25$ mm. For these values, in order to obtain a device area $\Re = 40$ cm^2 (roughly the area of the original multifunction device designed) we can set $d_{AB} = 0.5$ mm, $\Delta\alpha = 4.47^o$, $f_{L2} = 32$ cm and $d_g = 0.65\mu$m. As can be seen from the procedure, this alternative design gives the designer more flexibility in decreasing the size of the device without compromising the specifications, since, irrespective of θ_{max}, by simply increasing $\Delta\alpha$ it will be possible to decrease the size of the device.

3.9 Advantages of the multifunction structures

We have thus far described geometrically the operation and some of the constraints on the two multifunction WDM device designs. Before proceeding to analyze more deeply the WDM multifunction device in the next chapters, we pause here to review some of the salient features of these two multifunction WDM device structures proposed, in comparison with other existing WDM reconfigurable components.

Channel Reconfiguration: Since the OVP is simply an array of pixels, there is no physical boundary between the adjacent channels. The channels are defined by the steering hologram displayed on the area that the beam falls on. Therefore, it is possible, without physically changing any parameter of the device, to change the position of the channels – so long as the new channels are within the wavelength range of the device. This capability of the multifunction processor is important, since the WDM device may be required to adhere to different channel wavelength standards depending on the network it is used in. This is not possible in other Free-space WDM devices, such as MEMS components, since the position of the mirrors must necessarily be fixed.

Multicasting Capability: Another unique capability of the multifunction WDM device is its ability to multicast a wavelength channel to more than one port. Multicasting devices can have a dramatic effect on the efficiency of networks, since a considerable portion of data services, especially multimedia services, have multiple destinations. Another use of multicasting would be in access networks, where a single wavelength channel can be shared between many communications customers. Finally, multicasting can be used to monitor data traffic congestion and troubleshoot dead links.

Integrated Variable Channel Attenuation: Another advantage of the multifunction device is its ability to dynamically attenuate the power of a wavelength channel, by

either decreasing the proportion of the beam's area that is steered, or by steering the beam slightly off its intended path, thereby decreasing the wavelength channel's coupling into the collimators. The attenuation can be controlled finely, since each pixel of the beam steering hologram can either be part of the hologram or not. Further, the OVP's steering angle can be controlled finely using computer generated holograms (see Chapter 5). Other WDM reconfigurable devices, such as Bragg-gratings and AWG based multiplexers, need to integrate a separate device for variable attenuation, in order to realize dynamic channel equalization. Likewise, MEMS WDM devices, although able to steer the beam slightly to couple less power into the collimator, do not exhibit a fine attenuation resolution cite-memsvariablecoupling.

Scalability: Although the scalability of the first multifunction design is limited by the ever increasing steering capability required of the OVP (see Eq. (3.5)), the alternative design proposed does not suffer from this shortcoming. Therefore, in the alternative design, while the number of channels and the size of the OVP, D_{OVP} increase, no increase in θ_{max} is needed.

Mechanical Integrity: Since the multifunction processor, unlike MEMS WDM devices, has no moving parts, it is potentially more durable. It is more stable since its solidity does not make it sensitive to mechanical vibrations. Again, since it has no moving parts, it can easily be integrated in a optical substrate, thereby protecting it from environmental contamination, similar to AWGs and other waveguided components.

3.10 Conclusions

We have in this chapter introduced the functioning of the WDM Multifunction processor, its geometrical properties, and related design parameters. We have also proposed a second alternative design using OVPs, which addresses some of the shortcomings of the first design. We presented a procedural approach to designing a WDM-MD devices, and compared some of their strengths with the strengths of competing approaches to WDM devices.

In Chapter 4, we will analyze the propagation properties of the WDM device using more accurate scalar diffraction based models, rather than the simple first approximation geometrical optics "rays" considered in this chapter. Next, we will devote Chapter 5 to algorithms for creating efficient "hologram" patterns for beam steering and multicasting applications. Finally, in Chapter 6, we experimentally demonstrate the operation of the

WDM multifunction devices.

Chapter 4

Analysis of Beams Diffracted from OVP

In this chapter, we review the relevant optical relations used to analyze the behavior of an optical beam and proceed to use them for analysis of the insertion loss of the system through investigation of the coupling loss of the output collimators, as well as study of parameters affecting the filter response of the multifunction device and the crosstalk isolation between adjacent wavelength channels.

4.1 Theoretical Basis

This study will use the scalar diffraction theory to model the optical systems, and quantify the error introduced by the simplifications made. The Rayleigh-Sommerfeld diffraction formula allows us to calculate the diffracted wave at any point $U(P_0)$ from knowledge of the field at all points in the aperture Σ:

$$U(P_0) = \frac{1}{j\lambda} \int\int_{\Sigma} U(P_1) \frac{e^{jkr_{01}}}{r_{01}} \cos(\vec{n}, \vec{r_{01}})\, ds \tag{4.1}$$

where the various symbols are described in Fig. 4.1. The derivation of Eq. (4.1) is shown in Appendix B. In this section we will provide the theoretical framework for analysis of the holographic beam-steering network, which is the scalar diffraction theory, and use it for analyzing coupling efficiency and cross-talk analysis between the collimator ports of the WDM multifunction device.

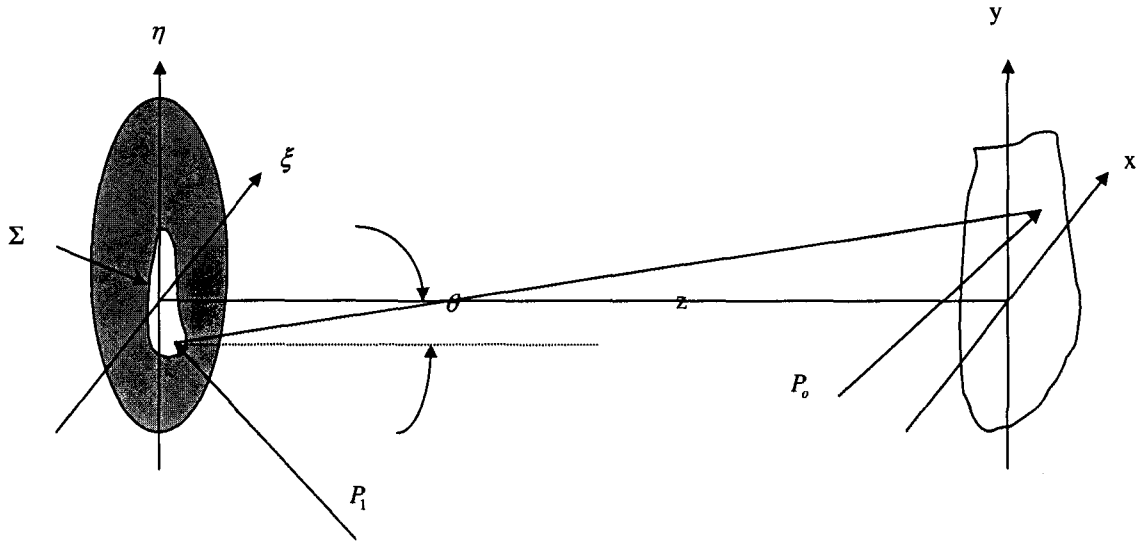

Figure 4.1: General layout for scalar diffraction analysis

4.1.1 Fresnel Integral

We can make a useful approximation of Eq. (4.1) by looking at Fig. 4.1. From the above figure, we can evaluate:

$$\cos(\vec{n}, \vec{r}_{01}) = \cos(\theta) = \frac{z}{r_{01}} \tag{4.2}$$

and

$$r_{01} = \sqrt{z^2 + (x-\xi)^2 + (y-\eta)^2} \tag{4.3}$$

approximating by using the first two terms of the binomial expansion, $\sqrt{1+b} = 1 + \frac{1}{2}b - \frac{1}{8}b^2 + \cdots$ we get

$$r_{01} \approx z\left(1 + \frac{1}{2}\left(\frac{x-\xi}{z}\right)^2 + \frac{1}{2}\left(\frac{y-\eta}{z}\right)^2\right) \tag{4.4}$$

and finally we get the Fresnel diffraction integral

$$U(x,y) = \frac{e^{jkz}}{j\lambda z}\int\int_{\Sigma} U(\xi,\eta)\, e^{j\frac{k}{2z}\left((x-\xi)^2+(y-\eta)^2\right)} d\xi d\eta \tag{4.5}$$

This approximation, if we express it simply as saying that the third term of the binomial expansion $\frac{1}{8}b^2$, is much less than the first two terms, needs to satisfy [91]:

$$z^3 \gg \frac{\pi}{4\lambda}\left((x-\xi)^2 + (y-\eta)^2\right)^2_{\max} \tag{4.6}$$

4.1.2 Fraunhofer Diffraction Formula

For very large values of z, if the following inequality is satisfied,

$$z \gg \frac{k\left(\xi^2+\eta^2\right)_{\max}}{2} \tag{4.7}$$

then we can make the following further approximation:

$$\exp\left(j\frac{k}{2z}\left(\xi^2+\eta^2\right)\right) \approx 1 \tag{4.8}$$

Therefore, we can make further simplify Eq.(4.5) into the following relation, known as the Fraunhofer diffraction formula:

$$U(x,y) = \frac{e^{jk\left(z+\frac{1}{2z}\left(x^2+y^2\right)\right)}}{j\lambda z}\int\int_{\Sigma} U(\xi,\eta)\, e^{-j\frac{2\pi}{\lambda z}(x\xi+y\eta)} d\xi d\eta \tag{4.9}$$

It can be seen that the above Fraunhofer formula has the added advantage of being in the form of a scaled Fourier transform relation. None the less, both the Fresnel and Fraunhofer relations require a considerable level of mathematical complexity.

4.1.3 Simplification using Operator Algebra

In order to simplify the evaluation of multi-component optical systems, we adopt the use of an operator algebra notation, where we use four operators that can describe the Fresnel and Fraunhofer regimes, as well as lenses. The relationship between the operators is described in Goodman [91]. The operators themselves in one-dimension (for simplicity) are shown below:

$$Q[c]\{U(x)\} = \exp\left(j\frac{k}{2}cx^2\right)U(x) \tag{4.10}$$

$$\nu[b]\{U(x)\} = b^{1/2}U(bx) \tag{4.11}$$

$$F\{U(x)\} = \int_{-\infty}^{\infty} U(x)\exp\left(-j2\pi fx\right)dx \tag{4.12}$$

$$R[d]\{U(x)\} = \frac{1}{\sqrt{j\lambda d}}\int_{-\infty}^{\infty} U(x_1)\exp\left(j\frac{k}{2d}(x_2-x_1)^2\right)dx_1 \tag{4.13}$$

As can be seen from Eq. (4.5), $R[d]$ is the Fresnel integral in one dimension, i.e. free-space propagation by a distance d. The quadratic phase operator $Q[c]$ can be thought of as transmission through a thin lens, where the operator parameter $c = -\frac{1}{f}$ for a converging lens of focal length f. The Fourier transform F and the scaling operator ν can then be combined with the quadratic phase factor Q to yield a relation for R:

$$R[d] = Q\left[\frac{1}{d}\right] v\left[\frac{1}{\lambda d}\right] FQ\left[\frac{1}{d}\right] \tag{4.14}$$

4.1.4 Gaussian Beam Propagation

In this section, we will review the basic relations for the propagation of a Gaussian beam. A paraxial beam is one that has no field component along its propagating direction, and varies slowly along the other two directions. A 1-D solution of the paraxial Helmholtz equation traveling in the z direction is of the form [1]:

$$U(x) = A_o \frac{w_o}{w(z)} \exp\left(-\frac{x^2}{w^2(z)}\right) \exp\left(jkz + jk\frac{x^2}{2R(z)} - j\xi(z)\right) \tag{4.15}$$

where

$$w(z) = w_o\left[1 + \left(\frac{z}{z_o}\right)^2\right]^{1/2} \tag{4.16}$$

$$R(z) = z\left[1 + \left(\frac{z_o}{z}\right)^2\right] \tag{4.17}$$

$$\xi(z) = \tan^{-1}\frac{z}{z_o} \tag{4.18}$$

$$w_o = \left(\frac{\lambda z_o}{\pi}\right)^{1/2} \tag{4.19}$$

The term w is termed the width of the beam and describes the distance from the center of the beam that the beam's intensity decreases to $1/e^2$. The waist w_o is the smallest width that the beam displays when propagating in isotropic medium. The Gaussian beam can also be described more easily using three "rays". A "central" ray that points in the direction of the propagation of the beam, as well as two "divergence" rays diverging from the center ray at the waist. The divergence angle of the two rays from the central ray is given by:

$$\theta_o = \frac{2\lambda}{\pi 2 w_o} \tag{4.20}$$

At points that are distant from the waist, the two divergent rays describe the width of the beam in either direction.

4.2 Beam Coupling into Collimator

In this section we will study various aspects of the WDM multifunction processor that have effect on the insertion loss of the device. First we will review the model that we will use to study the coupling efficiency into the collimators. In Section 4.2.2 we will study the effect of the number of pixels in the hologram on the coupling efficiency of the diffracted beam. Then in Section 4.2.3, we will study the effect of the beam offset from the axis of the collimators.

4.2.1 Coupling into the Fiber Propagating Mode

In this section, we calculate the coupling of offset and tilted gaussian beams into single mode fibers. The coupling ratio of a field distribution into any mode of a waveguide is determined from the so-called "overlap integral":

$$\eta_o = \frac{\left| \int\int_{-\infty}^{\infty} U(x,y)\, U_o^*(x,y)\, dxdy \right|^2}{\int\int_{-\infty}^{\infty} |U(x,y)|^2\, dxdy \int\int_{-\infty}^{\infty} |U_o(x,y)|^2\, dxdy} \tag{4.21}$$

where $U(x,y)$ is the field distribution incident on the fiber, and $U_o(x,y)$ is the description of the propagating mode in the fiber.

An analytical evaluation of the above relation is usually not feasible. Therefore, we use the analytical approximation of Eq. (4.21) developed by Marcuse [92].

If step index fiber waveguide, of core radius a, core index n_1 and cladding index n_2 would have a single mode propagating Gaussian beam of waist radius w_o of:

$$w_o = a\left[0.65 + \frac{1.619}{V^{1.5}} + \frac{2.879}{V^6}\right] \tag{4.22}$$

The normalized frequency, V, is given by the relation:

$$V = ka\sqrt{n_1^2 + n_2^2} \tag{4.23}$$

where $k = 2\pi/\lambda$ and a is the radius of the core of the fiber. It is possible to simplify Eq. (4.21), to a maximum error of a few percentage points, the power transmittance from a Gaussian beam that is tilted and offset, into a single mode fiber.

For a Gaussian beam that is offset but propagating parallel to the axis of the fiber, the power transmission coefficient, T_{off}, is [92]:

$$T_{off} = \frac{2w_o w}{w_o^2 + w^2} e^{-\frac{2d^2}{w_o^2+w^2}} \tag{4.24}$$

where w is the waist of the incident Gaussian beam, and d is the distance of the center of the incident Gaussian beam from the center of the fiber.

For a Gaussian beam that is incident exactly on the center of the fiber core, but tilted from the axis of the fiber core, the transmission coefficient, T_{tilt} will be:

$$T_{tilt} = \frac{2w_o w}{w_o^2 + w^2} e^{-\frac{(2\pi n_2 w w_o \theta_{tilt})^2}{(w_o^2+w^2)\lambda^2}} \tag{4.25}$$

where θ_{tilt} is the tilt angle between the optical axes of the fiber and the Gaussian beam.

Therefore, in general, the coupling efficiency for a beam that is tilted and offset with respect to the core of the optical fiber, $\eta_{o,\theta}$, will be given as follows:

$$\eta_{o,\theta} = T_{offset} T_{tilt} \tag{4.26}$$

As a curious consequence of the linearity of the system, it is possible to show that Eq. (4.21) can be computed from a description of the Gaussian beam at an earlier point and the back-propagation of the coupling (single) Gaussian mode to the same point, *provided* that all optical systems encountered are linear.

4.2.2 Effect of Number of Pixels

An important consideration in the analysis of the beam steering efficiency is the question: how many pixels are needed for each beam? In this section, we develop a method to determine the effect of the number of pixels on the coupling efficiency of the diffracted beam.

Consider the transmittance of a pixel. As indicated in Chapter 2, the pixel has a reflective/transmissive area, surrounded by a border that isolates it from its neighbors. For simplicity, considering one-dimension of a square pixel, it may be described as:

$$p(x) = \begin{cases} 1 & -1/2 \leq x \leq 1/2 \\ 0 & \text{elsewhere} \end{cases} \tag{4.27}$$

Therefore, the a pixel at a position $x = x_o$ with a length or width of a would be described by a "pixel function" $p\left(\frac{x-x_o}{a}\right)$. Therefore, the one dimensional pixel array, with M pixels, would be described by:

$$\mathbf{p}(x) = \sum_{m=1}^{M} p\left(\frac{x - x_m}{a}\right) e^{j\phi_m} \tag{4.28}$$

where $x_1, x_2 \cdots x_m \cdots x_M$ are the positions of the M pixels, and $\phi_1 \cdots \phi_M$ are the phase retardation of the pixels. Since the beam incident on the OVP has a Gaussian profile, and not a uniform field distribution, we define a Gaussian beam profile incident on the the pixel array $\mathbf{p}(x)$:

$$g(x) = g_{ovp} e^{-\frac{x^2}{w^2}} \tag{4.29}$$

where w is the radius of the Gaussian beam, and g_{ovp} is its intensity at the center of the beam. We choose, in Eq. (4.29), a Gaussian beam at its waist to reduce the complexity of the analysis by discarding the transverse phase factor. This is a reasonable choice, since the OVP is halfway along the optical path from the input collimator to the output collimator. In any case, the resulting beams will be close to Gaussian beams (as we will find at the end of this section), and thus, no generality is lost with this choice.

Therefore, the optical field distribution transmitted from the OVP, U_o has the profile:

$$U_o = \mathbf{p}(x) g(x) \tag{4.30}$$

In order to determine the diffraction from U_{ovp}, we compute its Fourier transform, A_{ovp}:

$$A_{ovp}(u) = F\{U_o vp(x)\} = P(u) \otimes G(u) \tag{4.31}$$

where $G(u)$ is the Fourier transform of the Gaussian beam profile, and is given by:

$$G(u) = g_{ovp} w \sqrt{\pi} e^{-\pi^2 w^2 u^2} \tag{4.32}$$

and the Fourier transform of the pixel array function $\mathbf{p}(x)$ is given by:

$$\mathbf{P}(u) = a\text{sinc}(au) \sum_{m=0}^{M} e^{-2\pi j x_m u + j\phi_m} \tag{4.33}$$

Finally, the Fourier transform of the field distribution can be expressed as:

$$A_{ovp}(u) = a g_{ovp} w\sqrt{\pi} \left[\left(\text{sinc}(au) \sum_{m=0}^{M} e^{-2\pi j x_m u + j\phi_m} \right) \otimes e^{-\pi^2 w^2 u^2} \right] \tag{4.34}$$

Next, in order to compute the diffraction efficiency, we use Parceval's identity on Eq. (4.21). Parceval's identity states that for any two functions $U_o(x)$ and $U_{ovp}(x)$, and their Fourier transforms $A_o(u)$ and $A_{ovp}(u)$, we can write:

$$\int_{-\infty}^{\infty} U_o(x) U_{ovp}^*(x) dx = \frac{1}{2\pi} \int_{-\infty}^{\infty} A_o(u) A_{ovp}^*(u) du \tag{4.35}$$

where $*$ indicates the complex conjugate. Therefore, we can write Eq. (4.21) as:

$$\eta_{pix} = \frac{\left| \int_{-\infty}^{\infty} A_o(u) A_{ovp}^*(u) du \right|^2}{\int_{-\infty}^{\infty} |A_o(u)|^2 du \int_{-\infty}^{\infty} |A_{ovp}(u)|^2 du} \tag{4.36}$$

The results of Eq. (4.36) can be numerically computed to give the effect of the number of pixels on the coupling efficiency of the diffracted beam. For example, we determine that for the maximum steering in the first diffraction order, we require a hologram pattern that has the largest spatial frequency, i.e, a pattern in two phase levels $0, \pi, 0, \pi \cdots$. The effect of the number of pixels on the coupling efficiency for such a pattern is computed and shown in Fig. 4.2. The parameters used for this calculation were $a = 30\mu$m, a pixel pitch of 40μm, and a Gaussian beam of beam radius of $w = 250\mu$m. As expected, increasing the number of pixels increases the coupling efficiency of the beam. For this particular case, increasing the number of pixels beyond 20 seems to have no advantage.

One can get a sense of the effect of the number of pixels from a careful observation of Eq. (4.34). We can observe that the summation term will, depending on the distribution of the phase of the pixel, tend to a series of peaks or δ-functions as the number of pixels increase. Therefore, for a sufficiently large number of pixels, it is possible to approximate the sinc function as being constant across each peak [93]. Therefore, the whole equation will be a series of Gaussian beams at the positions of the summation peaks. However, as the number of pixels decreases, the convolution will "distort" these Gaussian beams, and thereby decrease the coupling efficiency as seen in Fig. 4.3.

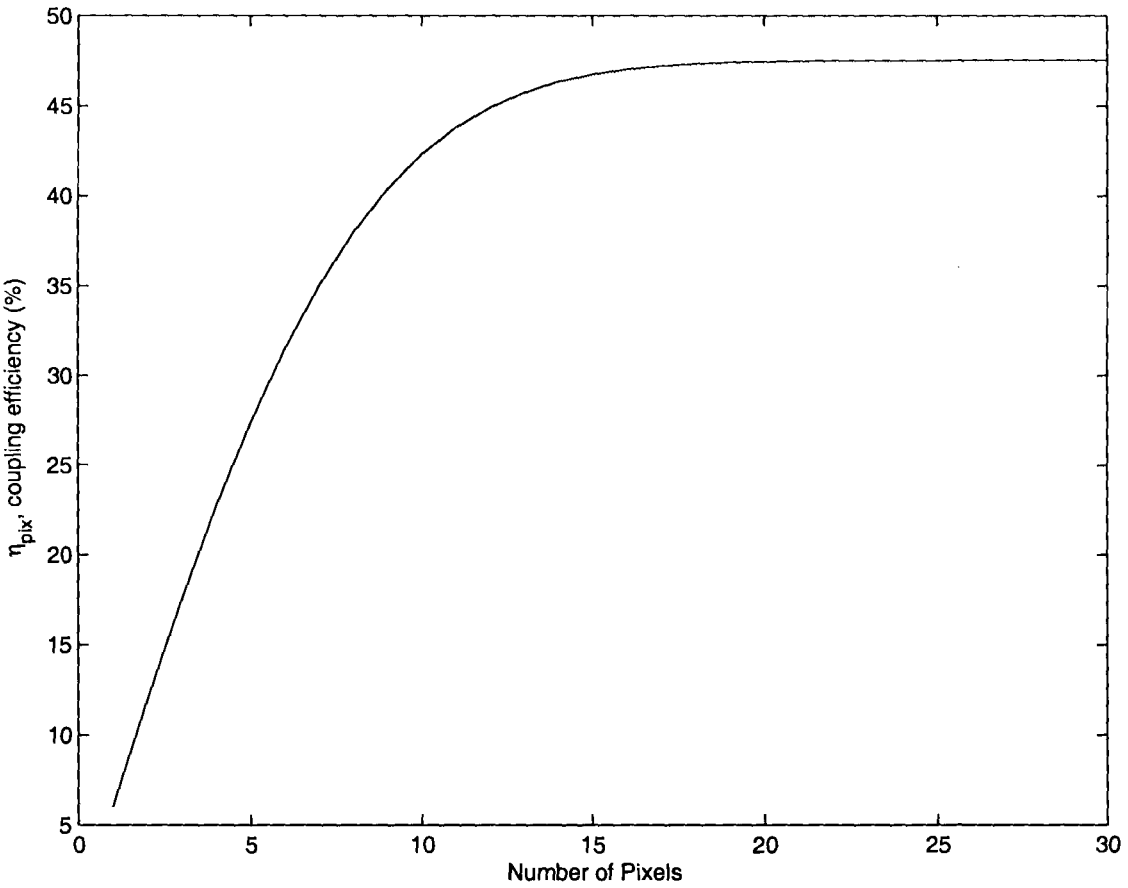

Figure 4.2: Coupling efficiency as a function of number of pixels

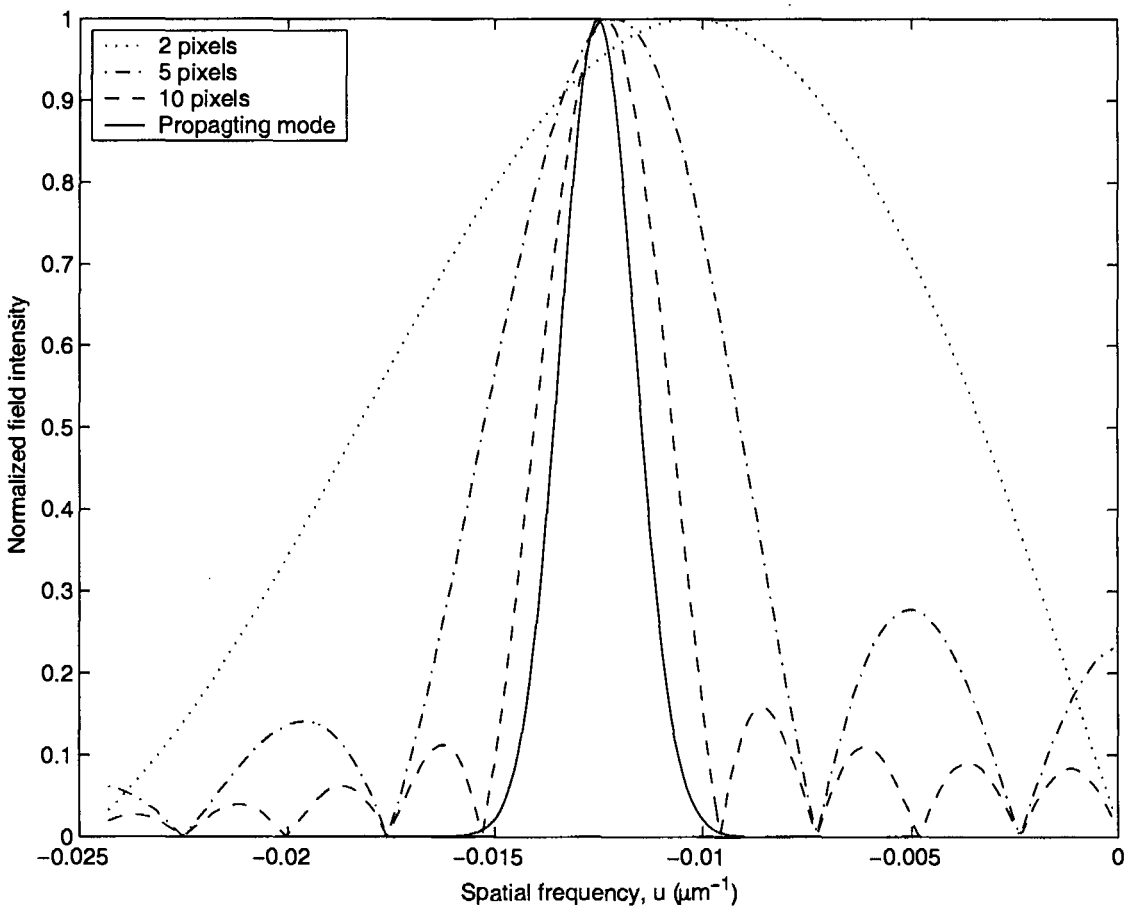

Figure 4.3: The Fourier transform of the propagating mode and of the field distribution for different number of pixels, A_{ovp}

We note in this regard that the removal of the transverse parabolic phase factor in Eq. (4.29) does not change the findings above. The effect of the phase factor on beam propagation would simply be to broaden the individual beams much as a lens would.

4.2.3 Optimization of loss due to offsets from Collimator axes

In Section 3.5 we set the position and orientation of the OVP and the second collimator "B", such that:

- Central beam from collimator λ_c falls normally on the center of the OVP.
- The distance h, of the OVP from the grating is set such that the channels use all space in the OVP (per Eq. (3.7)).
- The diffracted channel-beams from collimator "B" are set such that λ_1 and/or λ_N

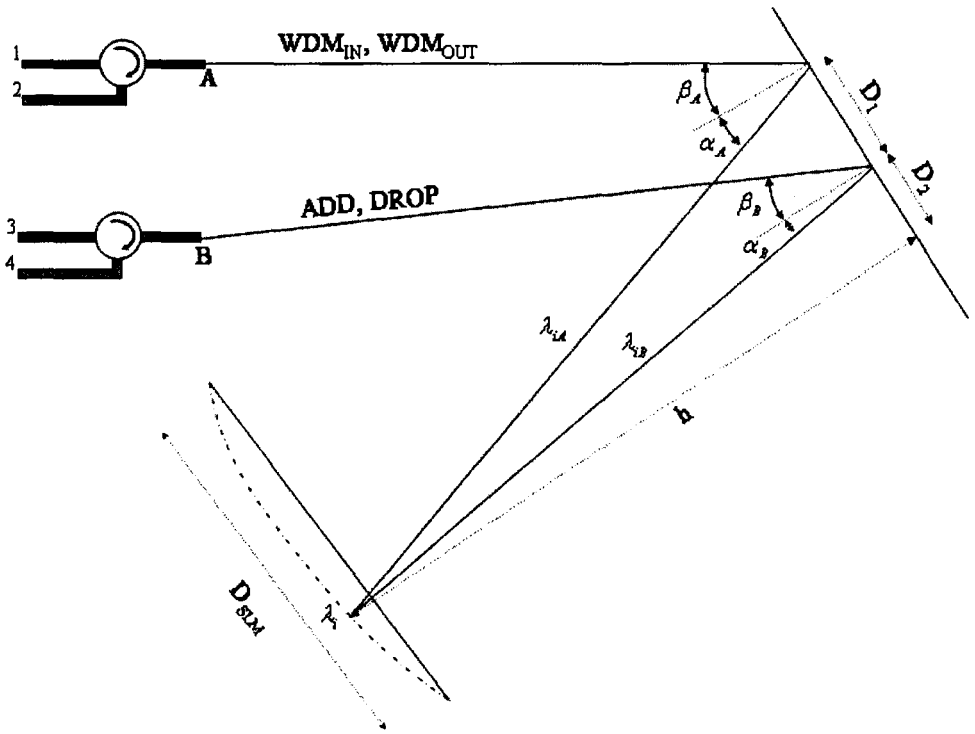

Figure 4.4: Discrepancy between SLM plane and meeting point of collimators A and B

arrive at exactly the same position on the OVP as the beam from collimator "A".

However, the above relations do not constrain the wavelength channels λ_i, for $1 < i < N$ from collimator "B" do not necessary arrive at exactly the same position as the corresponding channels from collimator "A". In fact, this is impossible if the OVP surface is planar. Therefore, there will be a small discrepancy between the point at which beams "A" and "B" arrive at the OVP plane, as shown in Fig. 4.4. This can be analyzed from the analysis of the relationship between D_2 and h. If we describe the distances D_2 and h in terms of trigonometric functions of the angles α_i and β_i, we would get the following relations for the positions as given in Eqs. (3.17) and (3.18). In order to simplify the analysis, we describe the OVP plane as a line that passes through the two points where λ_1 from collimators "A" and "B" and λ_N from the same two collimators meet. Mathematically, we can write:

$$y\left[h_1 - h_N\right] + x\left[D_{2N} - D_{21}\right] + D_{21}h_N - D_{2N}h_1 = 0 \tag{4.37}$$

where we have defined the co-ordinates x and y to originate on the point where beam from collimator "B" is incident on the grating. The positive direction of x is perpendicular to the grating plane and toward the OVP, i.e., along the direction of h_i. The positive direction of y is collinear with the grating plane, away from the length D_1, i.e., along the direction of D_{2i}. Again, the values of h_1, h_N, D_{21}, and D_{2N} are as defined in Eqs. (3.17) and (3.18).

Similarly, we can describe the beam from collimator "A" diffracted by the grating, in the i^{th} direction, as:

$$-yh_i + x\left[D_{2i} + D_1\right] - D_1 h_i = 0 \tag{4.38}$$

Further, the i^{th} channel diffracted from the grating which originated from collimator "B" can be described by the line:

$$-yh_i + xD_{2i} = 0 \tag{4.39}$$

Now, using Eq. (4.37) and (4.38), we can calculate for the i^{th} channel, the point at which the beam from collimator "A" intersects the OVP line. Using plane geometry, we get the y coordinate of the intersection point, which we designate y_{AO}:

$$y_{AO} = \frac{D_1 h_i \left(D_{2N} - D_{21}\right) + \left(D_{21} h_N - D_{2N} h_1\right)\left(D_{2i} + D_1\right)}{h_i \left(D_{21} - D_{2N}\right) - \left(D_{2i} + D_1\right)\left(h_1 - h_N\right)} \tag{4.40}$$

In a similar fashion, combining Eqs. (4.37) and (4.39), we calculate the point at which the beam from collimator "B" intersects the OVP plane. For the y coordinate of the intersection for the channel i, we get:

$$y_{BO} = \frac{D_{2i}\left(D_{2N} h_1 - D_{21} h_N\right)}{D_{2i}\left(h_1 - h_N\right) + h_i \left(D_{2N} - D_{21}\right)} \tag{4.41}$$

The distance between these two points projected *on the grating plane* and denoted by Δy will therefore be:

$$\Delta y = \left|y_{AO} - y_{BO}\right| \tag{4.42}$$

Assuming that the beams from "A" and "B" fall close enough on the OVP plane to be steered by the same hologram, the beam traveling from "A" to "B" will be parallel with the beam traveling from "B" (the line described by Eq. (4.39)). Similarly, the beam traveling from "B" to "A" will be parallel to the line described by Eq. (4.38). Therefore,

the displaced beams will arrive at their intended collimators, parallel to the axis of the collimator. However, they will be displaced by:

$$\Delta y_A = \Delta y \cos \beta_A \tag{4.43}$$

and

$$\Delta y_B = \Delta y \cos \beta_B \tag{4.44}$$

where Δy_A is the displacement of the beam from "B" from the axis of collimator "A" and Δy_B is the displacement of the beam from "A" from the axis of collimator "B".

Using the relations for coupling efficiency described in Section 4.2.1, we get:

$$\eta_A = e^{-\frac{\Delta y_A^2}{w^2}} \tag{4.45}$$

and

$$\eta_B = e^{-\frac{\Delta y_B^2}{w^2}} \tag{4.46}$$

Figure 4.5 shows the calculated offset from collimator "A" for all wavelength λ_1 to λ_N, for the geometry set in Table 3.1. Of course, at the two extremities there will be no offset, since the design set these two points to coincide. Further, for this example, since θ_{max} is small, there will be little effect on the coupling efficiency on the collimator, as given in Eqs. (4.45) and (4.46). However, as the value of d_g is decreased, thus making the grating more dispersive, and the value of $\Delta\alpha$ greater, the offset will decrease. Further, as the angle between the two collimators Θ_{AB} is increased, the offset increases.

4.3 Filter bandwidth

In this section, we will determine the filter response of the WDM Multifunction device. Without loss of generality, we assume that the OVP hologram dedicated to the steering of the wavelength channel in question, λ_i, is equal to the waist of the Gaussian beam incident on it, $2w$. Therefore, in the filter mode of the multifunction device, an incident beam is steered back to its incident direction, and any radiation reflected within the hologram is coupled (ideally) back into the collimator. However, as the wavelength of the incident

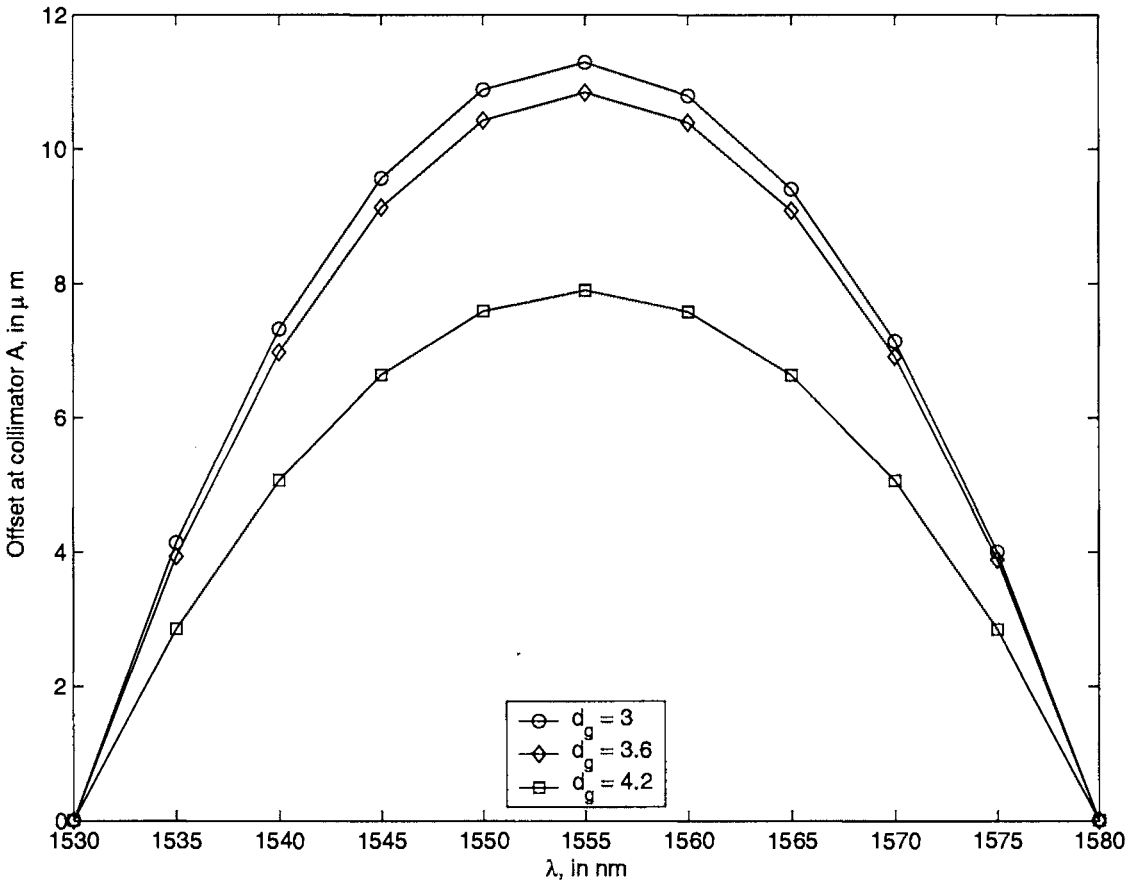

Figure 4.5: Calculation of offset at Collimator A for $\lambda_1 to \lambda_N$

beam changes to $\lambda_i + \Delta\lambda$, the amount of power coupled back into the collimator decreases for two reasons:

1. The grating will steer the beam $\lambda_i + \Delta\lambda$ away from the center of the hologram, thereby decreasing the portion of the beam that falls on the hologram, leading to less optical field that is reflected by the hologram.

2. The incident angle of $\lambda_i + \Delta\lambda$ on the OVP will be different from the steering angle of the hologram. Therefore, the beam will arrive at the collimator not normally, but with a tilt and offset.

Mathematically describing the above two wavelength effects will allow us to model the filter response of the device. First, we calculate the fraction of optical power falling within the hologram, η_{frac}. If the beam $\lambda_i + \Delta\lambda$ arrives on the OVP at a distance Δx away from the center of the hologram, then η_{frac} will be:

$$\eta_{frac} = \frac{\int_{\frac{w}{2}-\Delta x}^{\frac{w}{2}+\Delta x} e^{-\frac{x^2}{w^2}} dx}{\int_{-\infty}^{\infty} e^{-\frac{x^2}{w^2}} dx} \tag{4.47}$$

where w is the beam radius of the Gaussian beam, which is the same as the half-length of the hologram. The evaluation of Eq. (4.47) is easily facilitated by use of the error function, erf:

$$\eta_{frac} = \frac{1}{2}\left[\text{erf}\left(\frac{w-\Delta x}{w}\right) + \text{erf}\left(\frac{w+\Delta x}{w}\right)\right] \tag{4.48}$$

where the error function, whose numerical evaluation is convenient, is defined as:

$$\text{erf}(x) = \frac{2}{\sqrt{\pi}} \int_0^x e^{-t^2} dt$$

The displacement from the center of the hologram Δx, is of course a function of the wavelength. From the geometry of Fig. 3.4, Δx is given by the relation:

$$\Delta x = h \left| \tan\theta_{s_i} - \tan\theta_{s_{\lambda_i+\Delta\lambda}} \right| \tag{4.49}$$

where h is as given in Eq. (3.7) and steering angles θ_{s_i} is as given in Eq. (3.8). The last term, $\theta_{s_{\lambda_i+\Delta\lambda}}$ is given by:

$$\theta_{s_{\lambda_i+\Delta\lambda}} = \left[\sin^{-1}\left(\frac{\lambda_1+\lambda_N}{2d_g} - \sin\beta_A\right) - \sin^{-1}\left(\frac{\lambda_i+\Delta\lambda}{d_g} - \sin\beta_A\right)\right] \tag{4.50}$$

Similar to the analysis in Section 4.2.3, we can also from geometry determine the offset and tilt at the collimator "A" from a beam with wavelength $\lambda_i + \Delta\lambda$. The tilt of the beam at the collimator, Ψ_{tilt} can be shown to be:

$$\Psi_{tilt} = \sin^{-1}\left(\frac{\lambda_i+\Delta\lambda}{d_g} - \sin\left(\frac{\Delta\alpha + \theta_{s_{\lambda_i+\Delta\lambda}}}{2} - \theta_{s_i}\right)\right) - \beta_A \tag{4.51}$$

where $\Delta\alpha$ is as defined in Eq. (3.3). The offset at Collimator "A" from the $\lambda_i + \Delta\lambda$ beam can likewise be shown to be:

$$D_{offset} = \delta\cos\beta_A + (D_A - \delta\sin\beta_A)\sin\Psi_{tilt} \tag{4.52}$$

where δ is the offset of the diffracted beam on the grating, and is given by the following relation:

$$\delta = \frac{h\cos\left(\frac{\Delta\alpha-\theta_{s_{\lambda_i+\Delta\lambda}}}{2}\right)}{\cos\left(\frac{\theta_{s_{\lambda_i+\Delta\lambda}}}{2}\right)}\left[\tan\left(\frac{\theta_{s_{\lambda_i+\Delta\lambda}}+\Delta\alpha}{2} - \theta_{s_i}\right) - \tan\left(\frac{\Delta\alpha - \theta_{s_{\lambda_i+\Delta\lambda}}}{2}\right)\right] \tag{4.53}$$

Therefore, the coupling into the collimator "A" as a function of wavelength due to the fraction of the incident power reflected by the hologram, as well as the tilt and offset of the beam at the collimator can be combined using Eqs. (4.24), (4.25), (4.47), (4.51) and (4.52). The final coupling dependence on wavelength, η_{filter}:

$$\eta_{filter}(\Delta\lambda) = \eta_{frac} e^{-\frac{D_{offset}^2}{w^2}} e^{-\frac{(2\pi n_2 \Psi_{tilt})^2}{(\lambda_i+\Delta\lambda)^2}} \tag{4.54}$$

Again using the specifications in Table 3.1, we can compute the filter response of a typical wavelength. Figure 4.6 shows the response of the filter for three different Gaussian beam width, for $\lambda_i = 1555$ nm and $D_A = 100\mu$m. Therefore, we can choose the bandwidth of the filter by changing the Gaussian beam width. The bandwidth of the filter can be computed numerically from Eq. (4.54), by finding the bandwidth($2\Delta\lambda$) that decreases η_{filter} to half its maximum value.

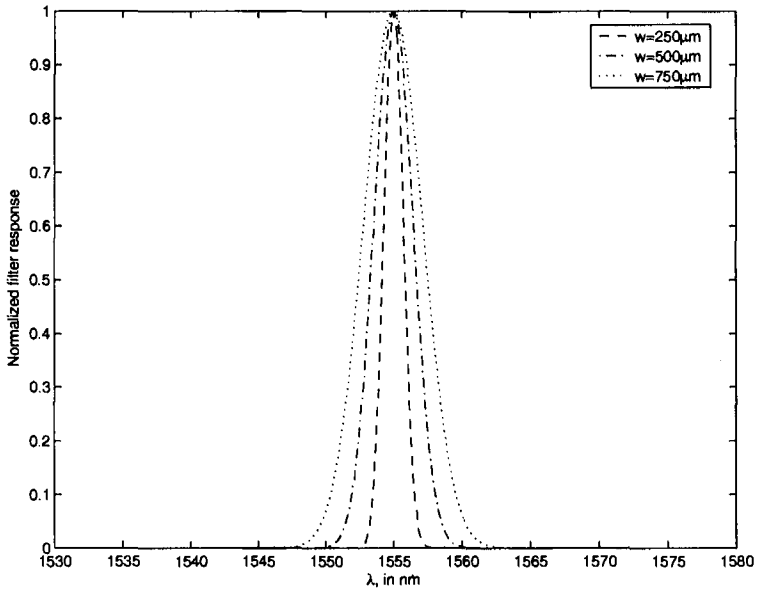

Figure 4.6: Filter response for three different Gaussian beam widths for a center wavelength of 1555 nm

4.4 Crosstalk Analysis

One shortcoming of diffractive optical systems is the non-ideal dispersion of the optical fields in directions not intended by the device. This tends to increase the cross-talk of the device, and thus degrade its performance. In this section, we attempt to quantify the implication of the architecture of the Opto-VLSI devices on crosstalk performance. Of course, the cross-talk performance of a device is ultimately dependent on the particular holograms loaded on the OVP. However, certain features of the device can have a significant effect on the performance of the device. Specifically, we note that if a two stage steering is available, for a generalized switching architecture, the crosstalk isolation performance can improve markedly. The multifunction WDM device may be considered a two-stage device category, since, it has two "steering" stages, with the first one being the OVP itself, and the second one the grating, which disperses the beams in differing directions, depending on their wavelength. However, the second "stage", which is the grating, does not have a fully controllable steering, and so it will not have the same flexibility of a true two stage device. However, the device described in Section 2.1.4.3, falls in the category of a one stage device, since the steering is available only at only one stage.

First we will consider a generalized beam switching system utilizing two steering stages, and show that, for a symmetric system, the analysis reduces to two stages of beam steering

separated by a distance, which is determined by the optical system between the two OVPs. Then, we will compare for an unintended diffracted beam (i.e. a beam that leads to crosstalk), its coupling path, for both the generalized one stage switch and the two stage switch.

4.4.1 General structures of a two stage device

Using the operator algebra described in Section 4.1.3, we now analyze the output of a beam steering scheme, including two lenses, as shown in Fig. 4.7, where one OVP steers the beam away from the normal, and a second OVP, encoded with a complex conjugate of the first, reverses the steering to the normal direction, at a lateral offset.

One can assume that the light at the first switch will be Gaussian, and can be completely described by the beam waist w_1 and the phase curvature R_1. Therefore, the question that remains is the nature of the propagation of the beam from the first to the second OVP. We can see from the analysis in the previous section that the propagation of the beam across free space can be computed using the Fresnel integral, while the phase curvature due to the two lenses can be expressed by the operator $Q\left[-\frac{1}{f}\right]$. The total system S will then be:

$$\begin{aligned} S &= R[d]\,Q\left[-\tfrac{1}{f}\right]R[2f]\,Q\left[-\tfrac{1}{f}\right]R[d] \\ &= R[d-f]\,R[f]\,Q\left[-\tfrac{1}{f}\right]R[f]\,R[f]\,Q\left[-\tfrac{1}{f}\right]R[f]\,R[d-f] \\ &= R[d-f]\,\nu\left[\tfrac{1}{\lambda f}\right]\Im\nu\left[\tfrac{1}{\lambda f}\right]\Im R[d-f] \\ &= R[d-f]\,\nu\left[\tfrac{1}{\lambda f}\right]\nu[\lambda f]\,\Im\Im R[d-f] \\ &= \nu[-1]\,R[2(d-f)] \\ &= R[2(f-d)] \end{aligned} \tag{4.55}$$

This result implies that the system between two OVPs with two lenses, is equivalent to a free space propagation by a distance of $2(f-d)$. The relationship between the two SLMs then can be simplified as shown in Fig. 4.8.

To analyze the system shown in Fig. 4.8, we use a normalized Gaussian beam as input

$$G_1(x) = \frac{1}{w_1\sqrt{\pi}}\exp\left(-\frac{x^2}{w_1^2}\right) \tag{4.56}$$

Further, let the hologram on the first switching stage be denoted by H_1. We can then express the field arriving at the second stage as U_{2-}

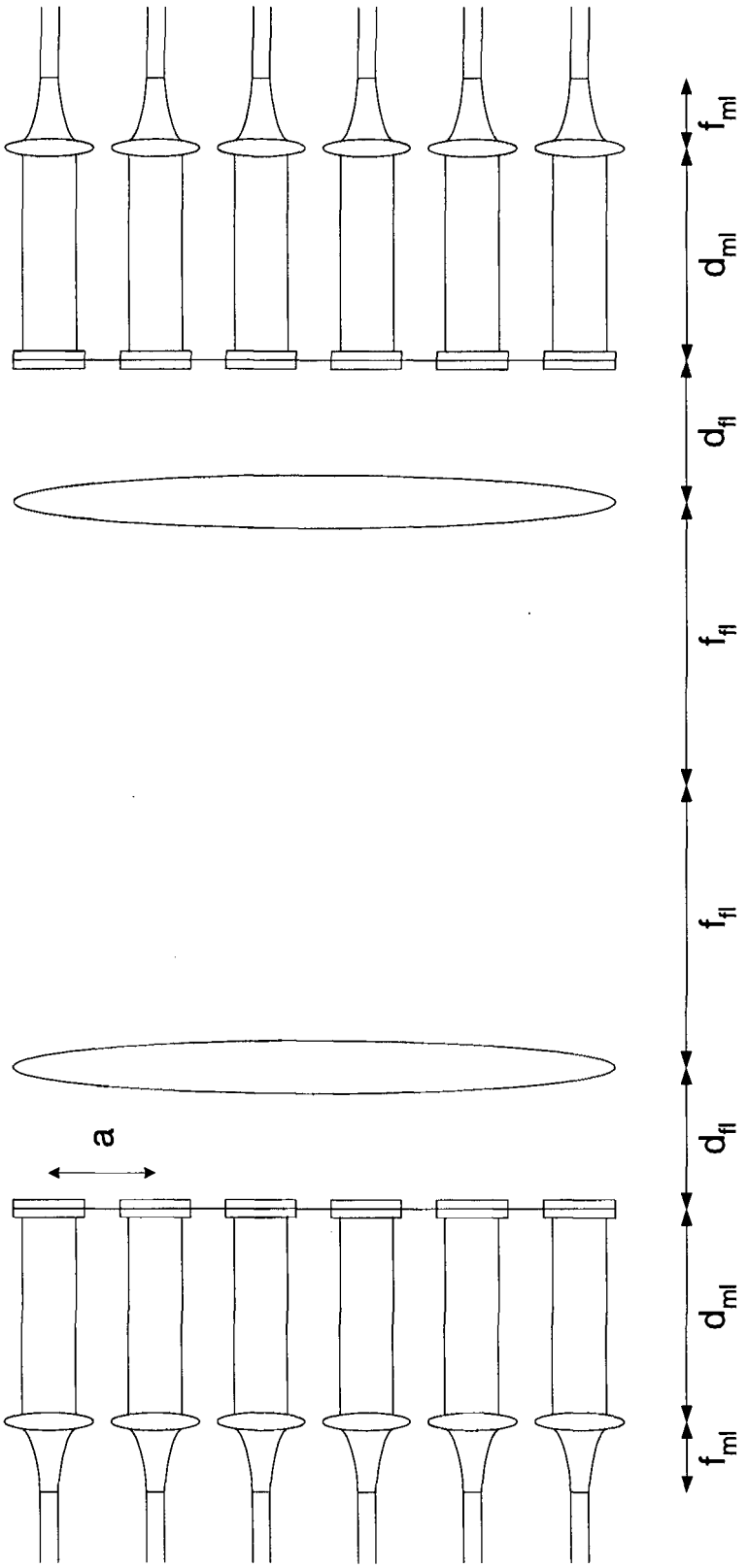

Figure 4.7: Optical system utilizing two OVPs, showing distances between elements

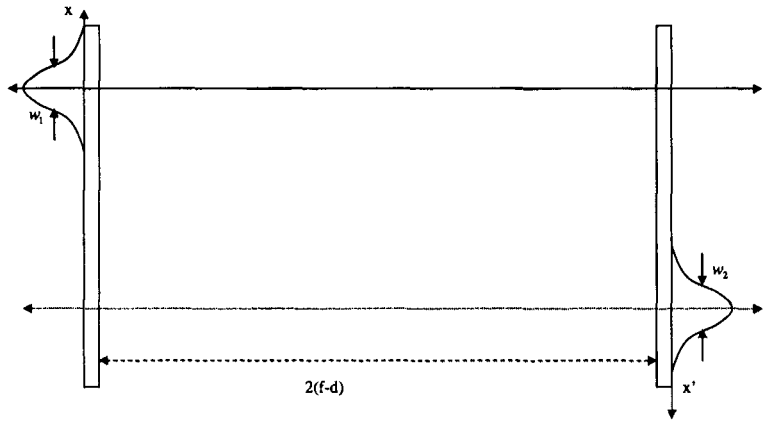

Figure 4.8: Simplified diagram describing beam steering between two SLMs

$$\begin{aligned} U_{2-} &= R\left[d'\right]\left\{G_1 H_1\right\} \\ &= Q\left[\tfrac{1}{d'}\right]\nu\left[\tfrac{1}{\lambda d'}\right]\Im Q\left[\tfrac{1}{d'}\right]\left\{G_1 H_1\right\} \\ &= Q\left[\tfrac{1}{d'}\right]\nu\left[\tfrac{1}{\lambda d'}\right]\left\{\Im\left\{Q\left[\tfrac{1}{d'}\right]G_1\right\}\otimes\Im\left\{H_1\right\}\right\} \end{aligned} \tag{4.57}$$

Since the hologram function H_1 routes the signal to a single port, the Opto-VLSI encoding can have to be in the form of a stepped blaze grating [94]. The form of the Fourier transform of a stepped grating is, as can be deduced from the results of Appendix A:

$$\Im\left\{H_1\right\} = \sum_{n=-\infty}^{\infty} \varepsilon_n \exp\left(j\phi_n\right)\partial\left(x - x_n\right) \tag{4.58}$$

If we assume that the separation between various orders of the hologram replay pattern is larger than the diameter of the Gaussian beam with non-negligible field [5], i.e. $(x_n - x_{n-1}) > 3.06 w_1$, we can write:

$$U_{2-} = Q\left[\frac{1}{d'}\right]\nu\left[\frac{1}{\lambda d'}\right]\left\{\Im Q\left[\frac{1}{d'}\right]\left\{G_1\left(x'\right)\right\}\right\} \tag{4.59}$$

Noting that the operators will not make a distinction between x and x' (due to linearity of the system), we arrive at the conclusion that

$$U_{2-_n} = \varepsilon_n \exp\left(j\phi_n\right) Q\left[\frac{1}{d'}\right]\nu\left[\frac{1}{\lambda d'}\right]\Im Q\left[\frac{1}{d'}\right]\left\{G_1\left(x'\right)\right\} = R\left[d'\right]\left\{G_1\left(x'\right)\right\} \tag{4.60}$$

This implies that the Gaussian beam will progress, in the direction of each of the diffracted orders, following its natural divergence. Since the beam steering requirement

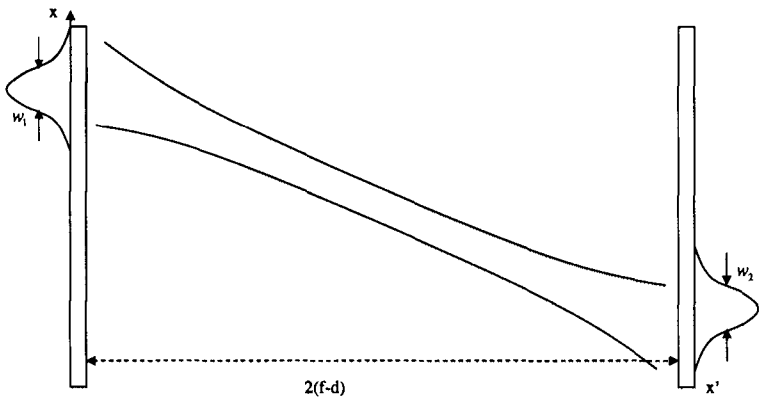

Figure 4.9: Showing the desired Gaussian beam arrangement

is to reproduce at the second hologram a Gaussian beam as close to the input beam as possible, phase curvature at the first hologram should be chosen in such a way that the waist of the beam should be at the middle between the two processors, as shown in Fig. 4.9.

Since the waist can be at the center of the system only for one set of inputs and outputs, an intermediate value can be chosen for such architecture.

4.4.2 Coupling from Undesired Diffraction Orders

We have analyzed so far the propagation of the desired beam. However, other (undesired) beams are also diffracted. We are interested to know the maximum cross-talk we can expect from these beams. Therefore, we calculate the maximum cross-talk in the various diffracted orders, assuming that these beams themselves travel undisturbed. Since we are interested in the maximum cross-talk, we will assume that the unintended beam travels undisturbed to the collimator, although the actual cross-talk of the real beam will be less.

One question we need to test is the difference between the two-hologram beam steering system and the single hologram beam steering system, as far as the cross-talk isolation provided. These two architectures are represented schematically in Figs. 4.10 and 4.11.

For a system containing one steering stage, the output ports need to be brought very close together, in order to minimize the variation in coupling efficiency (due to the variation in fiber launch angle). The system with one stage is shown in Fig. 4.10. The crosstalk from the unintended beam will be simply an unintended beam that is coupled normally onto a port. Therefore, the crosstalk is totally dependent on the ability of the hologram to reduce the power of the unintended beam to low levels.

In a two hologram system, since the second set of holograms will be the complex

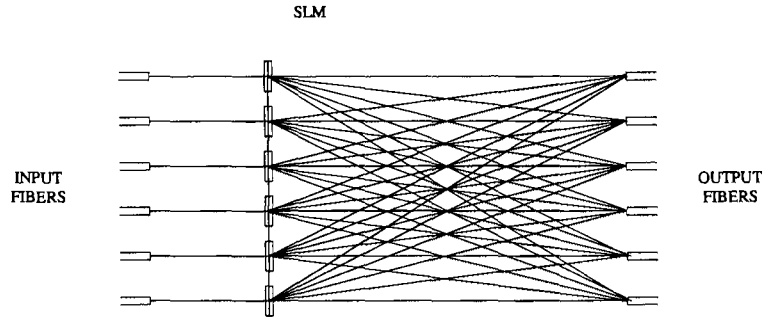

Figure 4.10: A system consisting of one steering stage

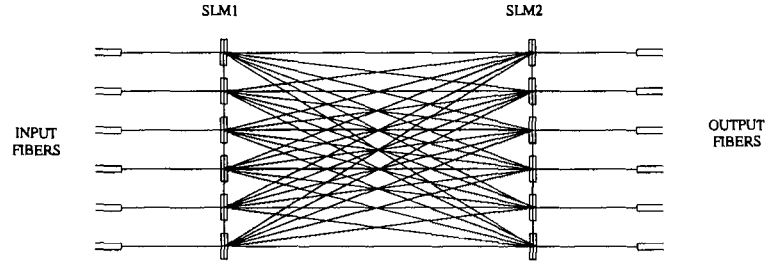

Figure 4.11: A system consisting of two steering stages

conjugate of the first set of holograms, resulting in beams that are launched normal to the output fibers. In such a setup, the very sensitivity of the output fibers to launch angle, allows for a greatly enhanced cross-talk isolation.

One approach two effectively evaluating the inter-channel cross-talk may be to compare the optical power in output port (P_{out}) against the worst-case scenario of power coupled unintentionally into another output port (P_{wc}). We denote the cross-talk isolation as C_i in dB:

$$C_i = 10 \log \left(\frac{P_{out}}{P_{wc}} \right) \tag{4.61}$$

We first decouple the two transverse dimensions, since the circular symmetry of the fiber implies that the crosstalk figure for a one dimensional beam steering is always worse than the two dimensional case. The entire system is shown in Fig. 4.12. The physical distance between the two steering stages is $2(f_{fl} + d_{fl})$ while the equivalent optical path length is $2(f_{fl} - d_{fl})$, with a total inversion of the array. Therefore, for holograms $h_1, h_2, \cdots, h_6$ at the first stage, the possible deflection angles (in gradient) would be:

$$\theta_{mn} = \frac{a(m-n)}{2(f_{fl} - d_{fl})} \tag{4.62}$$

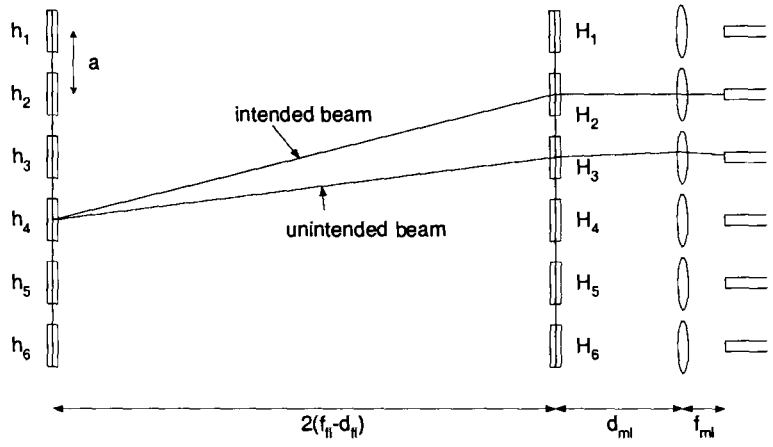

Figure 4.12: Beam coupled into unintended hologram and corresponding fiber

where m is the input port number (1 to 6), n is the output port number (1 to 6). From this relation, the possible values of θ_{mn} are:

$$-\frac{5a}{2(f_{fl}-d_{fl})}, -\frac{2a}{f_{fl}-d_{fl}}, -\frac{3a}{2(f_{fl}-d_{fl})}, -\frac{a}{f_{fl}-d_{fl}}, -\frac{a}{2(f_{fl}-d_{fl})}, 0,$$
$$\frac{a}{2(f_{fl}-d_{fl})}, \frac{a}{f_{fl}-d_{fl}}, \frac{3a}{2(f_{fl}-d_{fl})}, \frac{2a}{f_{fl}-d_{fl}}, \frac{5a}{2(f_{fl}-d_{fl})} \quad (4.63)$$

The deflection angles at the second stage will be the negative of the values for the first stage (in effect, the same list as above). The scenario for worst case of cross-talk will occur when the optical signal arrives at an unintended hologram at the first stage and gets coupled into the port corresponding to that hologram (Fig. 4.12).

In this scenario, a beam (m,n), from port m to port n, through holograms H_m (at the first steering stage) and H_n (at the second steering stage), also diffracts light to neighboring holograms $H_{n\pm1}$. A direct coupling into fibers $n\pm1$ will never take place. This is because, if H_n steers the beam by θmn, then $H_{n\pm1}$ cannot have the value of $m(n\pm1)$, since it would be steering a beam from a port other than m. Therefore, the worst case will correspond to a combination of beam steering by the first and second steering stages with the smallest value of angular difference, i.e:

$$\theta_e = \theta_{mn} - \theta_{m(n\pm1)} = \pm\frac{a}{2(f_{fl}-d_{fl})} \quad (4.64)$$

The system from the second stage to the fiber at the unintended port may be represented as shown in Fig. 4.13.

The lateral offset x and launch angle of the unintended beam may be shown to be:

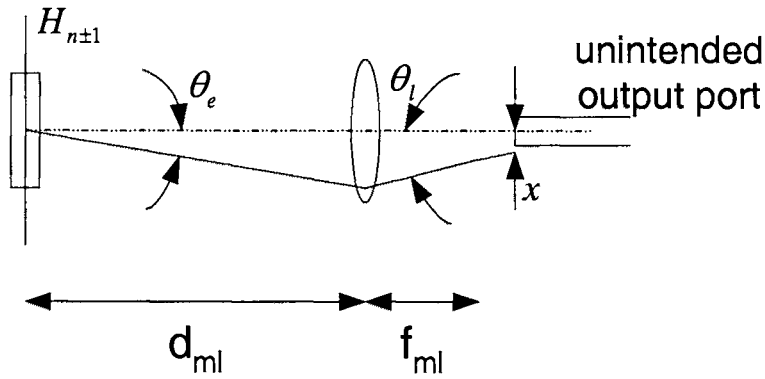

Figure 4.13: Lateral offset and launch angle for unintended beam

$$x = f_{ml}\theta_e = \frac{af_{ml}}{2(f_{fl} - d_{fl})} \tag{4.65}$$

and

$$\theta_l = \theta_e\left(1 - \frac{d_{ml}}{f_{ml}}\right) = \left(\frac{a}{2(f_{fl} - d_{fl})}\right)\left(1 - \frac{d_{ml}}{f_{ml}}\right) \tag{4.66}$$

The decrease in coupling efficiency due to the lateral offset x and the launch angle θ_l may be deduced from the splicing analysis of Marcuse [92], as mentioned in Section 4.2.1:

$$\eta_x = \exp\left[-\frac{x^2}{w^2}\right] = \exp\left[-\frac{a^2 f_{ml}^2}{4w^2\left(f_{fl} - d_{fl}\right)^2}\right] \tag{4.67}$$

and

$$\eta_{\theta_l} = \exp\left[-\frac{(\pi n_2 \theta_l)^2}{\lambda^2}\right] = \exp\left[-\frac{\pi^2 n_2^2 a^2}{4\lambda^2\left(f_{fl} - d_{fl}\right)^2}\left(1 - \frac{d_{ml}}{f_{ml}}\right)^2\right] \tag{4.68}$$

where again $w \cong r\left(0.65 + \frac{1.619}{V^{3/2}} + \frac{2.879}{V^6}\right)$, n_2 is the index of the fiber cladding, λ is the optical wavelength, r is the fiber core radius and V is the normalized fiber frequency ("V-number"). The total cross-talk isolation (in dB) can then be calculated from the following relation:

$$C_i = 10\log\left(\eta_x \eta_{\theta_l}\right) \tag{4.69}$$

Using Eq. (4.69), we can compare the difference in crosstalk isolation for systems utilizing one and two stage steering. Since, as we have said earlier, the one stage system offers no isolation to an unintended beam that is incident normally on the output fiber, the C_i in Eq. (4.69) actually describes the crosstalk isolation improvement in a two stages steering

system. Therefore, a two stage system *always* has greater crosstalk isolation over a single stage system, and the improvement is quantified through evaluation of C_i .

In conclusion, the multifunction processor "steers" a beam twice, first by the OVP and secondly by the grating, before it is coupled into the output collimator. Therefore, an unintended diffracted beam by the first stage (OVP), does not directly couple into the collimator, but is offset and tilted by the grating, thereby giving an added crosstalk isolation (given by Eq. (4.69)) over that offered by the hologram pattern.

4.5 Conclusions

In this chapter, we have studied the theoretical basis of the propagation of the diffracted beams, and used the relations developed to study two systemic causes of insertion loss in the multifunction device: namely, the offset at the collimator "A" from beams between λ_1 and λ_N sent from collimator "B", as well as the effect of the number of pixels in the hologram on the collimator coupling efficiency. We conclude that the coupling loss from the offset can be effectively minimized by judiciously choosing smaller angles between the two collimators (Θ_{AB}). Likewise, when the number of pixels in a hologram is above ≈ 20, there is no further advantage in increasing the number of pixels.

Next, the filter response of the multifunction device was analyzed, and two parameters that affect the filter bandwidth were identified; namely, the width of the Gaussian beam and the distance D_A between the collimator(s) and the grating.

Finally, the effect of the two stage steering nature of the multifunction processor was compared to a typical one stage system, and its superior cross-talk isolation performance was demonstrated. However, it is important to note the actual cross-talk isolation of a device is dependent on the crosstalk isolation that the holographic pattern on the OVP. Section 4.4 showed that in addition to the crosstalk isolation of the hologram pattern, the system structure provides additional crosstalk isolation. In the next chapter, we will study generation of the holograms that allow for beam steering and will identify the algorithms for computer generated holograms and their relative performance in reducing crosstalk.

Chapter 5

Computer Generated Hologram for Opto-VLSI WDM Components

OVPs offer promising technological platform for implementing reconfigurable Wavelength Division Multiplexing (WDM) networks. By driving an OVP with a computer generated hologram (CGH), dynamic optical beam steering and/or multicasting can be achieved. In this chapter we develop and compare CGH algorithms based on simulated annealing and projection methods, for optimum beam steering and multicasting applications. Experimental results show that simulated annealing can generate accurate output targets with low crosstalk but requires a long computation time for large-scale multicasting. The projection method is more computationally efficient in generating multicasting holograms, however, it is susceptible to higher crosstalk.

5.1 Introduction

Opto-VLSI technology for optical signal devices for WDM network components has received considerable attention [53,95]. In particular, diffractive, non-mechanical optical processing for optical filters, gain equalizers, and add-drop multiplexers have been demonstrated [53, 95–98]. All such systems rely on an OVP to control spatially the optical phase retardation of the beam, thus providing a reconfigurable beam steering and/or multicasting capabilities. For efficient beam processing, fast algorithms for hologram generation are required, which provide variable diffraction efficiency and low crosstalk. These requirements have received sustained attention [99]. Generally, the problem of generating CGHs is to calculate the

phase distribution, $h(x, y)$, in the hologram plane, for a target diffracted intensity pattern $T(u, v)$, given by

$$T(u, v) = \int\int_{\Theta_h} h(x, y) e^{2\pi j(ux+vy)} dxdy \tag{5.1}$$

where Θ_h is the aperture of the hologram and $h(x, y)$ is pixellated with finite phase levels, and unity amplitude.

Several methods have been identified for use in the generation of holograms, including projection onto convex sets [100, 101], Gerchberg-Saxton and Gerchberg-Papoulis algorithms [102–105], generalized projection algorithms [106–112], parallel projection algorithms [113], iterative fourier transforms [114], phase encoding [115], simulated annealing [116], and genetic algorithms [117]. In this chapter, we study the feasibility of two algorithms, namely the generalized projections and simulated annealing algorithms, for the generation of holograms that realize single- and multiple-spot diffracted intensity pattern targets. Further, we demonstrate a computer-controlled testing and measurement setup for OVP programming and output beam monitoring.

Results show that accurate output targets with low cross-talk can be generated using the simulated annealing method, whereas for a diffracted intensity pattern target the projection method results in high crosstalk levels. However, the projection method is found to be relatively more computationally efficient than the simulated annealing method, especially for a multicasting diffraction target of large spot number.

5.2 Estimation of Maximum Diffraction efficiency

Using the methods of scalar diffraction described in Chapter 4, we consider the diffraction efficiency expected from a beam steering hologram. First we give a brief intuitive introduction to the notion of beam steering and then discuss two estimates for theoretical maximum efficiency.

5.2.1 Beam Steering

The ideal hologram profile for beam steering applications can be found by analyzing the simple wave propagation equation:

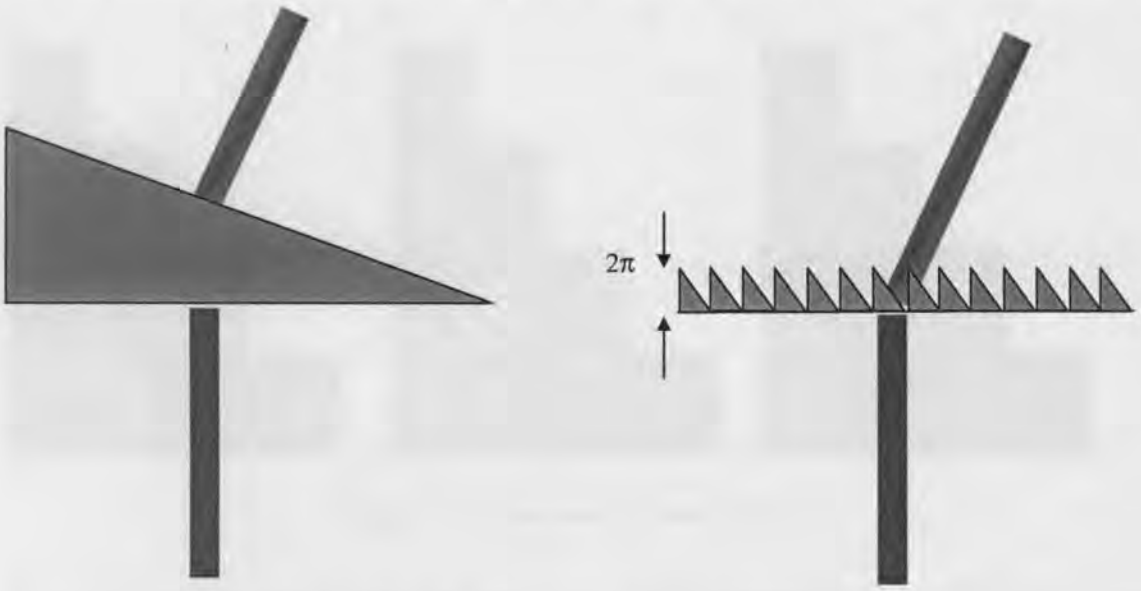

Figure 5.1: Similarity between prism and blazed grating

$$U = e^{j(\vec{k}\cdot\vec{r}-\omega t)} \tag{5.2}$$

The direction of the beam is determined by $\vec{k}$, the propagation constant, and $\vec{r}$ is the position vector. If the wavefront encounters a phase retardation linearly varying across a plane, $e^{(j\vec{a}\cdot\vec{r})}$, the new wavefront will be of the form $e^{j(\vec{k}'\cdot\vec{r}-\omega t)}$, travelling in the direction $\vec{k}' = \vec{k} + \vec{a}$. Therefore, the beam direction can be changed without distorting the beam itself, if a hologram provides a linearly varying phase term. Next, if we "wrap" the phase back to zero whenever it reaches 2π (without any change to the system - since phase of 0 and 2π are equivalent), we would get a linearly varying phase from 0 to 2π, i.e. a blazed grating. Figure 5.1 shows the relationship between a prism (linearly varying phase function) and a blazed grating.

However, the OVP is unable to reproduce the prism or the blazed grating. This is because the phase encoding in OVPs is quantized in the number of phase levels as well as pixellated. Therefore, an approximation to the blazed grating is made in the OVP, as shown in Fig. 5.2. This approximation was first proposed by Dammann [94], and such gratings are generally known as "Dammann blaze gratings".

Beside modeling the optical switch as shown in Fig. 5.2, an important theoretical limitation of the hologram will be its diffraction efficiency. The calculation of efficiency for a Dammann grating has been included in Appendix A. If we disregard the specific

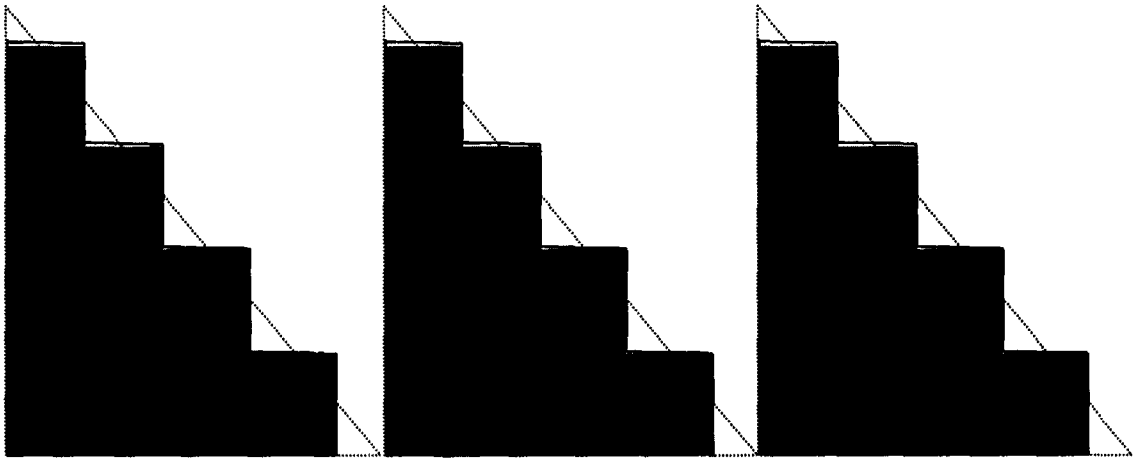

Figure 5.2: Dammann Blaze grating

arrangement of the spatial light modulator, there still is a theoretical limit of the diffraction efficiency possible [118], simply based on the fourier transform of the desired signal shape, $f(x)$:

$$\eta = \frac{\left|\int F(u)du\right|^2}{\int |F(u)|^2 du} \tag{5.3}$$

The derivation of the above relation is described in Appendix B. For the case of a delta function $f(x) = \delta(x - x_o)$, the Fourier transform will be such that $F(u) = \exp(j2\pi u x_o)$. This will result in $\eta = 100\%$. However, for any other function (i.e. $|F(u)| < 1$ for some values of u), it is impossible for a diffractive phase element to give a 100% (theoretical) efficiency.

5.3 Generation of CGHs

CGHs may essentially be divided into two broad categories: those that iteratively project onto constrained sets in order to converge onto a realizable solution, and those changing a single pixel or a group of pixels of an existing candidate solution to get closer to the target. In this section, we will consider one algorithm from each class, namely the generalized projection onto constrained sets and simulated annealing.

5.3.1 CGH by Simulated Annealing

The simulated annealing algorithm for hologram generation first defines a cost function as a measure of the distance between the diffracted field pattern of the target T and the

field pattern of the current candidate hologram. The target generally does not define the entire diffraction field, but rather a small subset of the diffracted field which is of interest. The algorithm, as formulated by Dames, et. al ([116]) starts from an initial random hologram pattern, $h(x, y)$ and computes the resulting diffraction field. Since the angular components of a wavefront are described by its fourier transform, the diffracted beam can be represented by a fourier transform [91]. For a pixellated hologram, $h(m, n)$, which represents the complex transmittance of each pixel (m, n), the diffracted beam $H(k, l)$ is described by:

$$H(k, l) \equiv DFT(h(m, n)) \tag{5.4}$$

where (k, l) represents the coordinates in the output plane. Since the target intensity $T(k, l)$ is only defined at a few spots in the diffraction field, we then reduce the set $H(k, l)$ to a smaller set H_T containing only the coordinates where the target spots are defined. From this, we compute the cost function, which is a measure of the discrepancy between the target and the diffraction field of the hologram. One expression for the cost C is:

$$C = \sum \left(T(k, l) - |H_T(k, l)|^2\right)^2 \tag{5.5}$$

Next, a pixel or group of pixels are randomly changed (subject to the constraint on the phase levels). Then the cost function is calculated again. However, the entire diffraction field $H(k, l)$ need not be recalculated, since it will be possible to compute ΔH_T arising from the change in a single pixel $\Delta h_{m,n}$:

$$\Delta H_T = \Delta h_{m,n} e^{-2pij(km+ln)/N} \tag{5.6}$$

This results in a change in cost, which similarly can be computed by Eq. (5.5). If the cost decreases (that is ΔC is negative), the pixel change(s) are accepted. If the cost increases, the pixels are accepted with a probability of $e^{\Delta C/T}$, where T is the "'temperature"', which is gradually reduced as the number of iterations increases. The decrease in temperature can be expressed as:

$$T = T_o e^{-T_e i/I} \tag{5.7}$$

where T_o and T_e are parameters that determine the starting value and rate of decrease of the temperature, i is the current iteration number, and I is the total number of desired

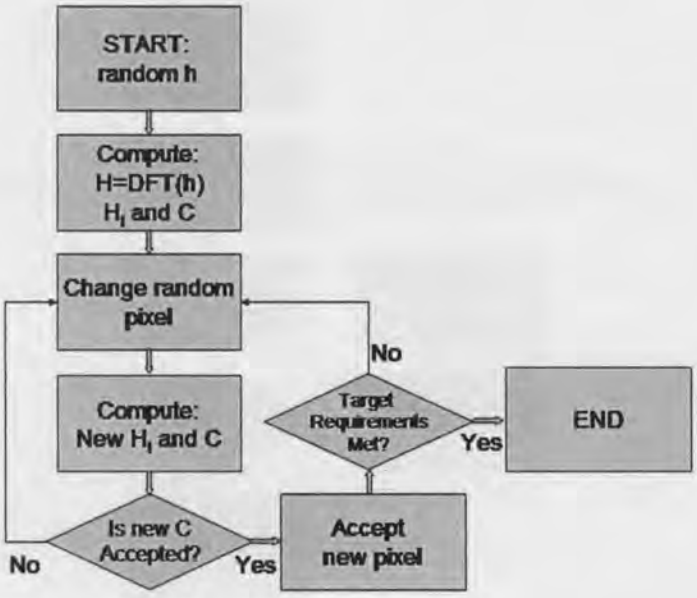

Figure 5.3: Flow Chart of Simulated Annealing Algorithm.

iterations. The end of the algorithm can be set at a certain number of iterations, or when the cost has been reduced to a determined level, or alternatively, when the temperature has been reduced to a certain value. Figure 5.3 shows the flow chart for the simulated annealing algorithm.

5.3.2 Projection onto Constrained sets

Following the procedure outlined by Stark, et. al [107], a hologram can be designed by iteratively projecting onto two constrained sets. The initial hologram $h_o(x, y)$ is optimized by interactively projecting onto two sets C_{QP} and C_{CP}, which represent the phase quantization constraint on the hologram, and a constraint to set the target magnitude, respectively. Each consecutive hologram is obtained by serially projecting onto the sets as follows.

$$h_{n+1} = P_{CP} P_{QP} h_n \tag{5.8}$$

where P_{CP} and P_{QP} are the operators that project onto C_{CP} and C_{QP}, respectively. Usually, these two sets are defined as [107]:

$$C_{CP} \equiv \{h(x, y) \leftrightarrow H(u, v) : |H(u, v)| = T(u, v)\} \tag{5.9}$$

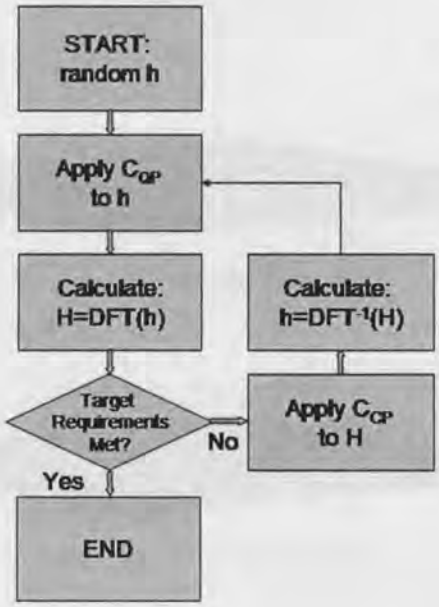

Figure 5.4: Flow Chart of Generalized Projections Algorithm.

and

$$C_{QP} \equiv \left\{ h(x,y) : h(x,y) = \frac{2\pi k}{Q} \right\} \tag{5.10}$$

where Q is the number of phase levels, $k \in \{0, 1, ..Q-1\}$ is an integer defined by the following relation:

$$\left| \frac{2\pi k}{Q} - \arg(h) \right| = min \left| \frac{2\pi n}{Q} - \arg(h) \right| \forall n \in \{0, 1, ...Q-1\} \tag{5.11}$$

Since the two constrained sets C_{CP} and C_{QP} are not convex, the convergence of the projections is not automatically assured. However, if there are only two projections per iteration (as is the case here), then it can be shown that the iterations will converge [106]. A flow chart depicting the generalized projection algorithm is shown in Fig. 5.4.

5.4 Computer Simulations

The two CGH algorithms described in the previous section were utilized in producing single peaks as well as multiple peaks in the diffraction field. The following parameters were used:

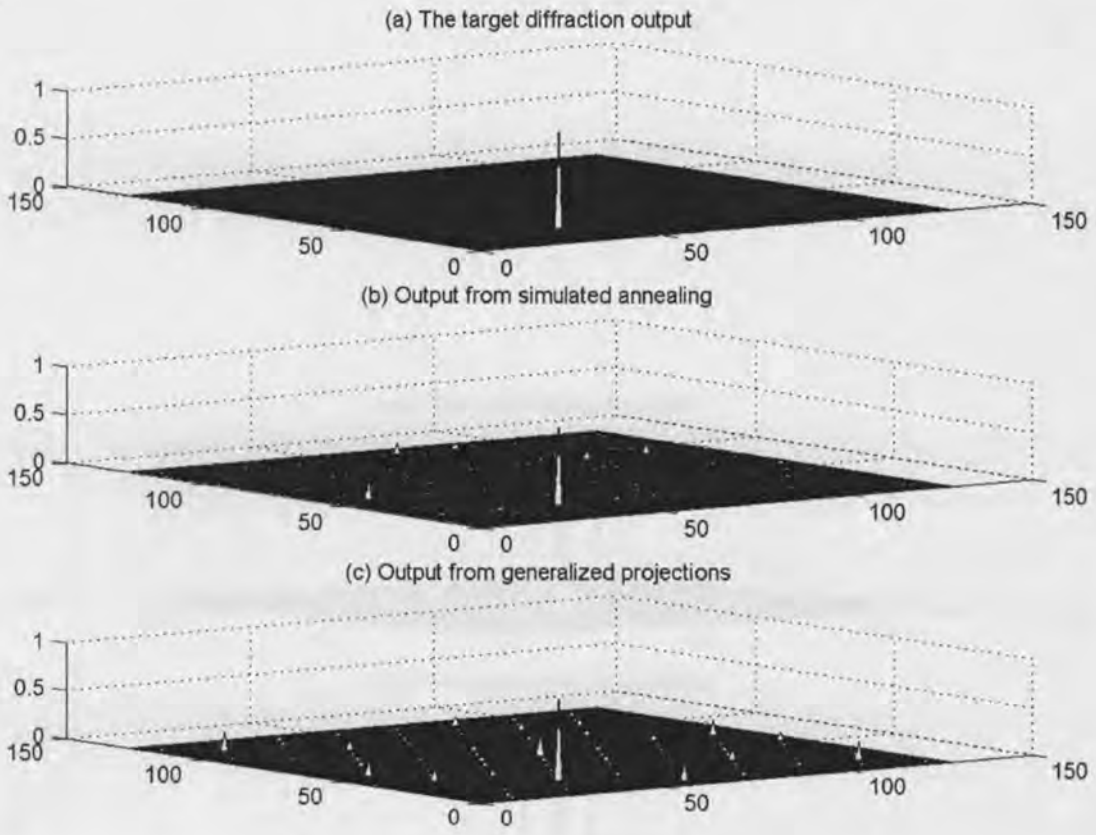

Figure 5.5: Simulation results for a target of a single peak.

1. Hologram h, with 128×128 pixels, each of which can have 4 equally spaced phases $(0, \pi/2, \pi, 3\pi/2)$ for both algorithms.

2. Number of iterations $I_{SA} = 10N^2 \log_2 N^2 = 2,293,760$ for the simulated annealing algorithm, and $I_{GP} = 10$ for the generalized projection algorithm.

Figures 5.5 and 5.6 typical simulation results, showing the desired target and the results for the two algorithms under consideration.

5.4.1 Effect of the number of peaks

One interesting comparison of the generalized projection algorithm and the simulated annealing algorithm is their effectiveness as the number of desired target peaks increases. The simulation was carried out for the simple case of a plane wave incident on a phase hologram. The effectiveness of the hologram can be measured by the diffraction efficiency η, which can be defined as:

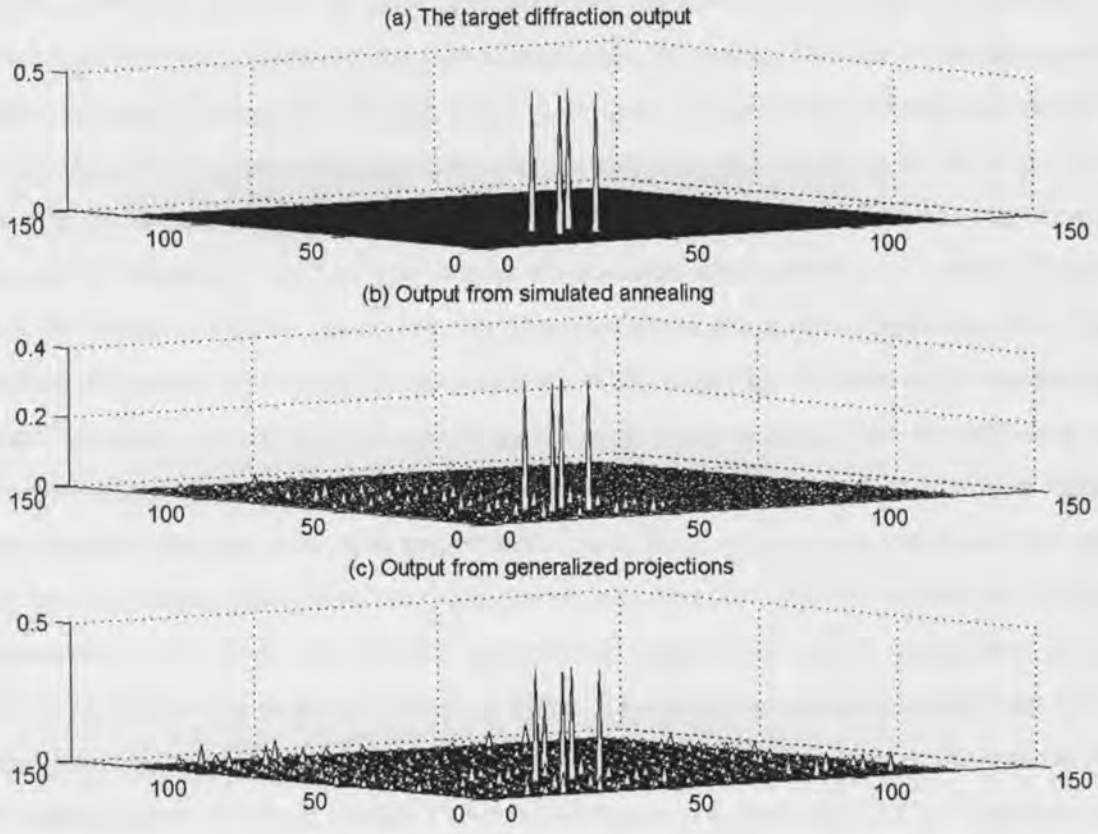

Figure 5.6: Simulation results for a 4-peak target.

$$\eta = \frac{\left|\int H_T(u,v)dudv\right|^2}{\left|\int H(u,v)dudv\right|^2} \tag{5.12}$$

Figure 5.7 shows the efficiency of the two algorithms as a function of the number of computational operations. For the purposes of the simulation, we define the evaluation of the field resulting from a single pixel on a single output position as a "'unit"' operation. Therefore, Eq. (5.6) is considered one operation.

The results of Fig. 5.7 indicate that for a small number of target peaks (<8), the simulated annealing algorithm is more efficient, while the generalized projection algorithm's relative performance improves with increasing number of peaks. This can be readily appreciated from considering the differing target definitions in these two particular algorithms. While the simulated annealing algorithm defines only the peak positions in the target vector $T(m,n)$ corresponding to $H_T(m,n)$, the projection algorithm defines the target over the entire diffraction field (setting to zero all positions where there is no peak). Therefore, the number of peaks has no effect on the generalized projections algorithm, while the number of operations required for simulated annealing algorithm increase as the number of peaks increases. Assuming both algorithms converge monotonously, then the efficiency of the generalized projections algorithm should relatively improve, as indeed is seen in simulation results. At this point, it is important to note the computational difference between the two algorithms. Each iteration of the projection operation requires two discrete fourier transforms, which, if we use the FFT optimization, requires $2N\log_2 N$ operations, where $N \times N$ is the number of pixels of the hologram. The simulated annealing algorithm however, performs only 1 such operation, since each iteration simply changes the weights to the target position through changing the transmittance of a pixel (Eq. (5.6)). Therefore, in terms of the computational length, the number of iterations in the generalized projection algorithm, I_{GP}, and the simulated annealing algorithm, I_{SA} are related as follows:

$$\frac{I_{SA}}{N_{peaks}} = \frac{I_{GP}}{2N\log_2 N} \tag{5.13}$$

where N_{peaks} is the number of peaks in the target. This relation, of course, does not give us the real speed of the algorithm as simulated in the computer: the highly optimized linear programming libraries, such as as LAPACK make the prediction of the actual computational speed based on the number of operations performed nearly impossible. In fact, we find that for the same number of operations, the generalized projections algorithm executes

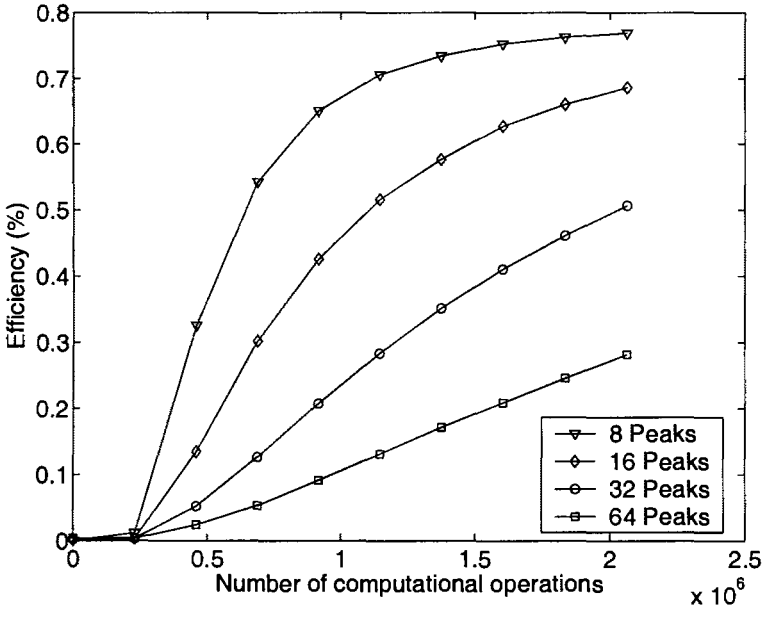

(a) Using simulated annealing algorithm.

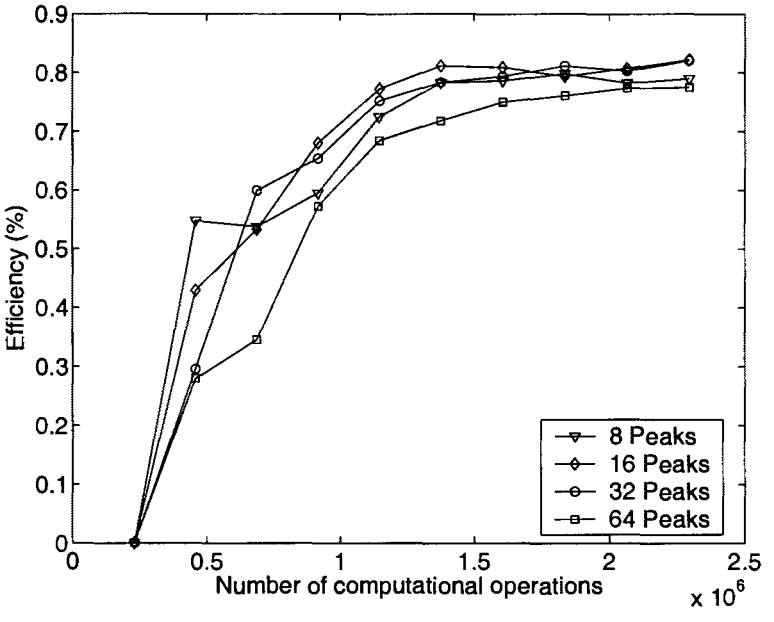

(b) Using generalized projections algorithm.

Figure 5.7: Efficiency as a function of the number of computational operations for various number of desired target peaks.

significantly faster. Therefore, the number of computational operations useful simply in providing a figure of merit for comparing the relative efficiency of the two algorithms.

5.5 Experimental Results

An experimental system was devised using a computer controlled testing of the diffraction from a spatial light modulator (SLM). The system is shown in Fig. 5.8. A computer was used to control the holographic pattern displayed on a 128 × 128 pixel nematic Liquid Crystal SLM, manufactured by Boulder Non-Linear Inc. The computer was also used to control a 1550 nm wavelength laser source, which was collimated using a fiber collimator. The resulting diffraction pattern was studied using an infrared camera, which was read into the computer via a video capture card. A computer program in the Python scripting language was written to act as a daemon to control th experiment. It contained modules that controlled the SLM, via a specialized card in the computer's PCI bus, as well as provide a communication path to a GPIB bus, which allowed the computer control of the laser source as well as additional measurement devices, including an optical spectrum analyzer (OSA) and an optical power meter. The daemon itself is controlled through a TCP/IP link that allows the control and measurement of the experiment from any computer on the internet. A functional chart of the computer program is shown in Fig. 5.9.

Typical diffraction patterns captured by the video capture card are shown in Figs. 5.10 and 5.11. As can be seen from the figures, there is a significant peak at the center of the field, corresponding to the "'zeroth order"' or undiffracted beam. This arises from the fact that the SLM phase modulation is not exactly separated into the Q phases. To confirm this hypothesis, a hologram for a 4-peak target was altered so that the range of the phases was decreased from 2π (full-wave retardation) to 1.4π . The simulation of this altered hologram (Fig. 5.12) shows that phase errors at the pixel level result in a significant zeroth order beam arising.

5.6 Conclusions

In this chapter, we have shown a method for comparing diffraction efficiencies of hologram generating algorithms and an experimental setup used to measure the diffraction pattern arising from the holograms. Further, we analyzed the relative merits of the generalized

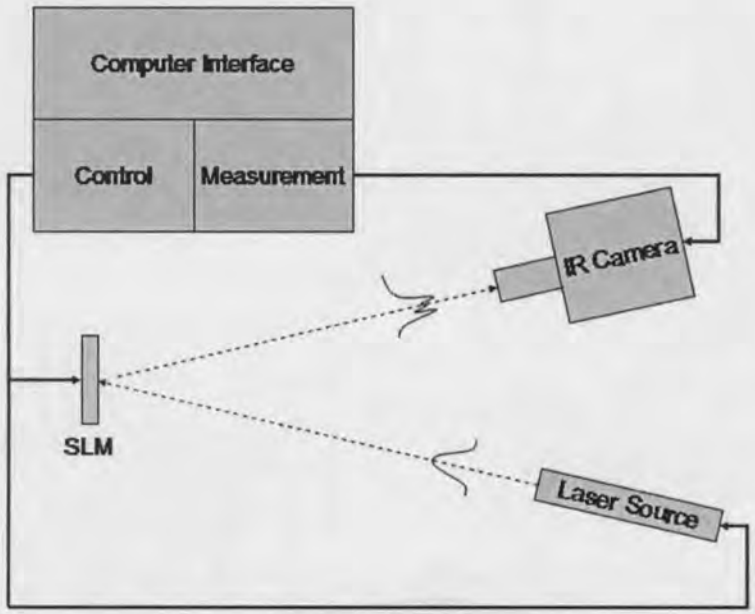

Figure 5.8: The experimental setup for measurement of optical diffraction.

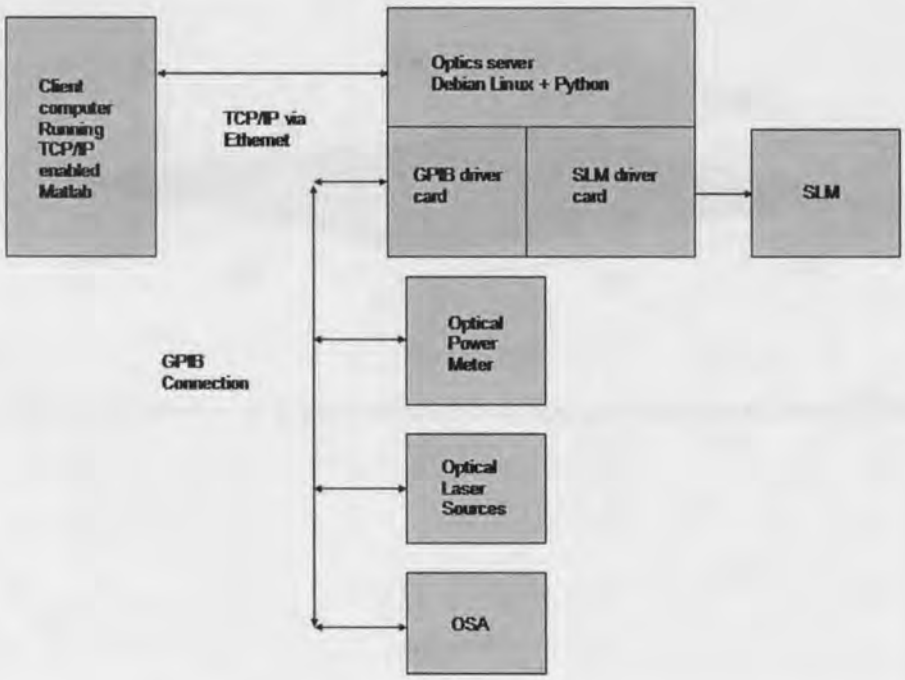

Figure 5.9: Functional relationships between computer interface modules and control modules.

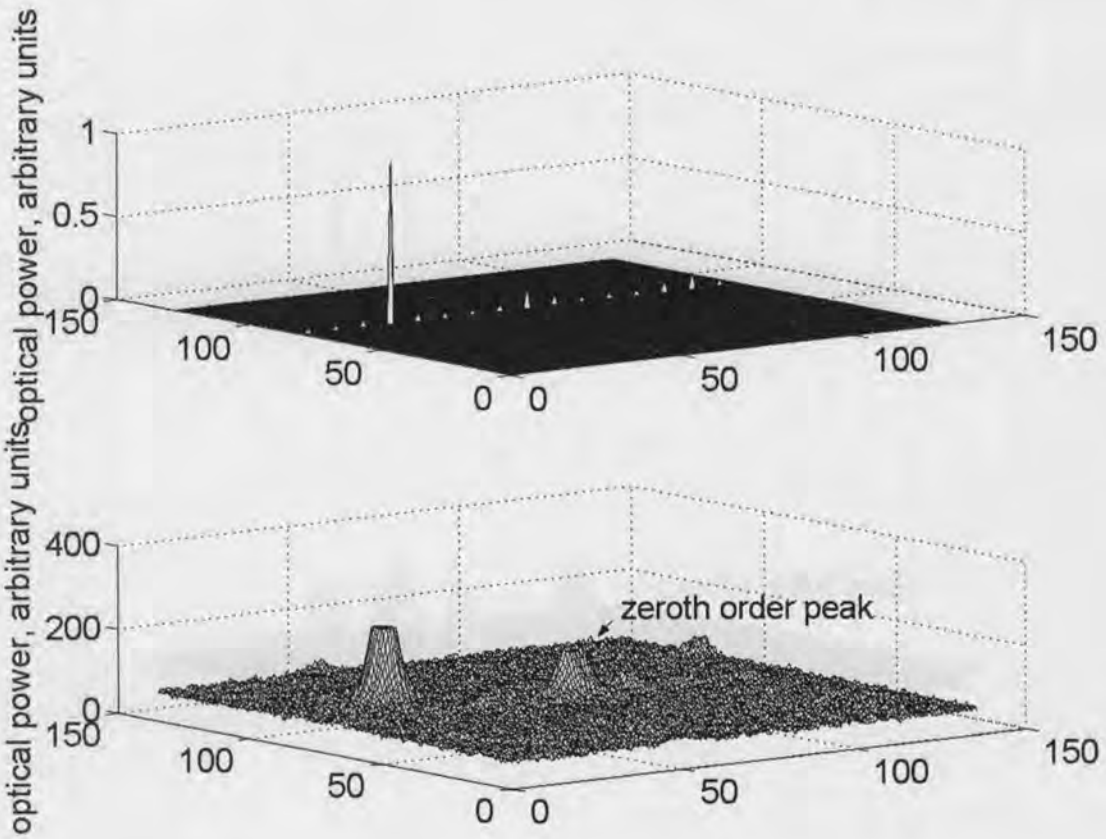

Figure 5.10: Simulated and experimental diffraction patterns for a single peak target.

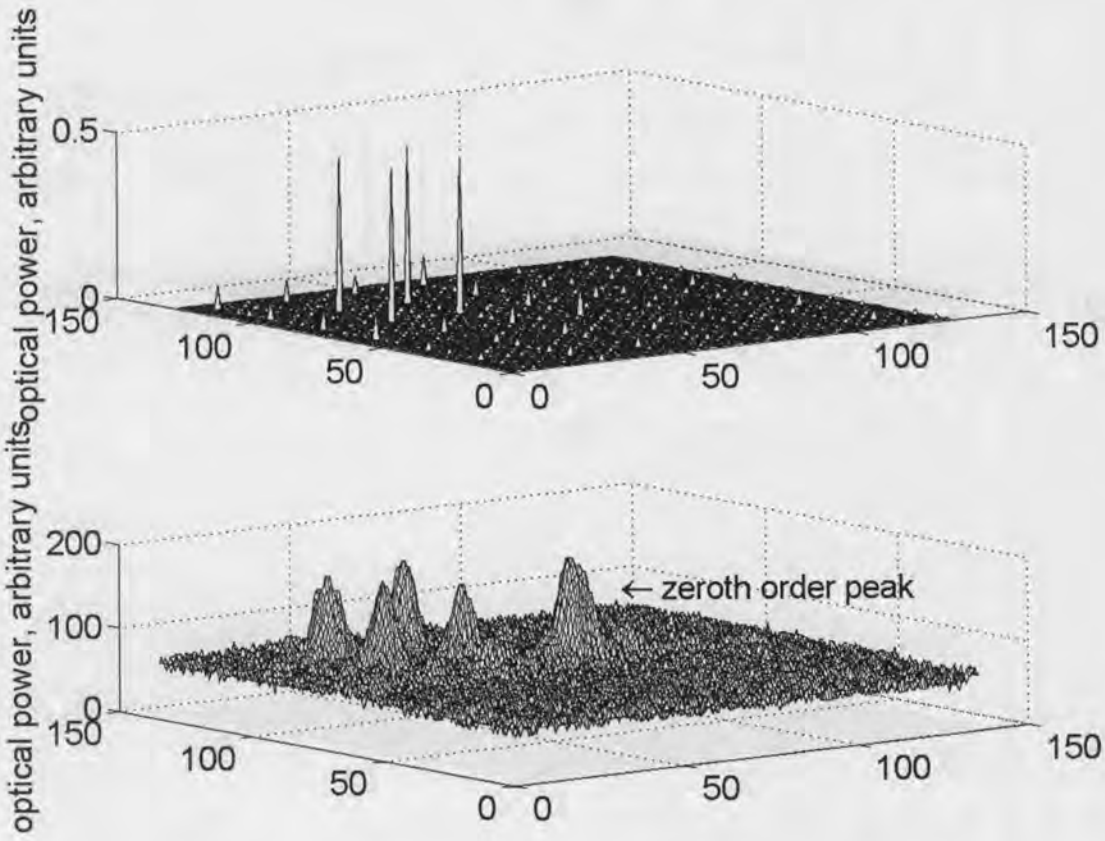

Figure 5.11: Simulated and experimental diffraction patterns for a 4-peak target.

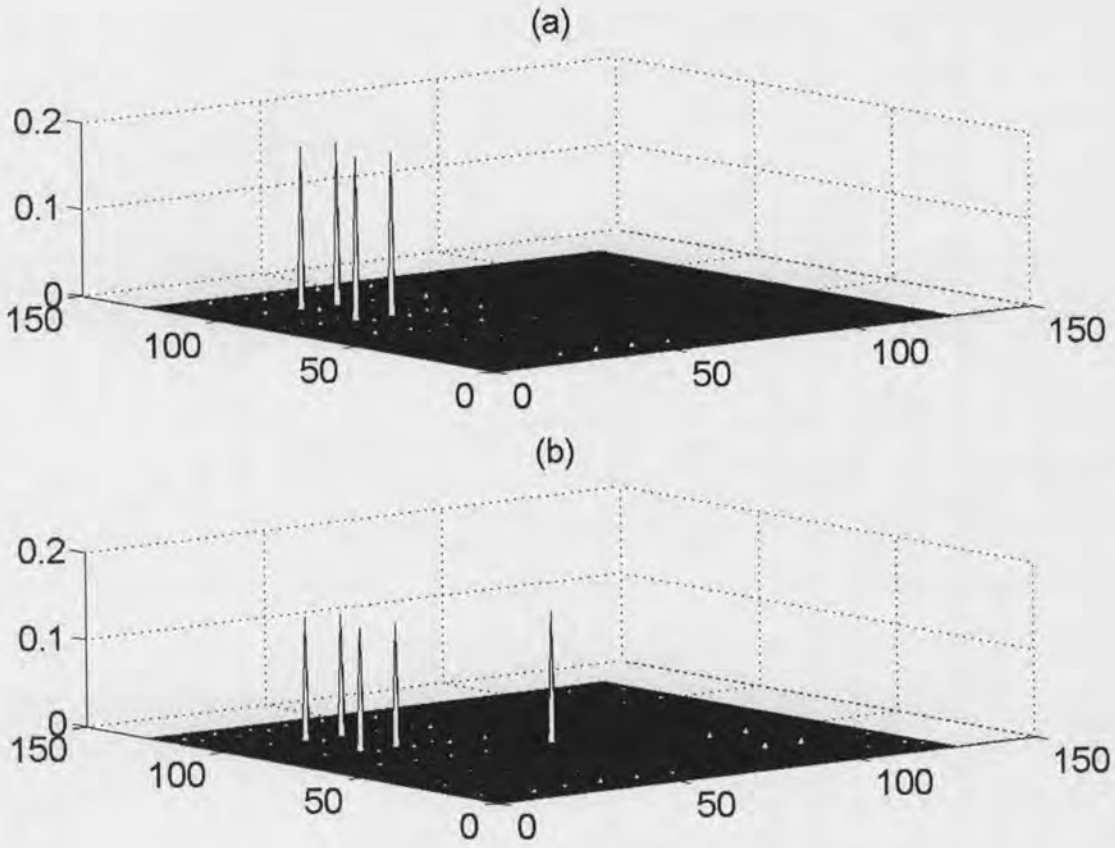

Figure 5.12: Simulation of pixel phase error: (a) diffraction with a 2π range of phases (b) diffraction with 1.4π phase range.

projection algorithm and the simulated annealing algorithm. We find that for a small number of peaks (<30), the simulated annealing approach is more efficient, while for a larger number of peaks, the generalized projection algorithm is more suitable.

Chapter 6

Experimental Demonstration of the Multifunction Device

In this chapter, we present the result of an experimental demonstration of the multifunction WDM device. We start by listing the equipment used in the experimental setup, and present a quick but accurate method for characterizing the phase retardation curve of the OVP. Then the layout of the multifunction processor is presented in two parts: First, the alignment of the OVP and grating with the first collimator ("A"), and second the alignment of the second collimator ("B") with the first collimator ("A"). Next, we analyze the insertion loss performance of the multifunction device. Finally, we present an experimental demonstration of a notch filter using the layout of the alternative WDM multifunction architecture. Throughout this chapter, we use the term collimator "A" to refer to the collimator that is oriented horizontally at the top of the layout, and collimator "B" is the second collimator placed below the first collimator, oriented at an angle to collimator "A", as shown in Fig. 4.4.

6.1 Equipment used

In addition to the basic experimental setup, consisting of an optical table, lenses, polarizers, prisms as well as optical stages, lens holders and fiber cords, the following specialized equipment will be in use for experimental verification.

OVP (Boulder Nonlinear Inc.): The central element of beam steering is the OVP, working as a phase hologram, with a layer of nematic liquid crystal providing the electrically

controlled phase retardation. There are 128×128 independently controllable pixels, with a pixel pitch of 40μm, and 60% fill factor (9μm dead space between pixels). In multiphase operation this device allows 128 phase retardation levels in the $0 - 2\pi$ range. The full specifications supplied by Boulder Nonlinear Inc. are given in the appendices.

Reflective Diffraction Grating: The diffraction grating used is a Zerodur substrate from Optometrics LLC, with 600 grooves/mm, which exhibits no difference in diffraction efficiency of the S and P polarized states at 1550 nm, and $< 4\%$ efficiency variation within the range 1525-1575 nm [119]. Therefore, it exhibits a low polarization dependence in the telecommunications wavelength range.

Optical Power meter (Anritsu MT9810A): This measures the total optical power arriving at its input port. The port connector is FC/PC fiber connector. Therefore, this allows the power coupled into an optical fiber. The device operates in the wavelength range 800-1600 nm.

Optical spectrum analyzer (Agilent 86142B): This instrument measures the spectral distribution of the optical field. It has a resolution of 0.05 nm and sensitivity down to -90 dBm. It has an optical range of 600-1700 nm.

Fiber collimators: A fiber collimator consists of a grin lens package at the end of a fiber that expands the optical beam propagating in a fiber and collimate it. There were two fiber collimators used, both with a beam waist of 1 mm.

Fiber Splicer: This instrument fuses two fiber cleaved ends in a manner that minimizes the optical power loss at the fusion spot, typically with a loss <0.1 dB.

Infrared Camera (Electrophysics 7290A): This instrument's detection layer is composed of a phosphor layer sensitive to light in the visible and near infrared bands. Its wavelength range is 400-1900 nm.

Laser Sources: There were four DFB laser sources used: three fixed at 1530 nm, 1550.12 nm and 1580 nm, respectively and one tunable laser with a range of 1524-1576 nm. All the lasers have an FC/APC fiber adapters for easy connection to the fiber collimators.

6.2 Characterizing the OVP

In this section we present a quick but accurate method for characterizing the OVP phase retardation. The OVP needs to be characterized since, in general, the VLSI layer of the OVP supplies voltages to the liquid crystal's electrodes in linearly distributed values between

zero and V_{cc}, which is the maximum voltage supplied. However, the phase retardation of the liquid crystal (LC) layer does not respond with a linearly varying phase retardation corresponding to the voltages applied. The response of the LC layer is dependent on the electrical characteristics as well as crystal orientation of the liquid crystal mixtures. This information, however, is usually unavailable, especially with commercially supplied OVPs. Therefore, we have developed a method for accurately mapping each voltage level to an optical retardation level.

First we note that the optical reflectance of the OVP in one dimension may be presented as:

$$\mathbf{p}(x) = \sum_{m=1}^{M} p\left(\frac{x - x_m}{a}\right) e^{j\phi_m} \tag{6.1}$$

where $p(x)$ is the square function as defined in Eq. (4.27), x_m is the position of the m^th pixel on the x-axis, M is the total number of pixels and ϕ_m is the phase retardation of the m_th pixel.

The Fourier transform of the reflectance function $\mathbf{p}(x)$ is:

$$\mathbf{P}(u) = a\text{sinc}au \sum_{m=1}^{M} e^{-2\pi j x_m u} e^{j\phi_m} \tag{6.2}$$

If there are N voltage levels in the OVP, we denote the voltages by $V_1, \ldots V_N$ and the corresponding N phase levels by $\phi_1, \ldots \phi_N$. Generally, the pixels are arranged regularly. Therefore, we can write, without loss of generality:

$$x_m = bm \tag{6.3}$$

where b is the pixel pitch.

In order to determine the i^{th} phase level, Ψ_i, corresponding to the voltage V_i, we create a pattern on the OVP that alternates between zero and Ψ_i (i.e. $\phi_1 = \Psi_i, \phi_2 = 0, \phi_3 = \Psi_i, \phi_4 = 0, \ldots$). We can then compute $\mathbf{P}(u)$ for this particular pattern as:

$$\mathbf{P}(u) = a\text{sinc}au \left\{ \sum_{m=1}^{M/2} e^{-2\pi j(2m-1)bu} e^{j\Psi_i} + \sum_{m=1}^{M/2} e^{-4\pi jmbu} \right\} \tag{6.4}$$

After some algebraic manipulations, we get:

$$\mathbf{P}(u) = a\text{sinc}au \left(e^{j\phi_i} + e^{-2\pi jbu}\right) e^{-\pi jbuM} \frac{\sin \pi buM}{\sin 2\pi bu} \tag{6.5}$$

Noting that, as the value of Ψ_i increases from zero to π, the zeroth order (undiffracted) beam will decrease to zero, while the first order beam will increase to its maximum, we find the value of $\mathbf{P}(u)$ for the values of spatial frequency u that correspond to the undiffracted beam and the first order diffraction. These values from Eq. (6.5) are $u = 0$ and $u = \pm 1/2b$, respectively. Therefore we evaluate Eq. (6.5) at these two spatial frequency positions.

$$\mathbf{P}(0) = \frac{aM}{2}\left(e^{j\Psi_i} + 1\right) \tag{6.6}$$

$$\mathbf{P}\left(\frac{1}{2b}\right) = \frac{aM\mathrm{sinc}\,(a/2b)}{2}\left(e^{j\Psi_i} + 1\right) \tag{6.7}$$

If we consider the power at these two positions, we can determine the value of Ψ. From Parceval's theorem, the optical intensity at these two positions will correspond to:

$$I_o = |\mathbf{P}(0)|^2 \tag{6.8}$$

and

$$I_1 = |\mathbf{P}(1/2b)|^2 \tag{6.9}$$

Therefore, we can finally find Ψ_i values, determined between $-\pi < \Psi < \pi$, using Eqs. (6.8) and (6.9):

$$\Psi_i = 2\tan^{-1}\left(\frac{\sqrt{I_o/I_1}}{\mathrm{sinc}(a/2b)}\right) \tag{6.10}$$

Experimentally, a simple characterization layout was prepared as shown in Fig. 6.1, and the pattern $\Psi_i, 0...$ was displayed on the OVP. Then the values of I_o and I_1 were measured for all 128 phase levels Ψ_i, available in our OVP. Then, using Eq. (6.10), the corresponding phase levels were computed. The results are shown in Fig. 6.2.

6.3 Realization of Multifunction Processor

We present the demonstration of the multifunction OVP in two stages. First we present the layout and alignment of the first collimator "A" to the system, and the experimental verification of the filtering and gain equalization functions. Second, we present the procedures for the alignment on the second collimator, and present the experimental results for the add/drop multiplexing function.

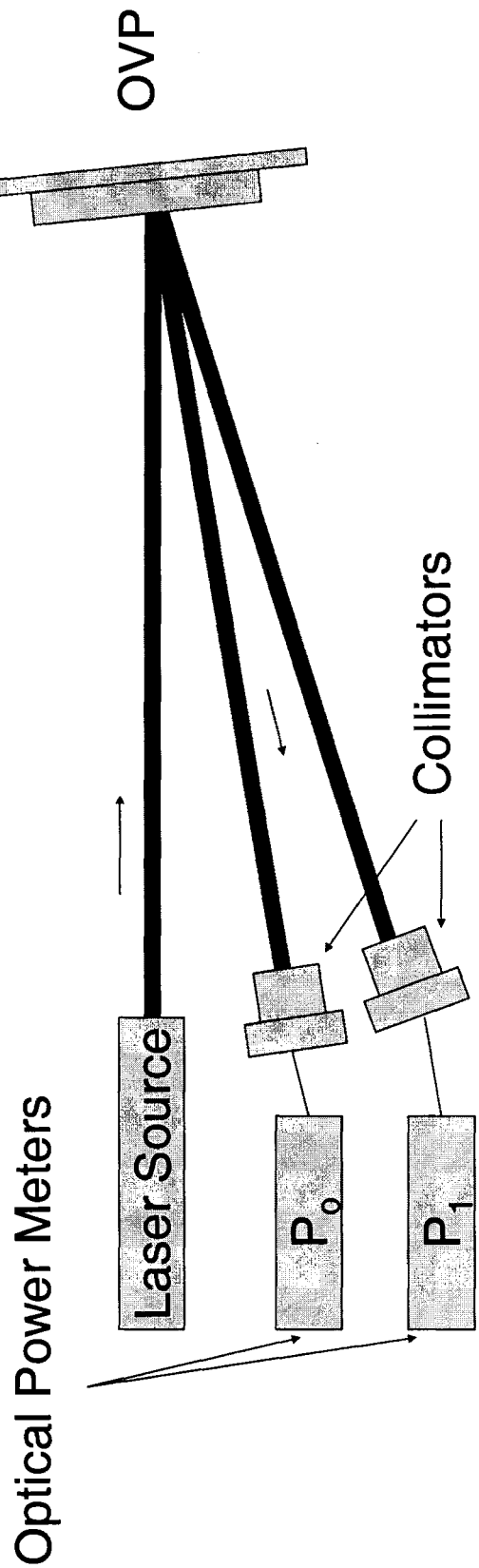

Figure 6.1: Setup for characterizing phase response of the OVP

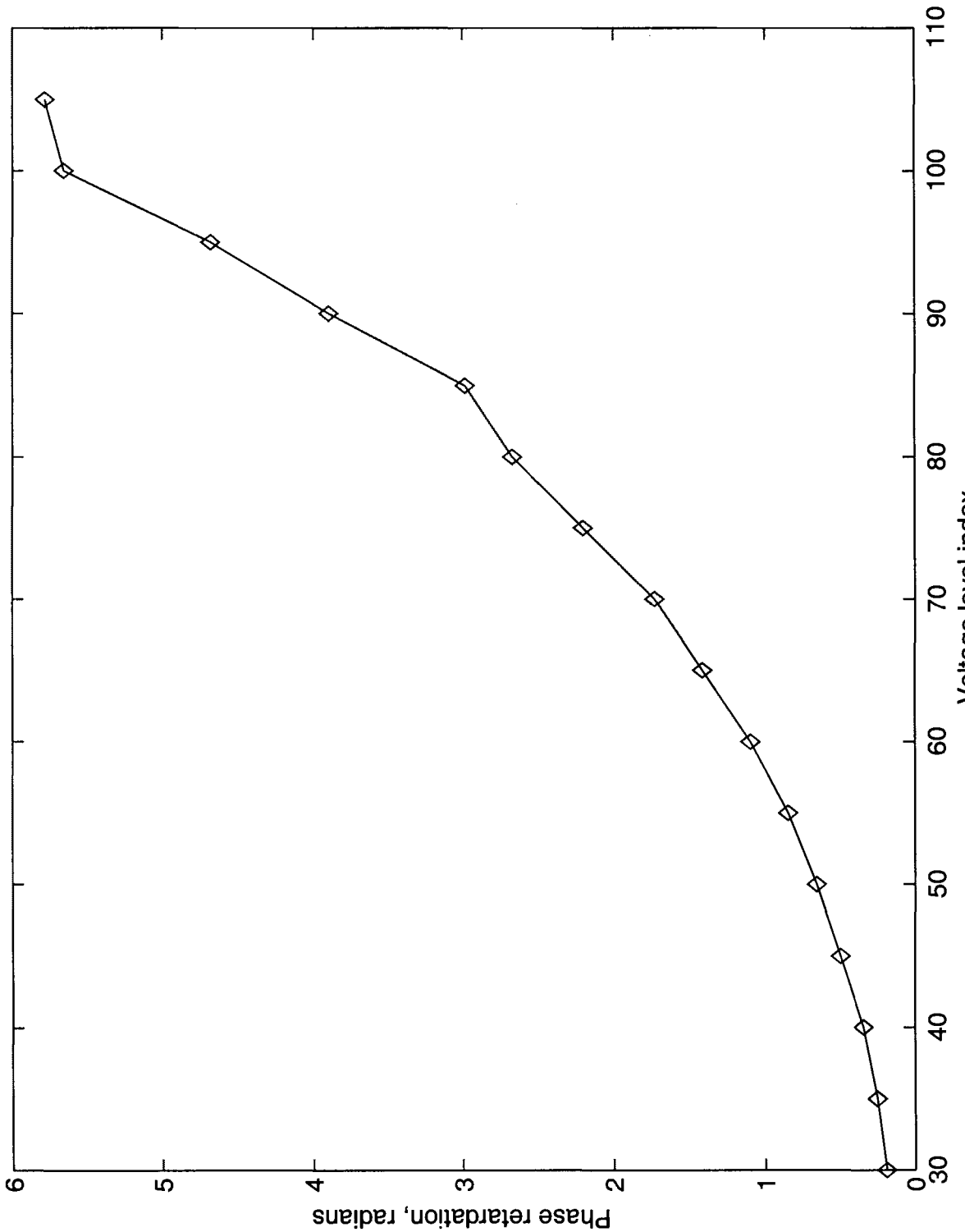

Figure 6.2: Experimental voltage index vs phase retardation characteristics

6.3.1 Layout: Alignment of first OVP

As shown in Fig. 6.3, the fiber input of the collimator is connected to the output port of a 3-port coupler, and its input ports are connected to the tunable laser and the optical spectrum analyzer. Therefore, a signal from the laser is sent to the collimator with a 3-dB loss, and a signal coupled into the collimator is split into the two input ports. This arrangement, is simply to substitute for the lack of a circulator, which would be able to route the signal without the losses associated with a coupler. The connectors used are the FC-APC connectors, which give a very low reflections between the devices. Naturally, the laser sources have built-in isolators that protect them from the coupled light.

For the alignment of the system, first the collimator "A", grating, and the OVP were placed as shown in Fig. 6.3. The collimator and the grating were each placed on a 5-axis stage (with XYZ translation, and 2 axis rotational control), while the OVP was mounted on a rotational two-axis stage.

The center wavelength $\lambda_c = 1550$ nm was chosen, where λ_c is as defined in Section 3.3. The OVP is positioned in such manner that the incident optical beam arrives normally. The angle of incidence of the beam from "A" on the grating, β_A was chosen to be equal to the blaze angle, 37° [119],for satisfying the blaze condition.

The wavelength range is determined by the the dispersion of the grating and the maximum steering angle of the OVP. Since experimentally, the grating and OVP were commercially acquired, the steering angle of the OVP and the dispersion of the grating were both fixed, and thus determined the wavelength range of the device. Therefore for $d_g = 1.67\mu$m and $\theta_{max} = 1.1^o$, we use Eq. (3.3) at $\lambda_N - \lambda_1 = \Delta\lambda = 29$ nm to choose $\lambda_1 = 1535.5$ nm and $\lambda_N = 1564.5$ nm so that we can keep $\lambda_c = 1550$ nm. The specifications of the OVP are given in Appendix E.

The infra-red camera was used for monitoring in real-time the diffraction patterns resulting from the OVP. The infra-red camera measures the beam diffracted from the OVP by being carefully placed to image the *zeroth order* reflection at the grating resulting from the beam that is diffracted from the OVP. This allows us to observe the exact diffraction pattern being sent back to the collimator, since we don't have the ability to observe the optical field distribution at the plane of the collimator.

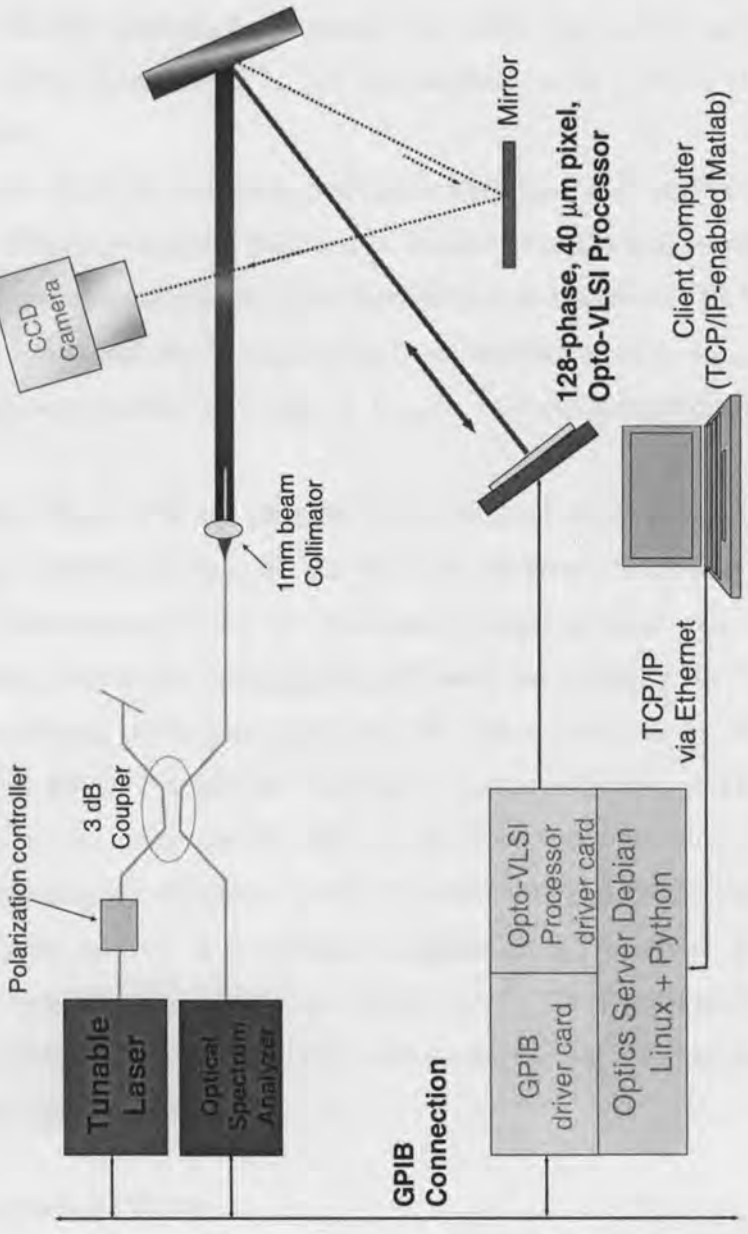

Figure 6.3: Layout of first collimator of multifunction processor

6.3.1.1 Generation of Holograms

As was experimentally demonstrated in Section 5.5, the zeroth order of the OVP will never be zero, owing to imperfections in the phase level generation. Therefore, the design as it stands would not work since $\lambda_c = 1550$ nm would always be present. As a solution, we tilt the OVP in the *vertical* direction, i.e perpendicular to the plane of the grating dispersion. Since the OVP is two dimensional, it can independently steer both in the vertical and horizontal positions.

The simulated annealing hologram generation algorithm was used to generate holograms. Since the fourier transform was used to compute the holograms, using 128 pixels, the number of positions possible using the discrete fourier transform (DFT) was 128 per axis. Therefore, 128 holograms corresponding to all steering angles $-\theta_{max} < \theta_s < \theta_{max}$. All the holograms were steered vertically by $\theta_{max}/8$, to avoid diffraction from the zeroth order.

The alignment of the OVP has therefore to be modified in order to couple the beams that are steering vertically by $\theta_{max}/8$. We load the hologram that steers the beam only vertically, i.e. corresponding to the λ_c. The laser is tuned to λ_c as well. Since it is not possible to directly observe the vertically steered beam, we vertically tilt the mounting of the OVP while observing the coupled power into the optical power meter. When the power is maximized, then the OVP is aligned vertically to the new steering plane.

The position on the hologram for each of the wavelengths arriving on the OVP is determined by masking the hologram except in a circle the size of the collimated beam. Then, by moving the position of the masked hologram, it is possible to identify for each wavelength, the position of the hologram on the OVP. The data with regard to each wavelength, its incident position on the OVP, the corresponding hologram to steer it back, was saved on the client computer.

6.3.1.2 Polarization Effects

One effect that greatly affected the coupling efficiency of the first-order diffraction grating was the polarization dependence of the hologram. This is due to the anisotropy of the liquid crystal. The phase retardation is dependent on the polarization of the incident beam. Therefore, it was necessary to use a polarization controller next to the laser as shown in Fig. 6.3. Therefore, during the alignment process for the vertically steered beam, it was

necessary to adjust the polarization controller until the coupled power was maximized.

6.3.2 Realization of filtering

A single wavelength hologram, as prepared in Section 6.3.1.1 was displayed on the OVP, and the wavelength response was determined by consecutively scanning the tunable laser over the range 1530-1565 nm, and automatically measuring the power level corresponding to each wavelength at the OSA. Thus, is was possible to find the wavelength response of the filter. Furthermore, using the model described in Section 4.3 the expected response was computed. The result of the experimental and theoretical curve are shown in Fig. 6.4. As can be seen from the figure, there is close agreement between the model and the results for areas within 20 dB of the peak. However, at lower power levels, the experimental response is significantly wider. This can be attributed to edge diffraction effects since the hologram loaded has a sharp border.

In order to find the range of wavelengths supported, 64 of the 128 holograms generated, spanning the entire range of wavelength, were loaded serially (one after the other), and for each hologram, the response was measured. The hologram size was chosen to be 14 pixels by 14 pixels, which we found in Section 4.2.2 to be sufficient for faithfully steering the beam with negligible diffractive loss. The results are shown in Fig. 6.5, which demonstrates a uniform shape and near identical response for all the wavelength in the range. As can be seen, the Wavelength range measured is 1532-1561 nm, rather that 1536-1565 nm. This is due to the fact that the center wavelength was approximately normal to the OVP but not exactly so. This poses no real problem, since the range can be easily reconfigured by tilting the OVP if needed. The positions of the holograms, as described in Section 6.3.1.1 would in any case identify the real position and corresponding wavelength for each hologram.

Finally, by simultaneously placing holograms on the OVP that do not overlap, a multi-band filter was demonstrated. The frequency response of the three band hologram and the holograms used to generate it are shown in Fig. 6.6. A draw back, again, revolved around the problem of edge diffraction from the holograms. Thus, if the holograms were placed very close to each other, the undesired diffraction orders would interfere above -20 dB from the peak level. Therefore, in the results of Fig. 6.6 the bands had to be separated by ≈ 10 nm.

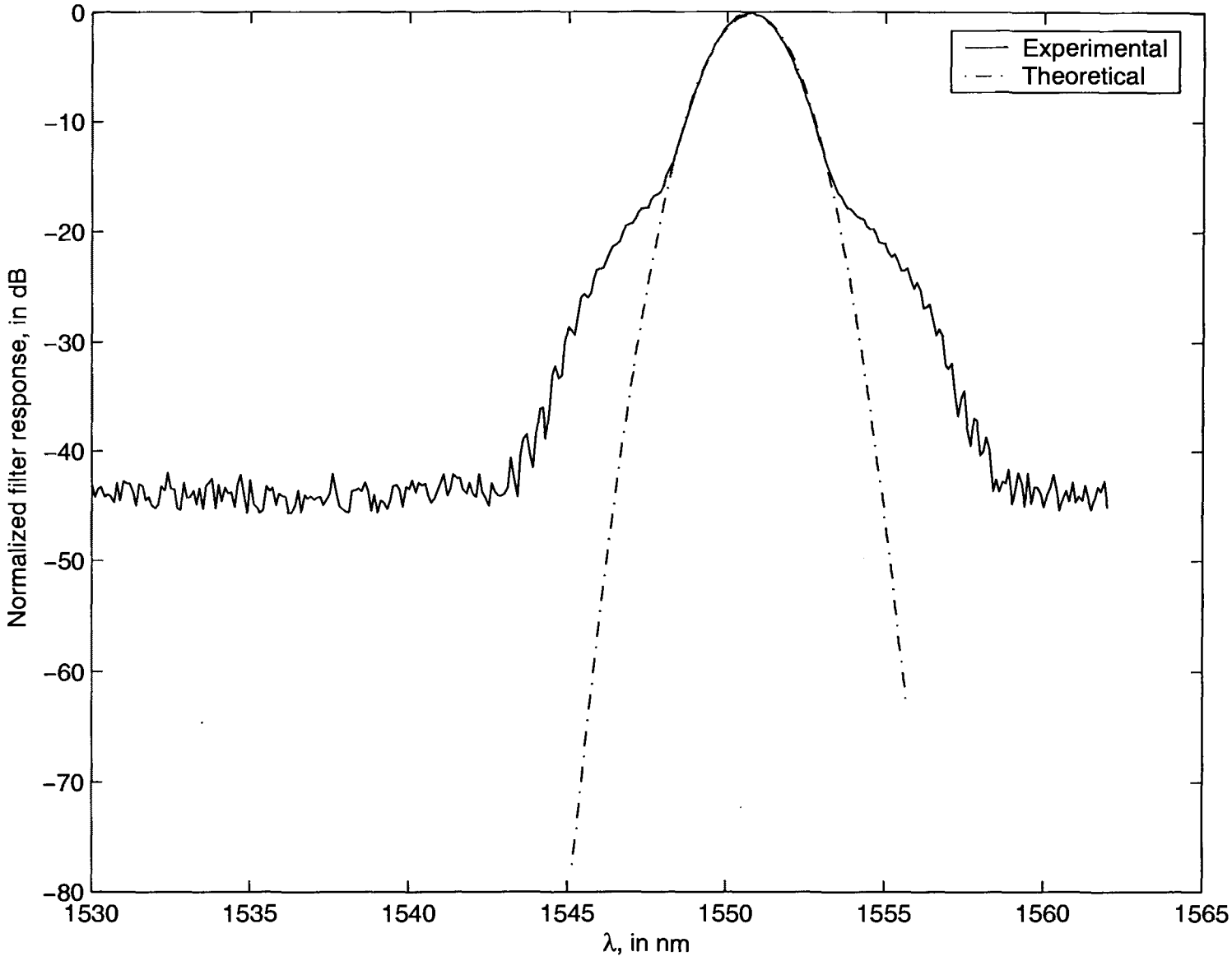

Figure 6.4: Results of experimental and theoretical filter responses

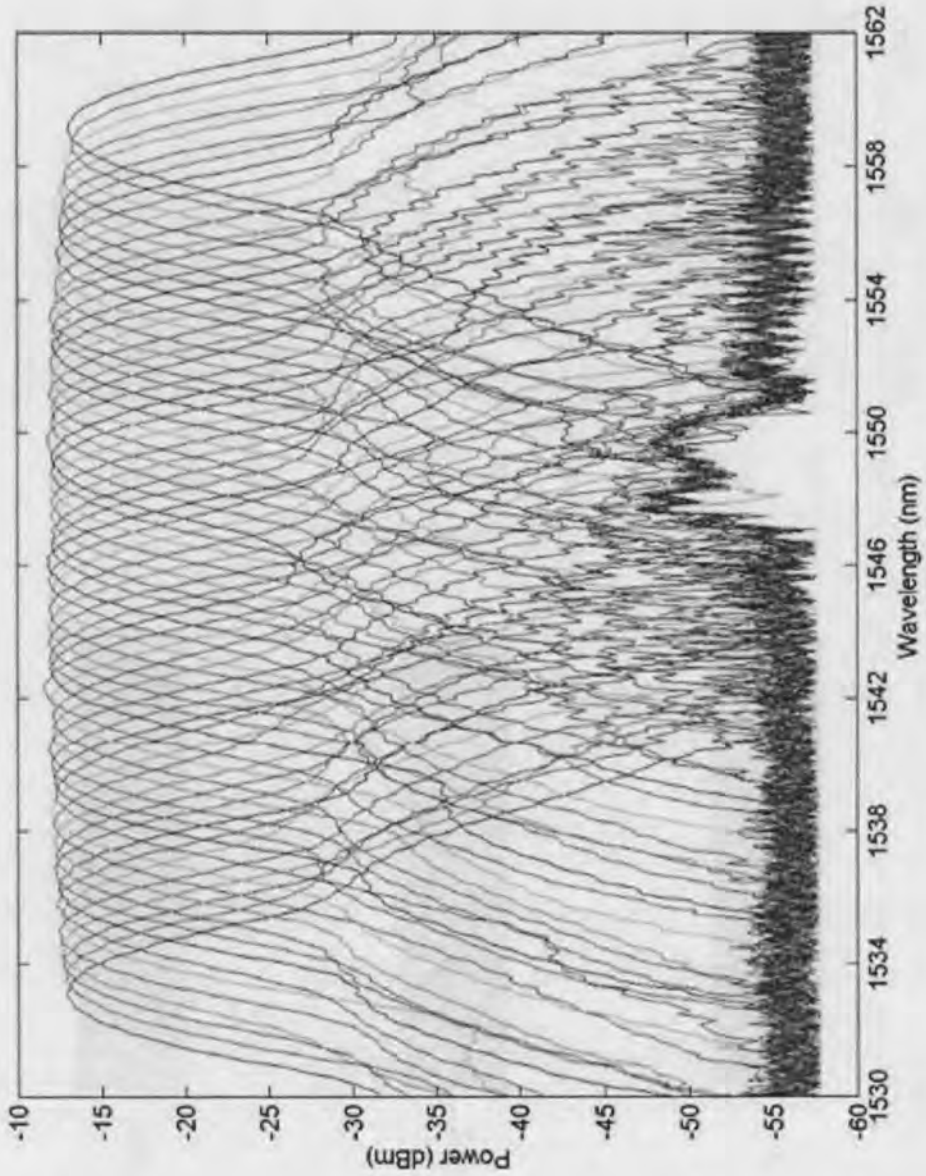

Figure 6.5: Results of the filter for 64 different filtering holograms loaded on the OVP

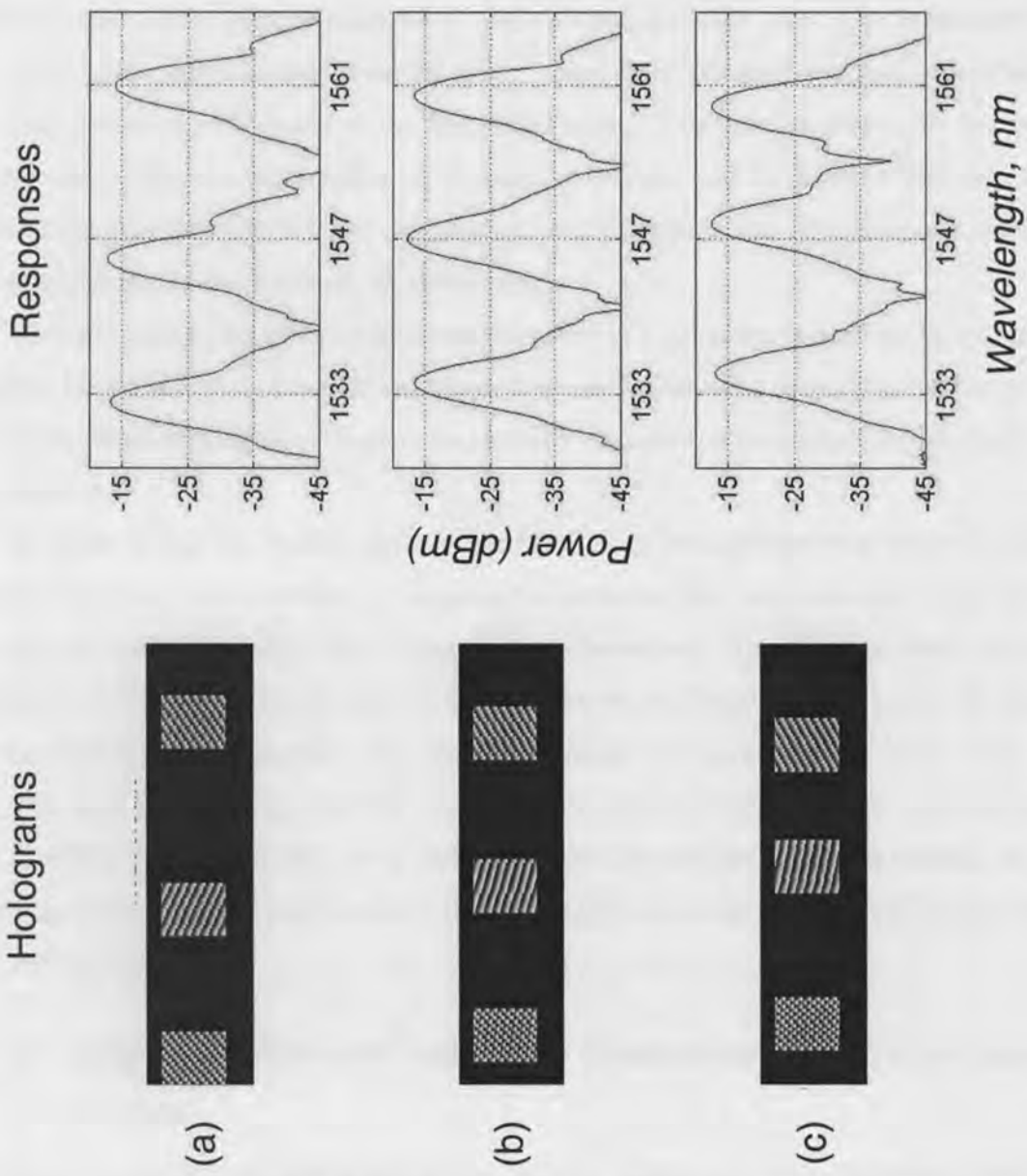

Figure 6.6: Results for a three band filter

6.3.3 Realization of variable attenuation

As was mentioned in Chapter 3, one of the advantages of an opto-VLSI based device is the ability at the channel level to dynamically attenuate the signal. This is demonstrated by changing the size of the holograms as well as the phase range in the hologram. Experimentally this is demonstrated for a single output position (chosen to correspond to $\theta_c = \theta_{max}$, by using a binary phase hologram where the π phase is continually decreased, thereby decreasing the power of the first-order beam. This was conducted for two sizes of circular holograms: for a radius of 10 pixels = 400 μm and 12 pixels = 480 μm. The results are shown in Fig. 6.7. As can be seen from the figure, fine attenuation is possible by changing the phase levels of the holograms.

Another method for finely attenuating the power of a hologram is moving the hologram slightly from the center of the optical beam. This can be achieved by moving the hologram vertically, since moving the hologram horizontally changes the frequency characteristics of the response.

In order to test the channel equalization function of the multifunction device, 6 wavelength channels, corresponding to wavelengths between 1533 and 1561 nm, and optical power was varied by 6 dB. Each channel was consecutively tuned by the laser and the response of the device was recorded by the OSA for all wavelengths in the range, as shown in Fig. 6.8(a). The responses were then superimposed as shown in Fig. 6.8(b). As can be seen from the holograms loaded, the fine attenuation of the signals was accomplished by changing the vertical sizes of the holograms and moving the holograms slightly in the vertical direction. The results indicate that the equalization was achieved with better than 0.2 dB variation.

6.3.4 Alignment of Second Collimator: Realization of Add/Drop multiplexing

In order to align the two collimator system, the two collimators were together bound to a 5 axis stage, with the angle between carefully set to $\approx 10^o$. This is in order to insure that the offset issue described in Section 4.2.3 does not pose a significant problem. Then the two wavelengths λ_1 = 1536 nm and λ_N = 1565 nm are coupled using a 3-dB coupler into a single fiber and the demultiplexed into both collimators "A" and "B". Therefore, both collimators will carry the signal λ_1 and λ_N. As can be seen in Fig. 6.9, the λ_1 beams will

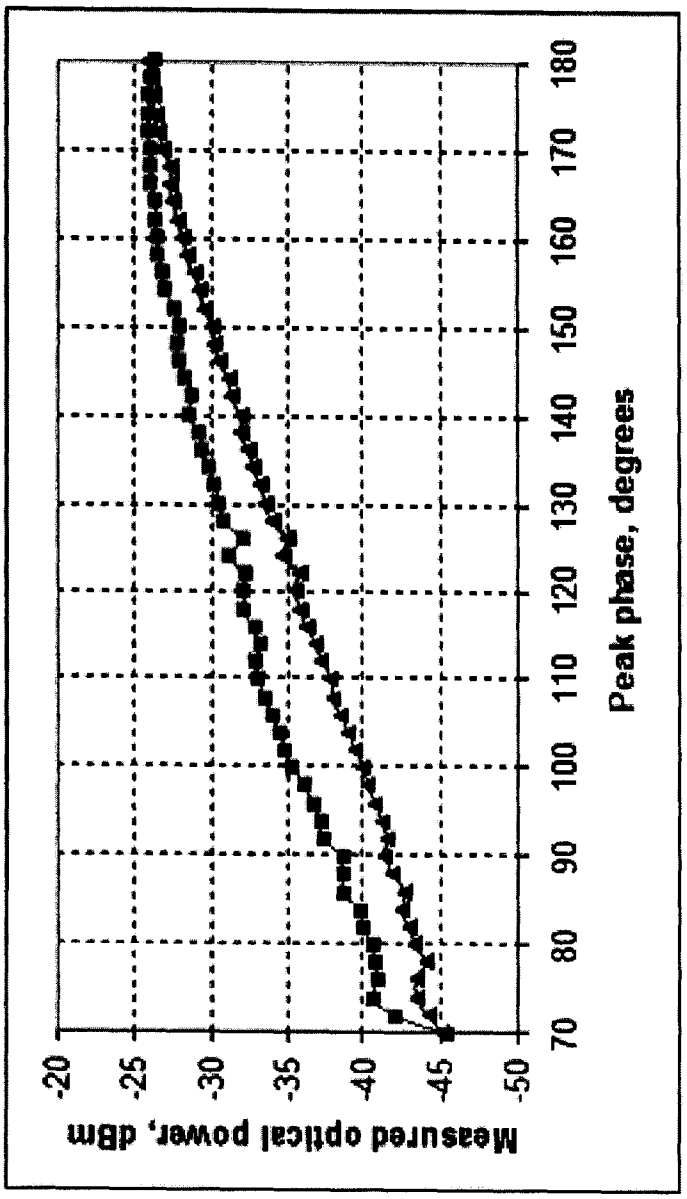

Figure 6.7: Experimental fine resolution attenuation by varying phase levels for two hologram sizes

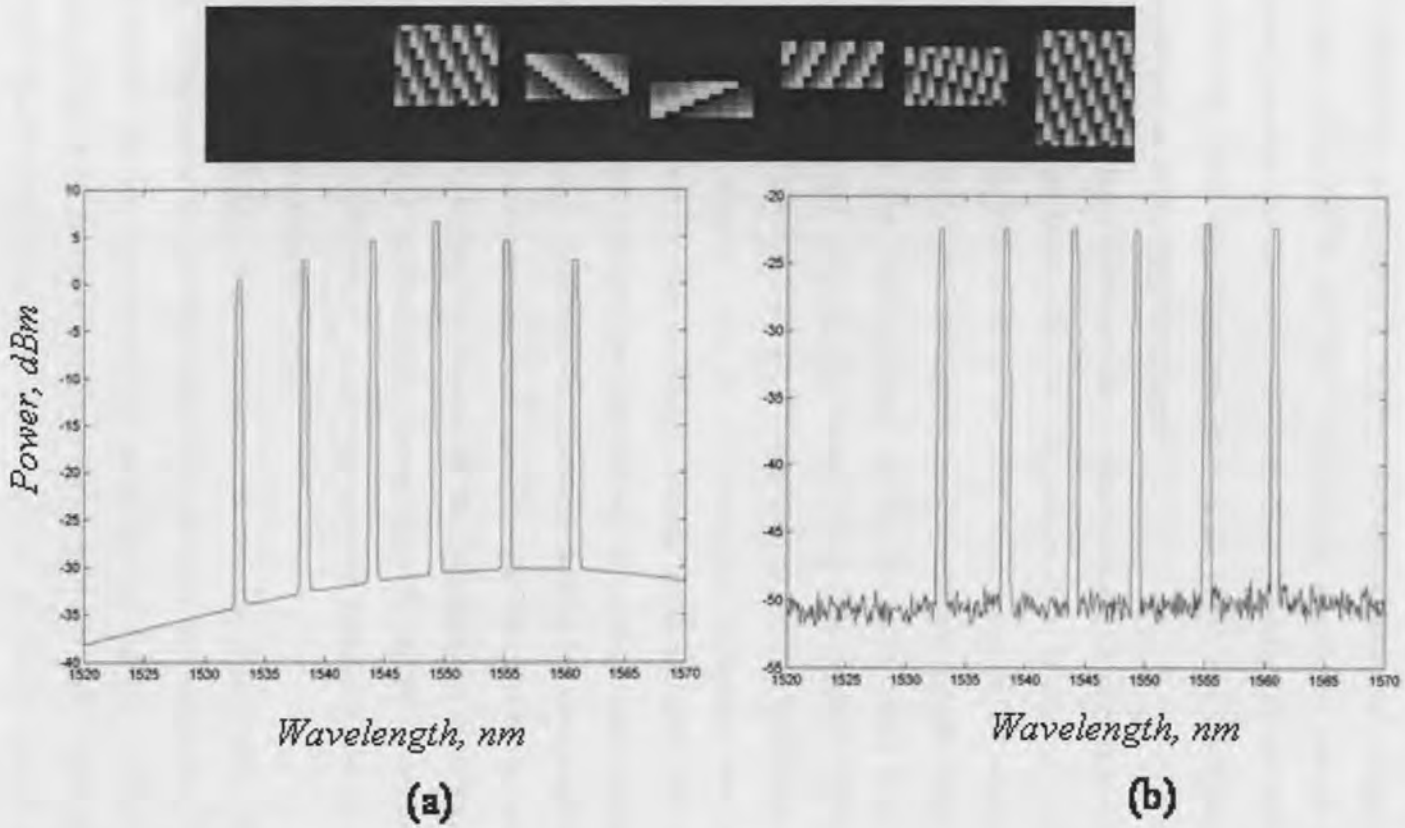

Figure 6.8: Results for gain equalizer

meet and the λ_N will likewise meet, after being diffracted by the grating. As stipulated as a possibility in Chapter 3, the line containing these two crossing points was used as the plane of the OVP. The OVP was carefully aligned to contain the two points. The distance between the two collimators was then carefully moved until it appeared that the two meeting points are on opposite sides of the OVP. The OVP and the collimators were then bound to their respective stages.

In order to align the beams, first it was necessary to align the collimators such that the zeroth order beam from collimator "A" couples into "B" for $\lambda_c = 1550.5$ nm. Therefore, without any hologram loaded on the OVP, the collimator "B" was connected to the OSA, and the collimator "A" was attached to the laser tuned to 1550.5 nm. The two tilt controls of the OVP were then used to align it so that the zeroth order from "A" couples into "B". Then, an unmasked hologram was loaded which only directly vertically steers (similar to the procedure in Section 6.3.1.1). Then using the vertical tilt control of the OVP, the first order beam was aligned. Then the 128 generated holograms were used with their masks such that the beam for each wavelength channel from collimator "A" was coupled back into "A". The hologram position was determined by moving each hologram until the coupled power is maximized. The data on the position and center wavelength of each hologram was the recorded in the computer. Next, the OSA was attached to the collimator "B" and using the same data regarding the position of the hologram for each wavelength recorded, the matching hologram was found that steered from "A" to "B". Therefore this set of hologram can be used to ADD/DROP, while the previous dataset would be used for the channels that would not be added/dropped.

Four laser channels were multiplexed in order to demonstrate the ROADM functionality. They were all launched into the input port for collimator "A" and the output at the output port from collimator "A" as well as the output port from collimator "B" were attached (in turn) to the OSA. Then for each of the four wavelengths, the either of the two holograms were displayed (i.e. the hologram for DROP or no DROP). The results are shown in Fig. 6.10. In Fig. 6.10(a), the four holograms display "no DROP", therefore the four channels, at 1549 nm, 1554 nm, 1560.5 nm, and 1564 nm, are all directed to the WDM output port. In Fig. 6.10(b), the 1549 nm, 1554 nm and 1565 nm channels are directed to the WDM output port, while the 1560.5 nm channel is directed to the DROP port. In Fig. 6.10(c), the 1549 nm and 1564 nm channels are directed to the WDM output port,

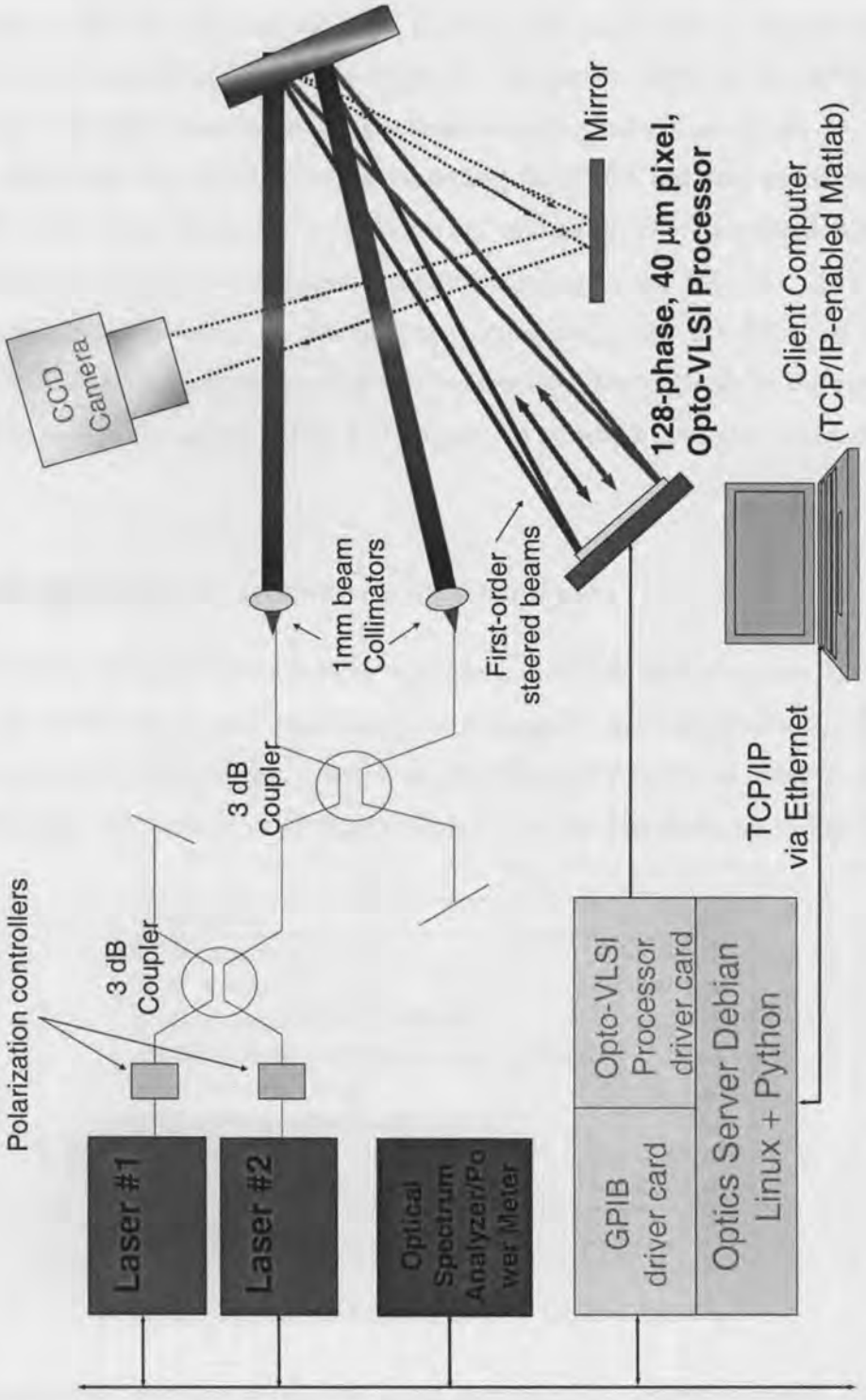

Figure 6.9: Layout of Collimator "A" and "B" for realization of ROADM function

while the 1554 nm and 1560.5 nm channels are directed to the DROP port. Finally, in Fig. 6.10, the holograms are arranged to direct the 1549 nm and 1560.5 nm channels to the DROP port, while the 1554 nm and 1564 nm channels are directed to the WDM output port. As can be seen from figures Fig. 6.10(a-d), the highest crosstalk is observed at the DROP port. However, even there, the crosstalk is never greater than 20 dB.

The experiment was repeated by disconnecting the 1560.5 nm laser source from collimator "A" and connecting it to the input port of collimator "B". Then the holograms for no DROP were displayed on the positions corresponding to the 1549 nm, 1554 nm, and 1564 nm channels. However, for the laser now connected to "B" the displayed hologram was DROP. Using this arrangement, the channel was added successfully at the output port of "A". The results are shown in Fig. 6.11. Again the crosstalk measured was less than 20 dB.

6.4 Experimental Insertion loss analysis

In this section, we consider the sources of power loss in the optical system. In order to identify the power loss in each component, the component was independently attached to a laser source with a determined power level, and the power meter, in order to determine the optical loss. The results are shown in Table 6.1 for the layout shown in Fig. 6.9.

Component	Loss
3-dB coupler 1	3.6 dB
3-dB coupler 2	3.4 dB
grating toward OVP (blazed)	1.55 dB
grating toward collimators (non-blazed)	3.5 dB
collimator coupling	1.5 dB
OVP mirror reflectivity	6 dB
OVP fill factor	3.97 dB
Connectors	<0.2 dB
TOTAL	23.7 dB

Table 6.1: Breakdown of Loss in Optical System

The measured insertion loss for the layout shown in Fig. 6.9 was $\approx$ 25 dB , i.e. with 6 dBm laser power level, peak power of -19 dBm was measured. This agrees quite well with the breakdown of the losses in Table 6.1.

The total loss of 25 dB, of course, is not the insertion loss of the device itself. The

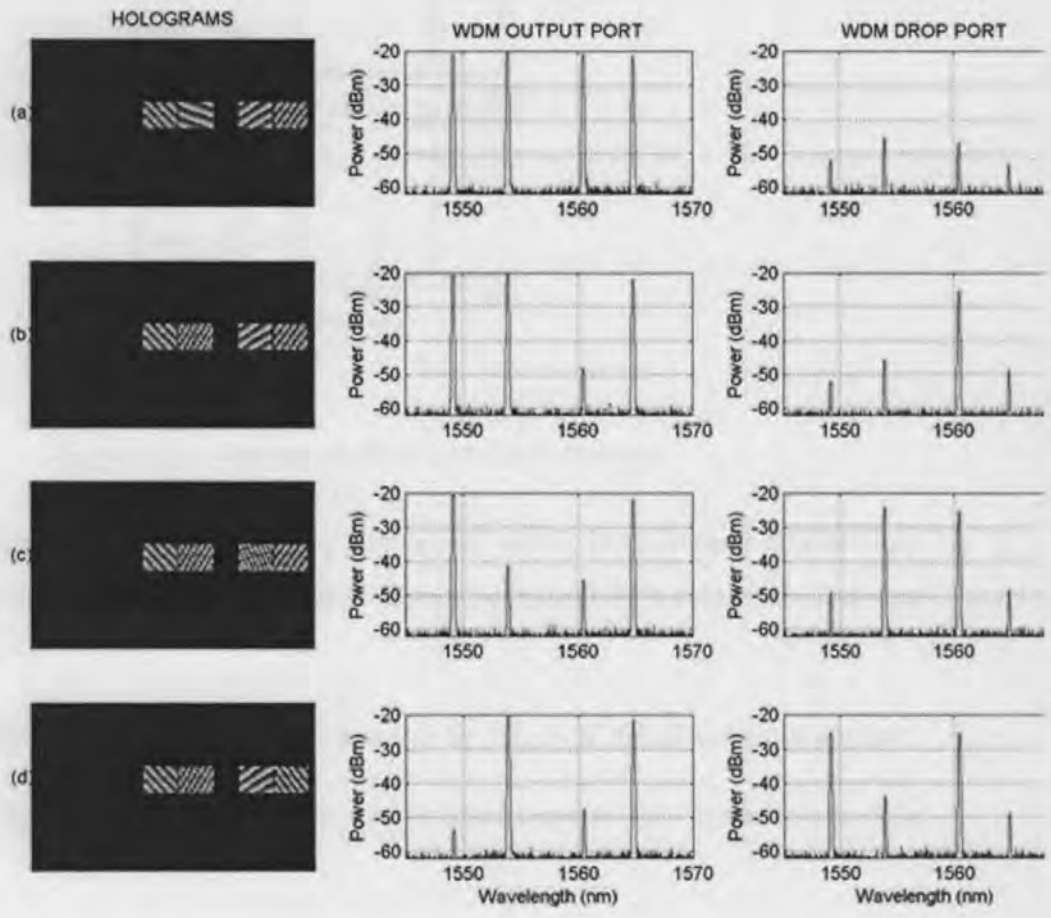

Figure 6.10: Results for ROADM DROP function

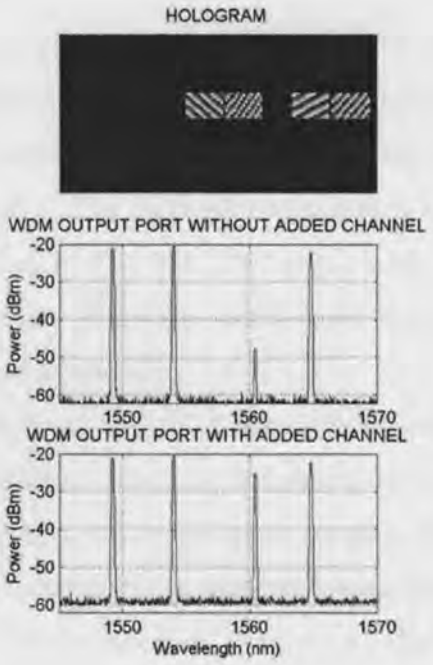

Figure 6.11: Results for ROADM ADD function

two 3-dB couplers used were meant to be circulators, which contributes negligible loss. Further, the losses from the grating and the OVP can be minimized if custom devices were to me constructed:

- The gratings can be designed to give low loss by choice of highly reflective surface.
- The gratings can be designed to have symmetrical blaze at the chosen values of β_A and λ_c.
- The mirror deposited as the top metalization on the OVP can be made to have high reflectivity, as is the case with standard VLSI process for optical MEMS.
- The OVP can have much higher fill factor, by choosing a modern VLSI fabrication technology.

Assuming the above improvements can be made, one may estimate that the total insertion loss of the device may reach as low as < 5 dB.

6.5 Reconfigurable optical splitter

In order to demonstrate the multicasting capability of the OVP, a 1 × 2 dynamic optical splitter was set-up. The layout of the splitter is shown in Fig. 6.12. The input port of the collimator into which the laser is attached (which we will call collimator "A"), was attached to a $\lambda = 1549$ nm laser source. The other port attached to collimator "A" and the second collimator ("B") are attached to the OSA. The zeroth order is coupled by using the two tilt controls of the OVP stage. Since the zeroth order beam is not desired, the beam is slightly tilted in the horizontal direction.

Holograms to steer the beam in 128 directions horizontally are generated using the Simulated Annealing algorithm. Then, the holograms are loaded one after the other in order to identify the holograms corresponding to coupling into the output of "A" or "B". Once the steering angles are identified, the simulated annealing algorithm was again used to steer the incoming beam in both directions. Further, by changing the the relative weights of the two targets in Eq. (5.5), the relative power in each output were changed from -10 dB to -3 dB (equal power). The results are shown in Fig. 6.13.

6.6 Layout of Alternate Design

In this section we present a demonstration of a variable notch filter using the alternative design of the multifunction processor described in Section 3.8. A collimator array with the two collimators aligned parallel to each other was not available, and so a demonstration of the one collimator system was carried out. The layout is shown in Fig. 6.14. Although a transmissive grating, if available, would make the layout easier, it was possible to accommodate the structure with a reflective grating. The focal lengths of Lens 1 and Lens 2 were chosen to be 100 mm each, and the distance between them was set to the same amount.

The grating and Lens 1 were mounted together and the two lenses were aligned to have collinear optical axis. Next an Erbium fiber doped optical source (ASE source) was used to generate a beam with power over a broad wavelength range (1530-1565 nm). These wavelength were dispersed and the coupled beam to the collimator was observed on the OSA through the output port. Then the OVP's tilt were adjusted until a wide range of wavelengths were coupled, indicating that the OVP was aligned. However, the coupled power was observed to decrease significantly outside of the range 1530-1545 nm. This is

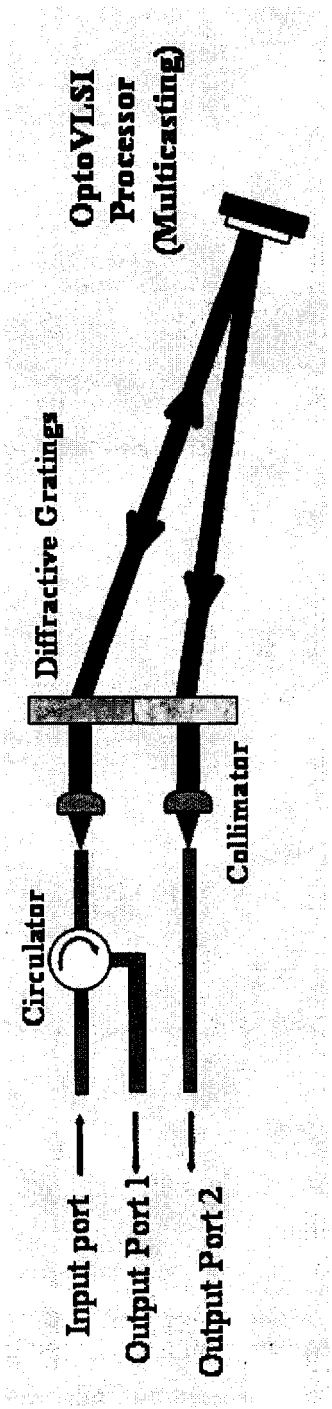

Figure 6.12: Layout of reconfigurable optical splitter

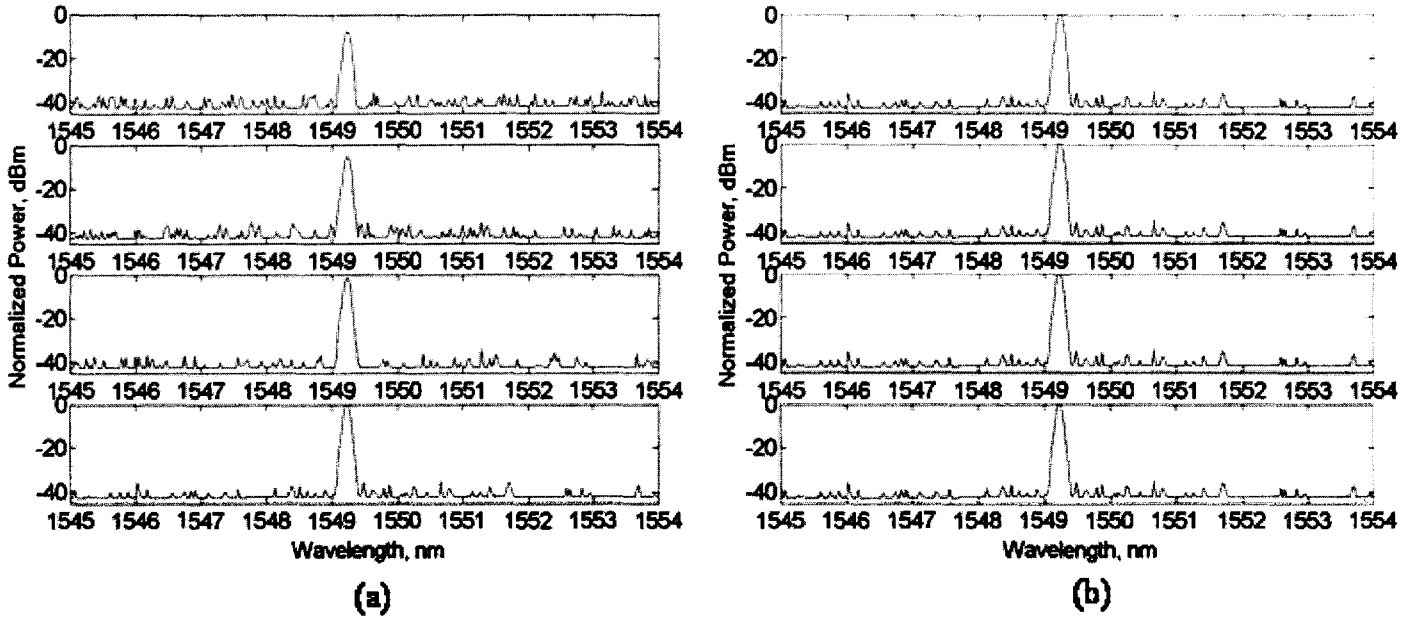

Figure 6.13: Results for Two port variable power splitting

postulated to be due to aberrations, since by tilting the OVP it is possible to shift to another wavelength range, but not increase the wavelength range. The aberrations likely are due to the fact that the collimator incident on the grating travels at an large angle through Lens 1.

A hologram that steers the beam only vertically was loaded on the OVP, and the OVP was tilted again to maximize the coupling efficiency. Then the hologram was altered so that, for a vertical strip in the middle of the OVP, the peak phase level was varied. The wavelength range corresponding to this strip then decreased its power coupling into the OVP, thereby giving a notch filter of varying depth. The results are shown in Fig. 6.15. As can be seen from the results, the variable notch filtering effect is clearly demonstrated. The notch can be made shallow or deep by changing the phase contrast of the hologram.

6.7 Conclusions

In this chapter, we have experimentally demonstrated the multifunction processor, including its functions of filtering, channel equalization, add/drop multiplexing and interconnect. Further, a variable notch filter was demonstrated using the alternate design for multifunction processor. Additionally the phase vs voltage index of the OVP was experimentally determined, by developing a quick but accurate method for characterizing the OVP.

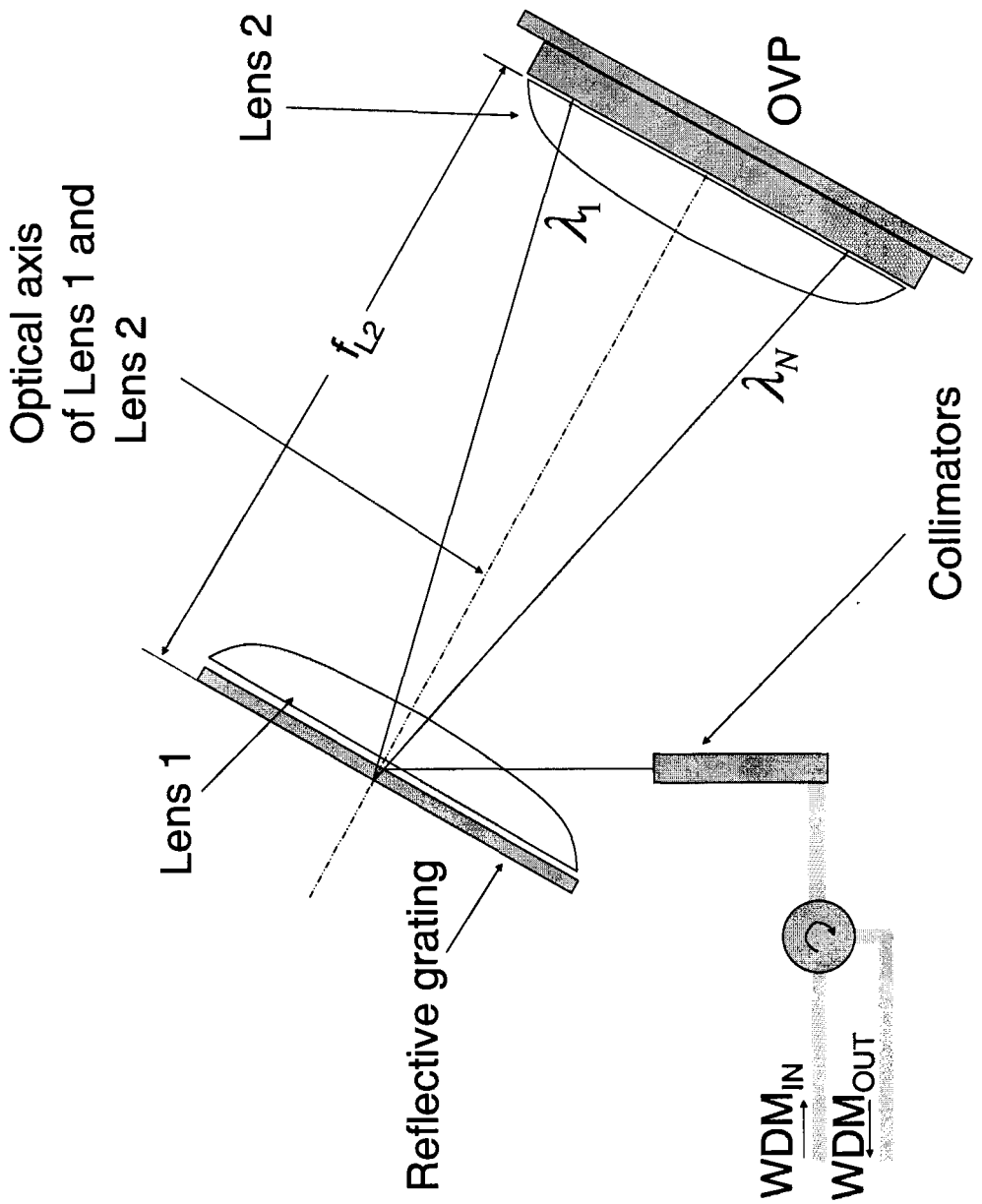

Figure 6.14: Layout of Alternative design

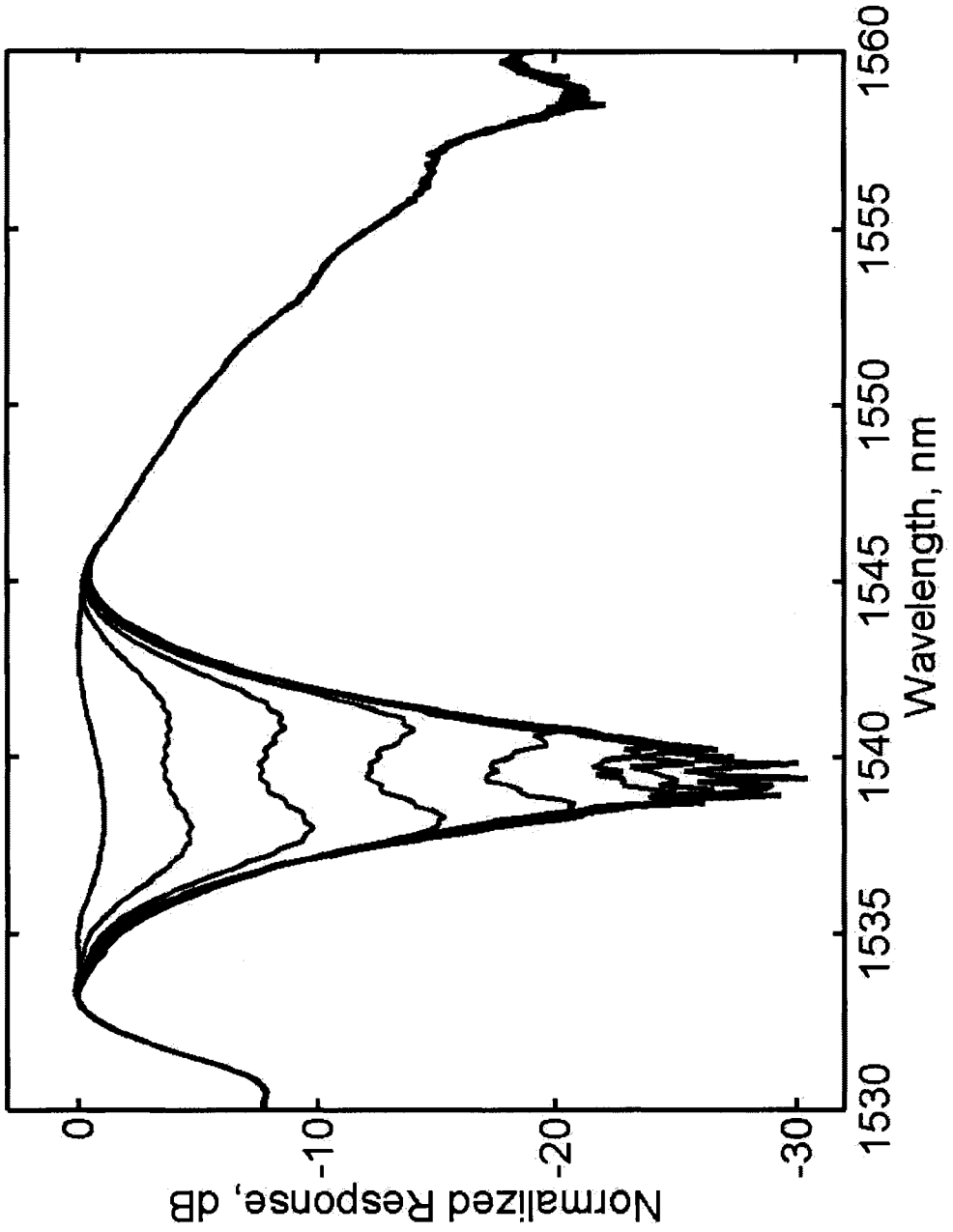

Figure 6.15: Results for notch filtering for the alternative layout

Chapter 7

Conclusions

In this chapter, we briefly assess the feasibility of the Multifunction processor as a WDM device, in order to give context of the salient features of the current work. We further note the possibilities for future research directions opened by this research work.

7.1 Feasibility of Opto-VLSI based WDM Components

In Chapter 6, the Multifunction WDM device was built, and its functionality demonstrated. In this section, we will consider the viability of the device in WDM networks. As was first noted at the beginning of Chapter 2, the salient features of WDM devices are low insertion loss, low polarization dependent loss, low temperature dependence. Another important considerations for a WDM device, especially dense-WDM device, is its scalability as the number of channels increases. We address these considerations individually:

Insertion loss: The measured insertion loss for the device was very large ($\approx 25dB$). However, as noted in Section 6.4, some of the loss measured ($7.2dB$) is outside the actual device, and other losses, such as from the grating and the OVP, can be dramatically improved by using current optical and VLSI technology. Therefore, we expect the insertion loss to drop significantly with the right equipment available.

Polarization dependence: The polarization dependence of an liquid crystal device is expected to be high, and this device is no exception. The device required a polarization controller for each channel, and for a large number of channel this quickly becomes untenable. However, this problem can be solved by using a polarization independent OVP. By placing a quarter-wave plate between the liquid crystal layer and the reflective layer, it is

possible to ensure that both polarization states experience the same retardation. This is because the quarter wave plate rotates the polarization state of the field by 90 degrees, thereby ensuring that each beam experiences both polarization states equally. The polarization independence of such setups has already been demonstrated [120].

Temperature dependence: No temperature dependence was detected in the operation of the device, since it does not contain any components that exhibit high temperature sensitivity. The liquid crystal itself is temperature dependent, however, over the normal working range of room temperature, the liquid crystal displays high stability.

Scalability: The scalability of a WDM device is determined by its ability to incorporate ever increasing number of channels. As can be seen from Chapter 3, the number of channels scales linearly with the extent of the OVP, which means that additional channels can simply be incorporated by proportionally increasing the size of the OVP. However, the steering angle required would also increase as the size of the OVP increases, which makes the multifunction processor have limited scalability. However, the alternative design for OVP solves this problem by ensuring that a fixed steering is required, *regardless of the number of channels.* Thus the multifunction device, utilizing the alternate layout, would be scalable to ever larger number of channels.

Further, the following specifications were obtained for the Opto-VLSI based WDM device:

Reconfiguration time: The reconfiguration time of the device consists of the OVP's reconfiguration time, which, as specified in Appendix E, is at a maximum 1 ms.

Crosstalk figure: The worst-case cross-talk figure experimentally obtained is 20 dB (see Section 6.3.4), which is comparable to WDM components described in the literature review. However, as noted in Section 5.5, the OVP used has significant errors in displaying the hologram. Therefore, with better OVPs, the crosstalk figure should improve.

Further we note that, the Opto-VLSI based multifunction device is optically transparent, thus, it is insensitive to the bitrate or protocol used in the signal. For example, it can accomodate digital or analog signals, it can use the OC-192 or the OC-768 bitrates.

In conclusion, we propose that the Opto-VLSI based WDM multifunction device is a promising platform for WDM components due to its versatility, scalability, as well as the ability to meet the specifications of current devices.

7.2 Future work

In this section, we list some possibilities for research exploration opened by the current research:

7.2.1 OVP Fabrication

- **Rectangular pixels:** The multifunction processor requires large steering angles in one direction only. The vertical direction need to give a small steering in order to counter the effect of zeroth order diffraction beam. Therefore, the size of the pixels in the horizontal direction can be greatly decreased and the size in the vertical direction increased, without changing the size of the pixel, it will be possible to realize larger steering angles.

- **Insertion of quarter-wave plate:** As noted in the previous section, the insertion of a quarter wave plate makes the OVP nearly polarization insensitive, thereby decreasing the number of components needed for the device by not requiring polarization controllers.

- **Incorporation of sensors:** If sensors are incorporated in the pixels, it will be possible to determine the position of the beam on the OVP without moving holograms across the face of the OVP, as was the method used in Chapter 6. A method for layout of the sensors as well as algorithms for computation of the position are given in Appendix D.

- **Reflective Aluminum Mirrors and VLSI processing:** By using high reflectivity Aluminum, which is available in standard VLSI process, it is possible to greatly decrease the losses of the device at the stage of the OVP. Further by using recent VLSI technologies, it is possible to greatly increase the fill-factor of the pixels.

7.2.2 Architectures

- **Two steering stages:** As the optical loss at the OVP is decreased it should be possible to have two OVP steering stages, thereby decreasing the crosstalk (as noted in Section 4.4). Therefore, interconnects with low crosstalk and high efficiency will be possible for WDM switches and multiplexers.

- **Glass integration:** For easy packaging the multifunction device can be incorporated in a glass substrate. This allows an easy mechanism for all the components to be securely attached to the device, and the alignment to be set without possibility of misalignment later.

Bibliography

[1] B. E. A. Saleh and M. C. Teich. *Fundamentals of Photonics.* John Wiley, New York, 1991.

[2] T. Miya. Silica-based planar lightwave circuits: Passive and thermally active devices. *IEEE Journal on Selected Topics in Quantum Electronics*, 6(1):38–45, 2000.

[3] L. Y. Lin, E. L. Goldstein, and R. W. Tkach. Free-space micromachined optical switches for optical networking. *IEEE Journal on Selected Topics in Quantum Electronics*, 5(1):4–9, 1999.

[4] J. S. Harris. Mems: How to make, model and use microdevices in a macro-world. In *American Physical Society (APS) meeting*, Mar 2001.

[5] Kim L. Tan, William A. Crossland, and Robert J. Mears. Dynamic holography for optical interconnections. i. noise floor of low-cross-talk holographic switches. *Journal of the Optical Society of America A*, 18(1):195–204, 2001.

[6] G. E. Moore. Cramming more components onto integrated circuits. *Electronics*, 38(8), 1965.

[7] P. P. Gelsinger, P. A. Gargini, G. H. Parker, and A. Y. C. Yu. Microprocessors circa 2000. *IEEE Spectrum*, 26(10):43–47, 1989.

[8] J. M. Kahn and K. P. Ho. A bottleneck for optical fibers. *Nature*, 411:1007–1009, 2001.

[9] P. P. Mitra and J. B. Stark. Non-linear limits to the information capacity of optical fibre communication. *Nature*, 411:1027–1030, 2001.

[10] S. J. B. Yoo. Wavelength conversion technologies for wdm network applications. *IEEE Journal of Lightwave Technology*, 14(6):955–966, 1996.

[11] M. Ajmone Marsan, Andrea Bianco, Emilio Leonardi, and Fabio Neri. Topologies for wavelength-routing all-optical networks. *IEEE/ACM Transactions on Networking (TON)*, 1(5):534 - 546, 1993.

[12] G. R. Hill, P.J. Chidgey, F. Kaufhold, T. Lynch, O. Sahlen, M. Gustavsson, M. Janson, B. Lagerstrom, G. Grasso, F. Meli, S. Johansson, J. Ingers, L. Fernandez, S. Rotolo, A. Antonielli, S. Tebaldini, E. Vezzoni, R. Caddedu, and N. Caponio. A transport network layer based on optical network elements. *Journal of Lightwave Technology*, 11(5/6):667–679, 1993.

[13] G. Keiser. A review of wdm technology and applications. *Optical Fiber Technology*, 5:3–39, 1999.

[14] Richard A. Barry and Pierre A. Humblet. Models of blocking probability in all-optical networks with and without wavelength changers. *IEEE Journal of Selected Areas in Communications*, 14(5):858–867, 1996.

[15] R. Ramaswami and K. N. Sivarajan. *Optical Networks: A practical perspective.* Harcourt, San Diego, CA, 2002.

[16] Ivan P. Kaminow and Thomas L. Koch (eds.). *Optical Fiber Communications IIIa.* Academic Press, San Diego CA, 1997.

[17] H. Okayama, Y. Okabe, and T. Kamijoh. Double stage flat passband acousto-optic wavlength filter. *Optical Review*, 4:300–2, 1997.

[18] Ivan P. Kaminow and Thomas L. Koch (eds.). *Optical Fiber Communications IIIb.* Academic Press, San Diego CA, 1997.

[19] J.J. Pan and Y. Shi. Steep skirt fibre bragg grating fabrication using a new apodised phase mask. *IEE Electronics Letters*, 33(22):1895–96, 1997.

[20] H. van de Stadt and J.M. Muller. Multimirror fabry-perot interferometers. *Journal of Optical Society of America A (JOSA A)*, 2(8):1363–70, 1985.

[21] C.K. Madsen and J.H. Zhao. *Optical Filter Design and Analysis: A Signal Processing Approach.* John Wiley and Sons, New York, 1999.

[22] F. Bilodeau, K. O. Hill, B. Malo, D. C. Johnson, and J. Albert. High-return-loss narrowband all-fiber bandpass bragg transmission filter. *IEEE Photonic Technology Letters*, 6:80–82, 1994.

[23] J.-L. Archambault, P. St. J. Russell, S. Barcelos, P. Hua, and L. Reekie. Grating-frustrated coupler: a novel channel-dropping filter in single-mode optical fiber. *Optics Letters*, 19(3):180–182, 1994.

[24] V. Mizrahi, R. Erdogan, D. J. DiGiovanni, P. J. Lemaire, W. M. MacDonald, S. G. Kosinski, S. Cabot, and J. E. Sipe. Four channel fibre grating demultiplexer. *IEE Electronic Letters*, 30:780–781, 1994.

[25] H.A. MacLeod. *Thin Film Optical Filters.* Institute of Physics Publishing, Bristol, 2001.

[26] S. V. Kartalopoulos. *Introduction to DWDM technology: Data in a rainbow.* IEEE Press, New York, 1999.

[27] Dan Sadot and Efraim Boimovich. Tunable optical filter for dense wdm networks. *IEEE Communications Magazine*, 36(12):50–55, 1998.

[28] J. Stone and L.W. Stulz. Pigtailed high finesse tunable FP interferometer with large, medium and small FSR. *IEE Electronics Letters*, 23:781–83, 1987.

[29] J. Y. Liu and K. M. Johnson. Analog smectic c* ferroelectric liquid crystal fabry perot optical tunable filter. *IEEE Photonics Technology Letters*, 7(11):1309–11, 1995.

[30] A. Locco, H.G. Limberger, and R.P. Salathe. Bragg grating fast tunable filter. *IEE Electronics Letters*, 33(25):2147–8, 1989.

[31] J. Hubner, D. Zauner, and M. Kristensen. Strong sampled bragg grating for wdm applications. *IEEE Photonics Technology Letters*, 10(4):552–54, 1998.

[32] H. Herrmann, K. Schafer, and C. Schmidt. Low loss tunable integrated acoustooptical wavelength filter in $LiNbO_3$ with strong sidelobe suppression. *IEEE Photonics Technology Letters*, 10:120–22, 1998.

[33] E. L. Wooten, K. M. Kissa, A. Yi-Yan, E. J. Murphy, D. A. Lafaw, P. F. Hallemeier, D. Maack, D. V. Attanasio, D. J. Fritz, and G. J. McBrien. A review of lithium

niobate modulators for fiber-optic communication systems. *IEEE Journal on Selected Topics in Quantum Electronics*, 6(1):69–82, 2000.

[34] B. H. Verbeek, C. H. Henry, N. A. Olsson, K. J. Orlowsky, R. F. Kazarinov, and B. H. Johnson. Integrated four channel mach-zehnder multi/demultiplexer fabricated with phosphorous doped SiO2 waveguides on Si. *Journal of Lightwave Technology*, 6:1011–15, 1988.

[35] J. P. Weber, B. Stoltz, H. Sano, M. Dasler, O. Oberg, and J. Waltz. An integratable polarization-independent tunable filter for wdm systems: The multigrating filter. *Journal of Lightwave Technology*, 14(12):2719–35, 1996.

[36] E.C. Vail, M.S. Wu, G.S. Li, L. Eng, and C.J. Chang-Hasnain. Gaas micromachined widely tunable fabry-perot filters. *IEE Electronics Letters*, 31(3):228–9, 1995.

[37] P. Tayebati, P. D. Wang, D. Vakhshoori, and R. N. Sacks. Widely tunable fabry perot filter using ga al as al ox deformable mirros. *IEEE Photonic Technology Letters*, 10(3):394–396, 1998.

[38] Eugene Hecht. *Optics*. Pearson Addison Wesley, Reading, MA, 2001.

[39] C. Dragonne. An n x n optical multiplexer using a planar arrangement of two star couplers. *IEEE Photonics Technology Letters*, 3:812–815, 1991.

[40] C. Dragonne. Efficient n x n star couplers using fourier optics. *Journal of Lightwave Technology*, 7(3):479–489, 1989.

[41] W. A. Pasmooij, P. A. Mandersloot, and M. K. Smit. Prism-coupling of light in to narrow planar optical waveguides. *Journal of Lightwave Technology*, 7(1):175–180, 1989.

[42] A. P. Vellekoop and M. K. Smit. Four-channel integrated-optic wavelength demultiplexer with weak polarization dependence. *Journal of Lightwave Technology*, 9(3):310–314, 1991.

[43] M. K. Smit. New focussing and dispersive planar component based on optical phase array. *IEE Electronic Letters*, 24:385, 1988.

[44] R. Adar, C. H. Henry, C. Dragone, R. C. Kistler, and M. A. Milbrodt. Broad-band array multiplexers made with silica waveguides on silicon. *Journal of Lightwave Technology*, 11(2):212–219, 1993.

[45] H. Takahashi, Y. Hibino, Y. Ohmori, and M. Kawachi. Polarization-insensitive arrayed-waveguide wavelength multiplexer with birefringence compensating film. *IEEE Photonic Technology Letters*, 5(6):707–709, 1993.

[46] Hideo Kosaka, Takayuki Kawashima, Akihisa Tomita, Masaya Notomi, Toshiaki Tamamura, Takashi Sato, and Shojiro Kawakami. Superprism phenomena in photonic crystals: Toward microscale lightwave circuits. *Journal of Lightwave Technology*, 17(11):2032–2038, 1999.

[47] J.H. Chiao. Liquid crystal optical harmonic equalizers. In *IEEE LEOS 2001 Topical Summer Meeting*, 2001.

[48] B. Offrein, F. Horst, G. Bona, R. Germann, H. M. Salemink, and R. Beyeler. Adaptive gain equalizer in high-index-contrast SiON technology. *IEEE Photonics Technology Letters*, 12:504–506, 2000.

[49] C.R. Doerr, M. Cappuzzo, E. Laskowski, A. Paunescu, L. Gomez, L. W. Stulz, and J. Gates. Dynamic wavelength equalizer in silica using the single-filtered-arm interferometer. *IEEE Photonics Technology Letters*, 11(5):581–583, 1999.

[50] X. Y. Zou S.H. Huang, S.-M. Hwang, A. E. Willner, Z. Bao, and D. A. Smith. Experimental demonstration of dynamic network equalization of three 2.5 gb/s wdm channels over 1000 km using acousto optic tunable filters. *IEEE Photonics Technology Letters*, 8(9):1243–5, 1996.

[51] D. S. Kim, J. C. Dries, M. R. Gokhale, and S. R. Forrest. Optoelectronic inp-ingaas smart pixels for optical interconnections and computing. *IEEE Journal of Quantum Electronics*, 33(8):1407–1416, 1997.

[52] J.E. Ford and J.A. Walker. Dynamic spectral power equalization using micro-opto-mechanics. *IEEE Photonics Technology Letters*, 10:1440–1442, 1998.

[53] Selam Ahderom, Mehrdad Raisi, Kamal Alameh, and Kamran Eshraghian. Adaptive wdm equalizer using opto-vlsi beam processing. *IEEE Photonics Technology Letters*, 15(11):1603–05, November 2003.

[54] W. Fix, M. Walker, W. Geisselbrecht, P. Kiesel, G. H. Dohler, P. Velling, W. Prost, and F. J. Tegude. A monolithically integrated smart pixel based on a photoconductive switch and a n-i-p-i modulator. In *Proceedings of CLEO '99*, pages 198–199, 1999.

[55] R. Y. Loo, G. Tangonan, V. Jones, H. Yen, Y. Liu, and S. R. Forrest. High bandwidth ingaas p-i-n photodetector array for optoelectronic switching applications broadband analog and digital optoelectronics, optical multiple access networks, integrated optoelectronic smart pixels. In *Summer Topical Meeting Digest*, pages B19–B20, 1992.

[56] N. A. Jackman, S. H. Patel, and B. P. Mikkelsenand S. K. Korotky. Optical cross connects for optical networking. *Bell Laboratories Technical Journal*, 4(1):262–281, 1999.

[57] L. Eldada and L. W. Shacklette. Advances in polymer integrated optics. *IEEE Journal on Selected Topics in Quantum Electronics*, 6(1):54–68, 2000.

[58] M. Mistuhiro, M. Sato, F. Shimokawa, and Y. Nishida. Micromechanical optical switches based on thermocapillary integrated in waveguide substrate. *Journal of Lightwave Technology*, 17(1):14–18, 1999.

[59] J. E. Fouquet, S. Venkatesh, M. Troll, D. Chen, H. F. Wong, and P. W. Barth. A compact scalable cross-connect switch using total internal reflection due to thermally-generated bubbles. In *Lasers and Electro-Optics Society Annual Meeting (LEOS '99)*, volume 2, pages 169–170, 1998.

[60] P. M. Hagelin, U. Krishnamoorthy, J. P. Heritage, and O. Solgaard. Scalable optical cross-connect switch using micromachined mirrors. *IEEE Photonics Technology Letters*, 12(7):882–884, 2000.

[61] P. Helin, M. Mita, and H. Fujita. Self-aligned mirror and v-grooves in freespace micromachined optical switches. *IEE Electronics Letters*, 36(6):563–564, 2000.

[62] P. Helin, T. Bourouina, M. Mita, G. Reyne, and H. Fujita. New self-aligned micromachining process for large free-space optical cross-connects. In *Proceedings of IEEE/LEOS International Conference on Optical MEMS*, pages 119–120, 2000.

[63] H. S. Hinton. Progress in smart pixel technologies. *IEEE Journal of Selected Topics in Quantum Electronics*, 2(1), 1996.

[64] R. Mears, W. A. Crossland, M. P. Dames J. R. Collington amd M. C. Parker, S. T. Warr, T. D. Wilkinson, and A. B. Davey. Telecommunications application of ferroelectric liquid crystal smart pixels. *IEEE Journal of Selected Topics in Quantum Electronics*, 2(1), 1996.

[65] T. H. Barnes, Tomoaki Eiju, Kiyofumi Matsuda, Hiroyuki Ichikawa, Mohammad R. Taghizadeh, and Jari Turunen. Re-configurable free-space optical interconnections with a phase-only liquid crystal spatial light modulators. *Applied Optics*, 31(26):5527–35, 1992.

[66] W. A. Crossland, I. G. Manolis, M. M. Redmond, K. L. Tan, T. D. Wilkinson, A. Chu, V. A. Handerek, M. J. Holmes, T. Parker, I. G. Bonas, B. Robertson, S. T. Warr, C. Stace, H. J. White, R. A. Woolley, and G. Henshall. Beam steering optical switches using lcos: the 'roses' demonstrator. In *Proc. Microdisplay and Smart Pixel Technologies*, pages 1/1 –1/7, 2000.

[67] Lih Y. Lin and Evan L. Goldstein. Opportunities and challenges for mems in lightwave communications. *IEEE Journal On Selected Topics In Quantum Electronics*, 8(1):163–172, 2002.

[68] Takashi Mizuochi, Tadayoshi Kitayama, Katsuhiro Shimizu, and Katsuyoshi Ito. Interferometric crosstalk-free optical add/drop multiplexer using mach-zehnder based fiber gratings. *Journal Of Lightwave Technology*, 16(2):265–276, 1998.

[69] Beatriz Ortega, Liang Dong, and Laurence Reekie. All-fiber optical add-drop multiplexer based on a selective fused coupler and a single fiber bragg grating. *Applied Optics*, 37(33):7712–15, 1998.

[70] M. Diez, J. Delgado-Pinar, J. Mora, L. Cruz, and M. V. Andrés. Dynamic fiber-optic add-drop multiplexer using bragg gratings and acousto-optic-induced coupling. *IEEE Photonics Technology Letters*, 15(1):84–86, 2003.

[71] B.J. Offrein, G.L. Bona, F. Horst, H.W.M. Salemink, R. Beyeler, and R. Germann. Wavelength tunable optical add-after-drop filter with flat passband for wdm networks. *IEEE Photonics Technology Letters*, 11(2):239–241, 1999.

[72] Kuninori Hattori, Masaki Fukui, Masahiko Jinno, Manabu Oguma, and Kimio Oguchi. Plc-based optical add/drop switch with automatic level control. *Journal Of Lightwave Technology*, 17(12):2562–2571, 1999.

[73] J. W. Goodman, A. R. Dias, and L. M. Woody. Fully parallel, high speed incoherent optical method for performing discrete fourier transforms. *Optics Letters*, 2(1):1–3, 1978.

[74] J. W. Goodman, F. J. Leonberger, F. J. Kung, and R. A. Athale. Optical interconnections for vlsi systems. *Proceeding of the IEEE*, 72(7):850–866, 1984.

[75] A.R. Dias, R.F. Kalman, J.W. Goodman, and A.A. Sawchuk. Fiber-optic crossbar switch with broadcast capability. *Optical Engineering*, 27(11):955–960, 1988.

[76] S. Schmitt-Rink, S. D. S. Chemla, and D. A. B. Miller. Linear and nonlinear optical properties of semiconductor quantum wells. *Advances in Physics*, 38:89–108, 1989.

[77] G. D. Boyd, A. M. Fox, and D. A. B. Miller. 33 ps optical switching of symmetric self-electrooptic effect devices. *Applied Physics Letters*, 57:1843–1845, 1990.

[78] L. M. Loh and J. L. LoCicero. Subnanosecond sampling all-optical analogue-to-digital converter using symmetric self-electro-optic effect devices. *Optical Engineering*, 35(2):457–466, 1996.

[79] F. B. McCormick, F. A. P. Tooley, T. J. Cloonan, J. L. Brubaker, A. L. Lentine, R. L. Morrison, S. J. Hinterlong, M. J. Herron, S. L. Waker, and J. M. Sasian. S-seed based photonic switching network demonstration. In *OSA Proceedings on Photonic Switching*, volume 8, pages 48–55, 1991.

[80] N. Peyghambarian and H. M. Gibbs. Optical bistability for optical signal processing and computing. *Optical Engineering*, 24(1):68–73, 1985.

[81] D. A. B. Miller, D. S. Chemla, T.C. Damen, A. C. Gossard, W. Wiegmann, T. H. Wood, and C. A. Burrus. Novel hybridoptically bistable: the quantum well self-electrooptic effect device. *Applied Physics Letters*, 45(1):13–15, 1984.

[82] W. E. Ross, D. Psaltis, and R. H. Anderson. Two-dimensional magneto-optic spatial light modulator for signal processing. *Optical Engineering*, 22(4):485–491, 1983.

[83] J. A. Davis, S. W. Connely, G. W. Bach, R. A. Lilly, and D. M. Cottrell. Programmable optical interconnections with large fanout capability using the magneto-optic spatial light modulator. *Optics Letters*, 14(1):102–104, 1989.

[84] K. Preston. The membrane light modulator and its applications. *Optica Acta*, 16(5):579, 1969.

[85] D. R. Pape and L. J. Hornbeck. Characteristics of the deformable mirror device for optical information processing. *Optical Engineering*, 22(6):675–681, 1983.

[86] K. M. Johnson, D. J. McKnight, and I. Underwood. Smart spatial light modulators using liquid-crystals on silicon. *IEEE Journal of Quantum Electronics*, 29:699–714, 1993.

[87] J. A. Neff, R. A. Athale, and S. H. Lee. 2-dimensional spatial light modulators: A tutorial. *Proceeding of the IEEE*, 78:826–855, 1990.

[88] N. A. Clark and S. T. Lagerwall. Submicrosecond bistable electrooptic switching in liquid crystals. *Applied Physics Letters*, 36(11):899–901, 1980.

[89] F. Leenhouts and M. Schadt. Optics of twisted nematic and supertwisted menatic liquid-crystal displays. *Journal of Applied Physics*, 60(9):3275–3281, 1986.

[90] L. K. Cotter, T. J. Drabik, R. J. Dillon, and M. A. Handschy. Ferroelectric liquid-crystal silicon integrated circuit spatial light modulator. *Optics Letters*, 15(5):192–293, 1990.

[91] J. W. Goodman. *Introduction to Fourier Optics*. McGraw-Hill, Boston, second edition, 1996.

[92] D. Marcuse. Loss analysis of single-mode fiber splices. *Bell System Technical Journal*, 56:703, 1977.

[93] V. Arrizon and M. Testorf. Efficiency limit of spatially quantized fourier array illuminators. *Optics Letters*, 22(4):197–99, 1997.

[94] H. Dammann. Spectral characteristics of stepped-phase gratings. *Optik*, 53(5):409–417, 1979.

[95] M. Raisi, S. Ahderom, K. Alameh, and K. Eshraghian. Opto-VLSI-based multiband tunable optical filter. *IEE Electronics Letters*, 39:1533–1535, 2003.

[96] Selam Ahderom, Mehrdad Raisi, Kamal Alameh, and Kamran Eshraghian. High-resolution dynamic wdm equalization using opto-vlsi beam processing. In *Proceedings of the 7th World Multiconference on Systemics, Cybernetics and Informatics SCI 2003*, pages 179–183, Orlando, Florida, July 2003.

[97] Mehrdad Raisi, Selam Ahderom, Kamal Alameh, and Kamran Eshraghian. Tunable optical filters employing opto-vlsi processors. In *Proceedings of the International Conference on Computer, Communication and Control Technologies CCCT 2003*, pages 29–34, Orlando, Florida, July 2003.

[98] S. Ahderom, M. Raisi, K. Lo, K. E. Alameh, and R. Mavaddat. Applications of liquid crystal spatial light modulators in optical communications. In *Proceedings of IEEE 5th International Conf. on High-speed Networks and Multimedia Communications, HSNMC'02*, pages 239–242, Korea, July 2002.

[99] J. Turunen and F. Wyrowski, editors. *Diffractive optics for industrial and commercial applications*, chapter Introduction to diffractive optics, pages 1–58. Akademie Verlag, Berlin, 1997.

[100] D. C. Youla and H. Webb. Image restoration by the method of convex projections: Part 1 - theory. *IEEE Transactions on Medical Imaging*, TMI-1:81–94, 1982.

[101] L. G. Gubin, B. T. Polyak, and E. V. Raik. The method of projections for finding the common point of convex sets. *U.S.S.R. Comput. Math. and Phys.*, 7:1–24, 1967.

[102] David Mendlovic, Zeev Zalevsky, Gal Shabtay, and Emanuel Marom. High-efficiency arbitrary array generator. *Applied Optics*, 35(35):6875–6880, December 1996.

[103] R. W. Gerchberg and W. O. Saxton. A practical algorithm for the determination of phase from image and diffraction plane pictures. *Optik*, 35:237–246, 1972.

[104] R. G. Dorsch, A.W. Lohmann, and S. Sinzinger. Fresnel ping-pong algorithm for 2-plane computer-generated hologram display. *Applied Optics*, 33(5):869–875, 1994.

[105] A. Papoulis. A new algorithm in spectral analysis and bandlimited extrapolation. *IEEE Transactions on Circuits and Systems*, CAS-22:735–742, 1975.

[106] Henry Stark, William C. Catino, and Joseph L. LoCicero. Design of phase gratings by generalized projections. *Journal of the Optical Society of America A*, 8(3):566–571, March 1991.

[107] William C. Catino, Joseph L. LoCicero, and Henry Stark. Design of continuous and quantized amplitude holograms by generalized projections. *Journal of the Optical Society of America A*, 15(1):68–76, January 1998.

[108] H. Stark, Y. Y. Yang, and D. Gurkan. Factors affecting convergence in the design of diffractive optics by iterative vector-space methods. *Journal of the Optical Society of America (JOSA A)*, 16(1):149–159, 1999.

[109] H. Stark and Y. Yang. *Vector Space Projections: A Numerical Approach to Signal and Image Processing, Neural Nets, and Optics.* Wiley, New York, 1998.

[110] A. Levi and H. Stark. Image restoration by the method of generalized projections with application to restoration from magnitude. *Journal of the Optical Society of America (JOSA A)*, 1:932–943, 1984.

[111] T. Kotzer, N. Cohen, and J. Shamir. A projection algorithm for consistent and inconsistent constraints. *SIAM Journal of Optimization*, 7(2):527–546, 1997.

[112] T. Kotzer, N. Cohen, and J. Shamir. Generalized projection algorithms with applications to optics and signal restoration. *Optical Communications*, 156(1):77–91, 1998.

[113] R. Aharoni and Y. Censor. Block-iterative projection methods for parallel computation of solutions to convex feasibility problems. *Linear Algebra Application*, 120:165–175, 1989.

[114] F. Wyrowski and O. Bryngdahl. Iterative fourier-transform algorithm applied to computer holography. *Journal of the Optical Society of America (JOSA A)*, 5:1058–1065, 1988.

[115] Frank Wyrowski. Diffractive optical elements: iterative calculation of quantised, blazed phase structures. *Journal of the Optical Society of America A*, 7(6):961–969, June 1990.

[116] M.P. Dames, R.J. Dowling, P. McKnee, and D. Wood. Efficient optical elements to generate intensity weighted spot arrays: design and fabrication. *Applied Optics*, 30(19):2685–2691, July 1991.

[117] N. Yoshikawa, M. Itoh, and T. Yatagai. Quantized phase optimization of two-dimensional fourier kinoforms by a genetic algorithm. *Optics Letters*, 20(7):752–754, April 1995.

[118] F. Wyrowski. Upper bound of the diffraction efficiency of diffractive phase elements. *Optics Letters*, 16(24):1915–1917, 1991.

[119] Optometrics LLC. Telecom grating specifications. Technical report, Ayer, Massachusetts, USA, 2002.

[120] I. G. Manolis, T. D. Wilkinson, M. M. Redmond, and W. A. Crossland. Reconfigurable multilevel phase holograms for optical switches. *IEEE Photonics Technology Letters*, 14(6):801–803, 2002.

[121] Boulder Nonlinear Systems Inc. 128×128 analog spatial light modulator users manual. Lafayette Colorado USA.

Appendix A

Dammann analysis

The stepped phase approximation of a blazed grating in a diffractive phase element (DPE) is shown in Fig. A.1:

The above infinite grating structure may be described mathematically as:

$$f(x) = \sum_{m=-\infty}^{\infty} \exp\left(j\frac{2\pi}{M}m\right) rect\left(\frac{x}{x_o} - mx_o\right) \tag{A.1}$$

where

$$rect\left(\frac{x}{x_o}\right) = \begin{cases} 1 for\, |x| \leq \frac{x_o}{2} \\ 0 for\, |x| > \frac{x_o}{2} \end{cases} \tag{A.2}$$

From fourier series, we know that

$$f(x) = \sum_{n=-\infty}^{\infty} c_n \exp\left(j\frac{\pi n x}{L}\right) \tag{A.3}$$

where

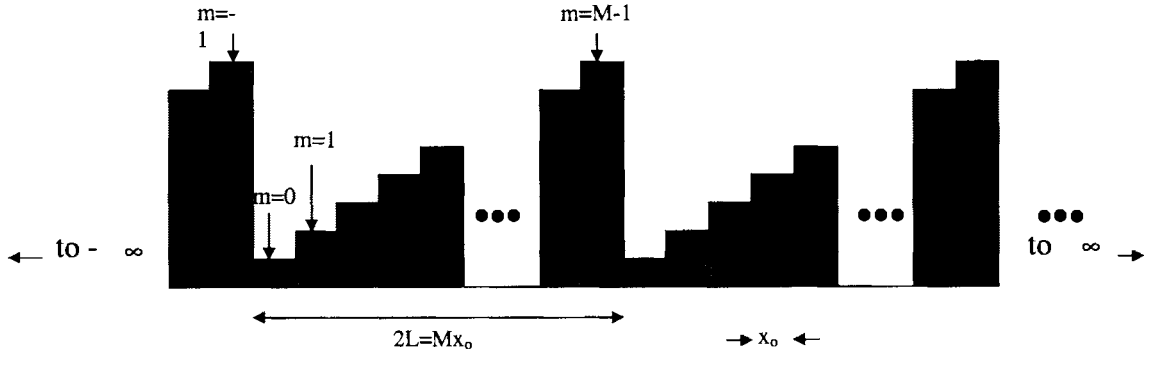

Figure A.1: Infinite stepped-blaze grating

$$c_n = \frac{1}{2L} \int_{c}^{c+2L} f(x) \exp\left(-j\frac{\pi n x}{L}\right) dx \tag{A.4}$$

We can express c_n as

$$c_n = \sum_{m=0}^{M-1} c_{nm} \tag{A.5}$$

where

$$c_{nm} = \frac{1}{Mx_o} \int_{mx_o}^{(m+1)x_o} \exp\left(j\frac{2\pi}{M}m\right) \exp\left(-j\frac{\pi n x}{L}\right) dx \tag{A.6}$$

Computing the value of c_{nm} we get

$$c_{nm} = \exp\left(j\frac{2\pi m}{M}(1-n)\right) \exp\left(-j\frac{2\pi n}{M}\right) \sin\left(\frac{\pi n}{M}\right) \tag{A.7}$$

Then, summing the c_{nm} coefficients, we get

$$c_n = \sum_{m=0}^{M-1} c_{nm} = \frac{\sin\left(\frac{\pi n}{M}\right)}{\pi n} \exp\left(-j\pi\left(n + \frac{1}{M}\right)\right) \frac{\sin(\pi n)}{\sin\left(\pi\frac{n-1}{M}\right)} \tag{A.8}$$

From c_n we can estimate the proportion of average power arriving at spatial frequency $\frac{\pi n}{Mx_o}$

$$\eta_n = |c_n|^2 = \frac{\sin^2\left(\frac{\pi n}{M}\right)}{\left(\frac{\pi n}{M}\right)^2} \frac{\sin^2(\pi n)}{M^2 \sin^2\left(\pi\frac{n-1}{M}\right)} \tag{A.9}$$

We can consider the above expression as being made up of two function:

$$\eta_n = A(M,n)B(M,n) = \frac{\sin^2(\pi n)}{M^2 \sin^2\left(\pi\frac{n-1}{M}\right)} \tag{A.10}$$

where

$$A(M,n) = \mathrm{sinc}^2\left(\frac{\pi n}{M}\right) \tag{A.11}$$

and

$$B(M,n) = \frac{\sin^2(\pi n)}{M^2 \sin^2\left(\pi\frac{n-1}{M}\right)} \tag{A.12}$$

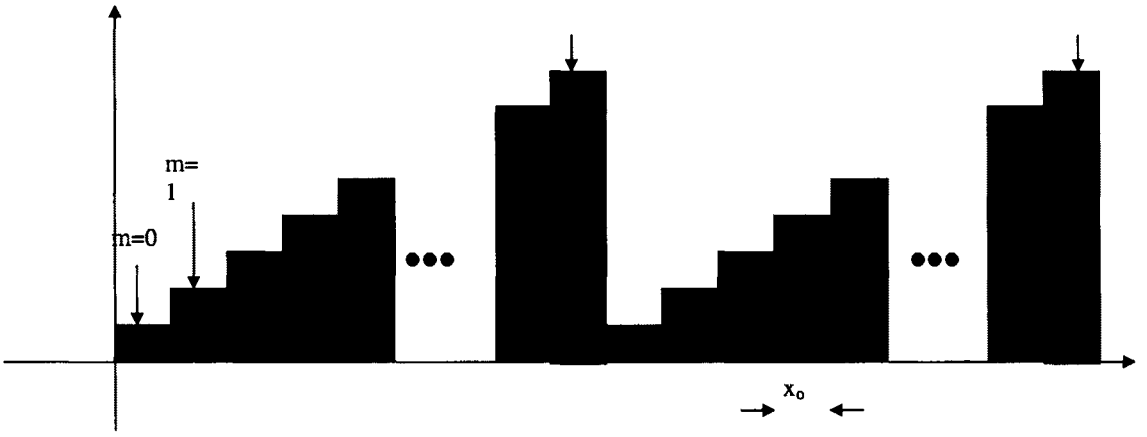

Figure A.2: Finite aperture stepped-blaze grating

Since the numerator of $B(M,n)$ is zero for all values of n, while the denominator is zero when $n-1$ is a multiple of M. Therefore, $B(M,n)$ is always zero, except when $n-1=gM$ or $n=gM+1$ for any integer g. For this case, we can write $B(M,n)$ as

$$B(M,n)=\frac{\sin^2(\pi gM+\pi)}{M^2\sin^2\left(\pi\frac{gM}{M}\right)}=\frac{\sin^2(\pi gM)}{M^2\sin^2(\pi g)}=\lim_{g\to 0}\frac{(\pi gM)^2}{M^2(\pi g)^2}=1 \tag{A.13}$$

Therefore, for we may express the efficiency as

$$\eta_n=\mathrm{sinc}^2\left(\frac{\pi n}{M}\right) \tag{A.14}$$

where $n=gM+1$.

A.1 Calculation of Replay Field for Stepped Blazed Grating of Finite Aperture

The replay field for stepped blazed grating structure of finite aperture will be somewhat different. Figure A.2 shows the structure of a finite aperture stepped-blazed grating.

The finite aperture grating structure may be described mathematically as:

$$f(x)=\sum_{m=0}^{K-1}\exp\left(j\frac{2\pi}{M}m\right)rect\left(\frac{x}{x_o}-mx_o\right) \tag{A.15}$$

where

$$rect\left(\frac{x}{x_o}\right) = \begin{cases} 1 for\,|x| \leq \frac{x_o}{2} \\ 0 for\,|x| > \frac{x_o}{2} \end{cases} \tag{A.16}$$

The fourier transform of the above may be represented as

$$F(u) = \int_0^{Kx_o} f(x)\exp\left(-j2\pi ux\right)dx = \sum_{m=0}^{K-1}\int_{mx_o}^{(m+1)x_o} \exp\left(j\frac{2\pi}{M}m\right)\exp\left(-j2\pi ux\right)dx \tag{A.17}$$

The above relation may be evaluated to get

$$F(u) = \exp\left(j\pi\frac{K}{M}\left(1 - ux_oM - \frac{1}{K}\right)\right)\frac{\sin\left(\pi ux_o\right)}{\pi u}\frac{\sin\left(\pi\left(\frac{1}{M} - ux_o\right)K\right)}{\sin\left(\pi\left(\frac{1}{M} - ux_o\right)\right)} \tag{A.18}$$

Since we are interested in mainly the intensity profile, we can represent it as

$$I(u) = |F(u)|^2 = \frac{\sin^2\left(\pi ux_o\right)}{\left(\pi u\right)^2}\frac{\sin^2\left(\pi\left(\frac{1}{M} - ux_o\right)K\right)}{\sin^2\left(\pi\left(\frac{1}{M} - ux_o\right)\right)} \tag{A.19}$$

Appendix B

Derivation of the Rayleigh-Sommerfeld diffraction relation

Below, we derive the scalar diffraction relation, following the treatment of Goodman [91]. The starting point for the analysis of all electro-magnetic radiation is, of course, Maxwell's equations. In the absence of free charges, the equations are:

$$\nabla \times \vec{E} = -\mu \frac{\partial \vec{H}}{\partial t} \tag{B.1}$$

$$\nabla \times \vec{H} = \varepsilon \frac{\partial \vec{E}}{\partial t} \tag{B.2}$$

$$\nabla \cdot \varepsilon \vec{E} = 0 \tag{B.3}$$

$$\nabla \cdot \mu \vec{H} = 0 \tag{B.4}$$

where $\vec{E}$ is the electric field, $\vec{H}$ is the magnetic field, μ is the magnetic permeability of the material, and ε is the electric permittivity. For most optical systems, further assumptions can be made to simplify Maxwell's equations:

- The permittivity ε of the medium is constant in the region of interest, and independent of the wavelength of the light,

- The medium is non-magnetic, i.e., $\mu = \mu_o$ the permeability of free-space.

If the above conditions hold true, we can use the vector identity to simplify the above relations:

$$\nabla \times \left(\nabla \times \vec{E}\right) = \nabla \left(\nabla \cdot \vec{E}\right) - \nabla^2 \vec{E} \tag{B.5}$$

Substituting Maxwell's equations, we get:

$$\begin{aligned} \nabla \times \left(\nabla \times \vec{E}\right) &= \nabla \times \left(-\mu_o \frac{\partial \vec{H}}{\partial t}\right) \\ &= -\mu_o \frac{\partial}{\partial t}\left(\nabla \times \vec{H}\right) \\ &= -\mu_o \frac{\partial}{\partial t}\left(\varepsilon \frac{\partial \vec{E}}{\partial t}\right) \\ &= -\mu_o \varepsilon \frac{\partial^2 \vec{E}}{\partial t^2} \end{aligned} \tag{B.6}$$

Likewise, for the right hand side, we get:

$$\nabla \left(\nabla \cdot \vec{E}\right) - \nabla^2 \vec{E} = \nabla (0) - \nabla^2 \vec{E} = -\nabla^2 \vec{E} \tag{B.7}$$

Thus, we get the differential equation:

$$\nabla^2 \vec{E} - \frac{n^2}{c^2} \frac{\partial^2 \vec{E}}{\partial t^2} = 0 \tag{B.8}$$

where the index of refraction $n = \left(\frac{\varepsilon}{\varepsilon_o}\right)^{\frac{1}{2}}$ is a relative measure of the permittivity, and the speed of light is expressed as $c = \frac{1}{\sqrt{\mu_o \varepsilon_o}}$. An identical relation is found for the magnetic field $\vec{H}$ since Maxwell's equations as described above are symmetric with respect to the electric and magnetic field.

Scalar diffraction theory takes advantage of the fact that, in the above equation, there is no coupling between the components of $\vec{E}$ and $\vec{H}$. That is E_x , E_y , E_z , H_x , H_y, and H_z all individual satisfy the equation. Therefore, we replace the vectors $\vec{E}$ and $\vec{H}$ with a single scalar wave equation:

$$\nabla^2 u(P,t) - \frac{n^2}{c^2} \frac{\partial^2 u(P,t)}{\partial t^2} = 0 \tag{B.9}$$

where $u(P,t)$ is dependent only on position P, and time t. A class of solutions to the above wave equation are of the form:

$$u(P,t) = A(P) \cos\left(2\pi\nu t + \phi(P)\right) \tag{B.10}$$

To get a simpler form of the wave equation, we write the solution $u(P,t)$ in complex form:

$$u(P,t) = \mathrm{Re}\left[U(P)\exp\left(-j2\pi\nu t\right)\right] \tag{B.11}$$

where $U(P)$ is the complex amplitude, excluding the time varying component. Since the time dependence is a simple exponential, and is the same for all waves (of the same frequency), the wave equation for a monochromatic wave can simply be described as:

$$\left(\nabla^2 + k^2\right)U = 0 \tag{B.12}$$

where $k = 2\pi n\frac{\nu}{c} = \frac{2\pi}{\lambda}$.

The last relation, which is the basis of the current study, is the most widely used form of the scalar wave equation, and is generally known as the Helmholtz equation.

In order to calculate the propagation of the scalar field $U(P)$ at some distance from its known boundary values, we utilize Green's theorem, which states for any two functions U and G:

$$\int\int\int_V \left(U\nabla^2 G - G\nabla^2 U\right)dv = \int\int_S \left(U\frac{\partial G}{\partial n} - G\frac{\partial U}{\partial n}\right)ds \tag{B.13}$$

where S is the surface surrounding the volume V, and $\frac{\partial}{\partial n}$ refers to the partial derivative in the direction, $\vec{n}$, normal to the surface S. We choose a surface S to give us an aperture that we wish to propagate in the manner shown in Fig. B.1.

As can be seen from Fig. B.1, the surface in consideration is the sum of the inner and outer surfaces:

$$S = S_1 + S_2 + S_\varepsilon \tag{B.14}$$

If the auxiliary function G is made to satisfy the Helmholtz wave equation, then the left hand side of Green's theorem will vanish:

$$\int\int\int_V \left(U\nabla^2 G - G\nabla^2 U\right)dv = \int\int\int_V \left(UGk^2 - Gk^2 U\right)dv = 0 \tag{B.15}$$

Thus, Green's theorem becomes

$$-\int\int_{S_\varepsilon}\left(U\frac{\partial G}{\partial n} - G\frac{\partial U}{\partial n}\right)ds = \int\int_{S_1+S_2}\left(U\frac{\partial G}{\partial n} - G\frac{\partial U}{\partial n}\right)ds \tag{B.16}$$

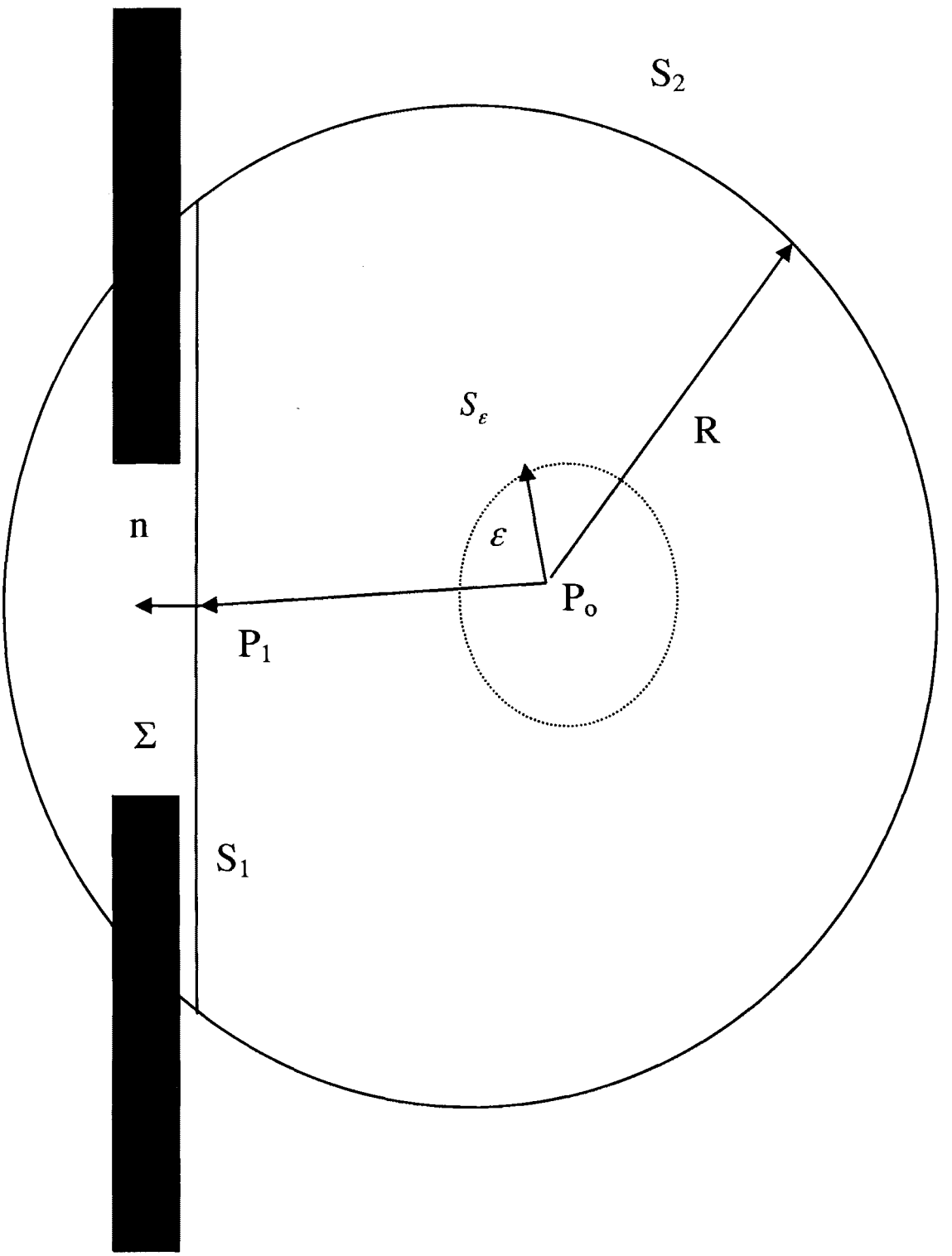

Figure B.1: Sphere for evaluation of Green's theorem

We carefully chose the auxiliary function G, to allow us to express the propagation of the electromagnetic disturbance from the hole in the screen screen Σ at point P_o. Of the several possible auxiliary functions, we choose the first Rayleigh-Sommerfeld function:

$$G = \frac{\exp(jkr_{01})}{r_{01}} - \frac{\exp(jk\tilde{r}_{01})}{\tilde{r}_{01}} \tag{B.17}$$

where r_{01} is the distance from the point P_0 to a point P_1 on the imaginary surface, and $\tilde{r}_{01}$ is the distance from a second point $\tilde{P}_0$, which is located at the mirror image of point P_0 across the screen Σ. The two contributions to G are exactly out of phase (hence the negative sign). We can then evaluate the derivative of G with respect to the normal:

$$\frac{\partial G}{\partial n} = 2\cos(\vec{n}, \vec{r}_{01})\left(jk - \frac{1}{r_{01}}\right)\frac{\exp(jkr_{01})}{r_{01}} \tag{B.18}$$

where $\cos(\vec{n}, \vec{r}_{01})$ is the cosine of the angle between the normal vector $\vec{n}$ and the distance vector$\vec{r}_{01}$. Specifically, for the case of the surface S_ε, we find that

$$G = \frac{\exp(jk\varepsilon)}{\varepsilon} - \frac{\exp(jk\tilde{r}_{01})}{\tilde{r}_{01}} \tag{B.19}$$

and noting that the normal vector $\vec{n}$ and $\vec{r}_{01}$ are in the opposite directions (the cosine term will have a -1 value), and further, noting that the value of $\tilde{r}_{01}$ will not vary appreciably across S_ε if ε is made arbitrarily small, we write

$$\lim_{\varepsilon\to 0}\int\int_{S_\varepsilon}\left(U\frac{\partial G}{\partial n} - G\frac{\partial U}{\partial n}\right) = \lim_{\varepsilon\to 0} 4\pi\varepsilon^2\left(U\frac{\exp(jk\varepsilon)}{\varepsilon}\left(\frac{1}{\varepsilon} - jk\right) - \left(\frac{\exp(jk\varepsilon)}{\varepsilon} - \frac{\exp(jk\tilde{r}_{01})}{\tilde{r}_{01}}\right)\frac{\partial U}{\partial n}\right) \tag{B.20}$$

$$= \lim_{\varepsilon\to 0} 4\pi\varepsilon^2\left(U\frac{\exp(jk\varepsilon)}{\varepsilon^2} - \left(\frac{\exp(jk\varepsilon)}{\varepsilon} - \frac{\exp(jk\tilde{r}_{01})}{\tilde{r}_{01}}\right)(0)\right) \tag{B.21}$$

$$= 4\pi U \tag{B.22}$$

Further, if we let the radius of the surface S_2 go to infinity, i.e. $R \to \infty$, and if $r_{01} \gg \lambda$, it can be shown that the integral over S_2 will also vanish, on the condition that the following requirement is met:

$$\lim_{R\to\infty} R\left(\frac{\partial U}{\partial n} - jkU\right) = 0 \tag{B.23}$$

The above requirement, generally known as the Sommerfeld radiation condition, simply requires that the value of U in S_2, for $R \rightarrow \infty$, diminish just as fast as a spherical diverging wave at P_o. In other words, there should be no additional external sources of light.

Combining Eq. (B.16) - (B.20), we find that

$$U(P_o) = \frac{1}{4\pi} \int\int_{S_1} \left(\frac{\partial U}{\partial n} G - U \frac{\partial G}{\partial n} \right) ds \tag{B.24}$$

Since G is clearly zero at all points on S_1, and using the results of Eq. (B.18), we get

$$U(P_o) = \frac{1}{j\lambda} \int\int_{S_1} U(P_1) \frac{e^{jkr_{01}}}{r_{01}} \cos(\vec{n}, \vec{r}_{01})\, ds \tag{B.25}$$

Since the screen corresponding to S_1 will absorb all the light except at the aperture Σ, we can rewrite Eq. (B.25) as

$$U(P_o) = \frac{1}{j\lambda} \int\int_{\Sigma} U(P_1) \frac{e^{jkr_{01}}}{r_{01}} \cos(\vec{n}, \vec{r}_{01})\, ds \tag{B.26}$$

The above the the desired Rayleigh-Sommerfeld diffraction relation.

Appendix C

Derivation of Theoretical Diffraction Efficiency relation

We derive below the general analysis by Wyrowski [118], who developed a method for determination of efficiency irrespective of the holographic phase profile.

The OVP essentially modifies the phase profile of a beam of light, in such a way as to effect a particular beam profile at the observation plane. If we consider $f(x)$ as the desired beam, and $g(x)$ as the actual beam at the output plane, we desire:

$$g(x) = \alpha f(x) \tag{C.1}$$

However, since the OVP can modify only the phase, and only in a pixellated array with limited phase levels, it will probably be impossible to satisfy the above relation on the entire observation plane. Therefore, we say that the above relation hold only at limited area of $x \in \Re$, which is known as the "signal window". The hologram needed to produce the normalized desired signal can be found simply from a fourier transform.

$$F(u) = \Im f(x) \tag{C.2}$$

In general, $F(u)$ cannot be realized in an OVP. Therefore, a coding algorithm will have to be defined to map $F(u)$ to the OVP. Therefore the discretized realizable phase distribution, $G(u)$, may be expressed as:

$$G(u) = F(u) + C(u) \tag{C.3}$$

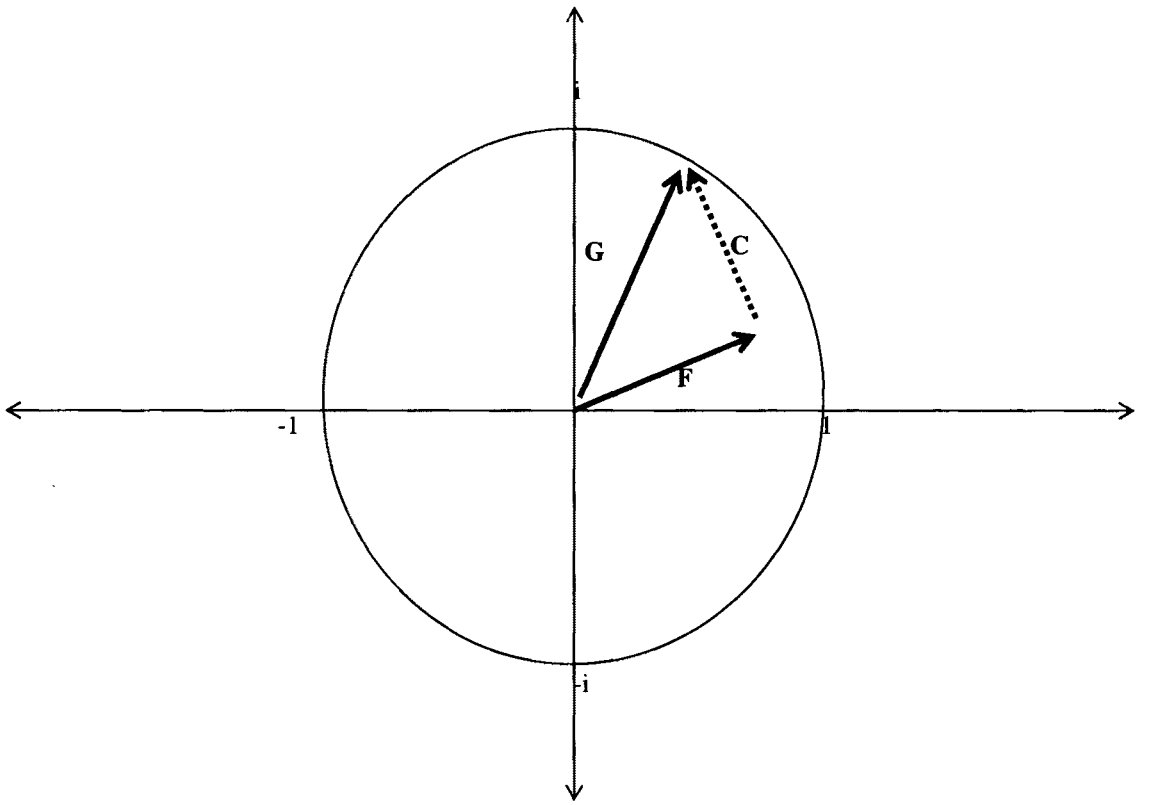

Figure C.1: Relationship between G, F, and C on the complex plane

where $C(u)$ is the quantization coding. If we assume that $|F(u)| \leq 1$, then we can visualize the coding algorithm as mapping $F(u)$ to the unit circle on the complex plane, since the SLM only modifies the phase and has unit amplitude as seen in Fig. C.1.

At the observation plane, this can be expressed as:

$$g(x) = f(x) + c(x) \tag{C.4}$$

The coding algorithm is chosen such that it allows the value of $c(x)$ to be proportional to $f(x)$ at the region $x \in \Re$, then we can ensure that there is no signal noise in that window. In other words, we can express $c(x)$ such that:

$$c(x) = (\alpha - 1)f(x) + \hat{c}(x) \tag{C.5}$$

where $\hat{c}(x) = 0$ in the region $x \in \Re$. We can then formulate $g(x)$ as:

$$g(x) = \alpha f(x) + \hat{c}(x) \tag{C.6}$$

Assuming that the incident wave has a normalized energy, the diffraction efficiency can be formulated as:

$$\eta = \int_{\Re} g(x)dx = \alpha^2 \int_{\Re} |f(x)|^2 \, dx \tag{C.7}$$

If we assume, without loss of generality, that $f(x)$ lies completely within $\Re$, then we can write, recalling Parceval's relation, Eq. (C.7) as:

$$\eta = \alpha^2 \int_{-\infty}^{\infty} |f(x)|^2 \, dx = \alpha^2 \int_{-\infty}^{\infty} |F(u)|^2 \, du \tag{C.8}$$

By integrating both sides of Eq. (C.6) we get:

$$\int |g(x)|^2 \, dx = \alpha^2 \int |f(x)|^2 \, dx + \int |\hat{c}(x)|^2 \, dx \tag{C.9}$$

Therefore, using Parceval's relation again, we get:

$$\int |G(u)|^2 \, du = \alpha^2 \int |F(u)|^2 \, du + \int \left|\hat{C}(u)\right|^2 du \tag{C.10}$$

Since $G(u)$ is a phase only hologram, $|G(u)| = 1$. Taking the Fourier transform of Eq. (C.6) and using the unit circle geometry for $\hat{C}$, $G(u)$ and $F(u)$, in a manner analogous to Fig. C.1, we get:

$$\int \left|C\hat{(u)}\right|^2 du = 1 - \alpha^2 \int |F(u)|^2 \, du \tag{C.11}$$

and

$$\int \left|C\hat{(u)}\right|^2 du = 1 + \alpha^2 \int |F(u)|^2 \, du + \int |F(u)| \cos\phi du \tag{C.12}$$

where ϕ is the angle between G and F. Combining Eqs. (C.11) and (C.12), we get:

$$\alpha = \frac{\int |F(u)| \cos\phi du}{\int |F(u)|^2 \, du} \tag{C.13}$$

In Eq. (C.13), the value of α is maximum when $\phi = 0$. Therefore, we note by considering Eq. (C.8) that the maximum diffraction will be given when α is at its maximum. Combining Eqs. (C.13) and (C.8) we get the upper limit for the diffraction efficiency η is

$$\eta = \frac{\left|\int F(u)du\right|^2}{\int |F(u)|^2 \, du} \tag{C.14}$$

The above result allows us to determine the maximum theoretical efficiency solely on the shape of the diffracted pattern desired *irrespective of the hologram used.* For the case of beam steering, the output desired is of course $f(x) = \delta(x - x_o)$, a delta function. Therefore, using Eq. (C.14), the maximum efficiency for such a hologram is 100%.

The above result is important, in that it allows us to determine, for our beam steering case, that the only source of loss from the hologram will be coding errors $c(x)$, i.e the only diffraction efficiency loss will result from the algorithms used to code the desired pattern.

Appendix D

Calculation of Gaussian beam center from optical intensity at any three detectors

To identify the center of the Gaussian beam falling on the two SLMs, it is possible to perform a calculation on the position and intensities of any three detectors on each SLM. The positions and number of the detectors can vary based on the sensitivity of the detectors and the size of the Gaussian beam relative to the size of the Hologram. Figure D.1 shows the layout considered for an arbitrarily positioned Gaussian beam.

The Gaussian beam intensity in the above coordinate system is given by:

$$I(x,y) = I_m e^{-\frac{(x-x_m)^2+(y-y_m)^2}{w^2}} \tag{D.1}$$

Therefore,

$$I_1 = I_m e^{-\frac{(x_1-x_m)^2+(y_1-y_m)^2}{w^2}} \; I_2 = I_m e^{-\frac{(x_1-x_m)^2+(y_1-y_m)^2}{w^2}} \; I_3 = I_m e^{-\frac{(x_1-x_m)^2+(y_1-y_m)^2}{w^2}} \tag{D.2}$$

Re-arranging the terms, we get:

$$\begin{aligned} -\frac{(x_1-x_m)^2+(y_1-y_m)^2}{w^2} &= \ln\left(\frac{I_m}{I_1}\right) - \frac{(x_2-x_m)^2+(y_2-y_m)^2}{w^2} \\ &= \ln\left(\frac{I_m}{I_2}\right) - \frac{(x_3-x_m)^2+(y_3-y_m)^2}{w^2} = \ln\left(\frac{I_m}{I_3}\right) \end{aligned} \tag{D.3}$$

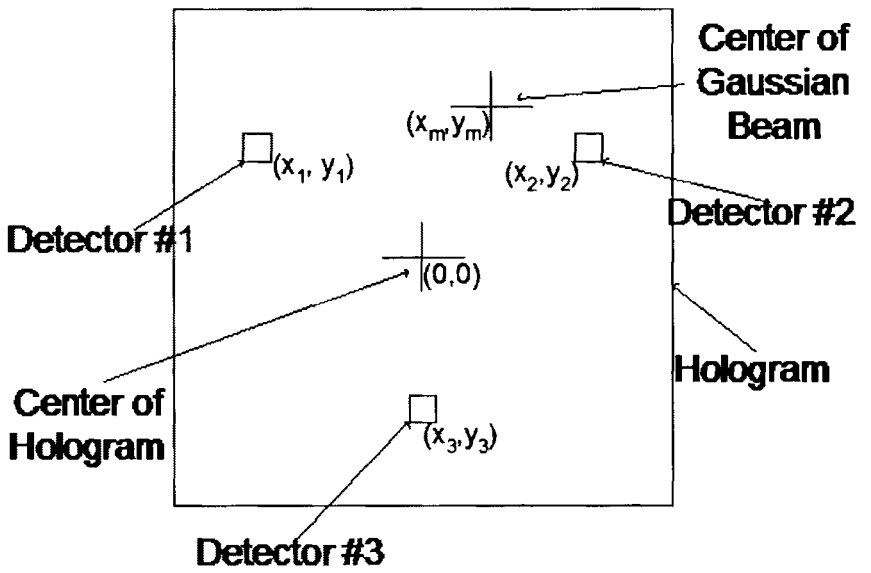

Figure D.1: Layout of an arbitrarily positioned Gaussian beam with three detectors

Using the above three equations, we can eliminate I_m and y_m and solve for x_m. After some algebra, we get:

$$x_m = \frac{w^2\left(y_1 \ln\left(\frac{I_3}{I_2}\right) + y_2 \ln\left(\frac{I_1}{I_3}\right) + y_3 \ln\left(\frac{I_2}{I_1}\right)\right)}{2\left(y_1\left(x_3 - x_2\right) + y_2\left(x_1 - x_3\right) + y_3\left(x_2 - x_1\right)\right)} + \frac{y_1\left(x_3^2 + y_3^2 - x_2^2 + y_2^2\right) + y_2\left(x_1^2 + y_1^2 - x_3^2 + y_3^2\right) + y_3\left(x_2^2 + y_2^2 - x_1^2 + y_1^2\right)}{2\left(y_1\left(x_3 - x_2\right) + y_2\left(x_1 - x_3\right) + y_3\left(x_2 - x_1\right)\right)} \quad \text{(D.4)}$$

By orthogonal symmetry, we get a similar relation for y_m :

$$y_m = \frac{w^2\left(x_1 \ln\left(\frac{I_3}{I_2}\right) + x_2 \ln\left(\frac{I_1}{I_3}\right) + x_3 \ln\left(\frac{I_2}{I_1}\right)\right)}{2\left(x_1\left(y_3 - y_2\right) + x_2\left(y_1 - y_3\right) + x_3\left(y_2 - y_1\right)\right)} + \frac{x_1\left(y_3^2 + x_3^2 - y_2^2 + x_2^2\right) + x_2\left(y_1^2 + x_1^2 - y_3^2 + x_3^2\right) + x_3\left(y_2^2 + x_2^2 - y_1^2 + x_1^2\right)}{2\left(x_1\left(y_3 - y_2\right) + x_2\left(y_1 - y_3\right) + x_3\left(y_2 - y_1\right)\right)} \quad \text{(D.5)}$$

The above results are correct for any three detectors. However, they are very large and clumsy. Therefore, we will choose symmetrical positions for the detector positions, which will simply the relations. Three representative setups are considered. The first is a "Y" shaped configuration, where the three detectors are equidistant from the origin, as well as even angular distribution (120 degrees between adjacent detectors). The second is square shaped, with the detectors are the corners of the square, and the center of the square at the origin of the coordinate system. The third configuration is "diamond" shaped, with two detectors on each axis, all equidistant from the origin.

D.1 Detectors in "Y" shaped configuration

Figure D.2 shows the three detectors arranged in a "Y" configuration. In such a setup, the pixels can be arranged such that $x_1^2 + y_1^2 = x_2^2 + y_2^2 = x_3^2 + y_3^2$. Further, we can set the positions such that $x_2 = -x_1 \approx 0.866r$, $x_3 = 0$, $y_1 = y_2 = 0.5r$, and $y_3 = -r$. This will simplify the relations in the following manner:

$$x_m = \frac{w^2}{6r\left(0.866\right)} \ln\left(\frac{I_2}{I_1}\right) \quad \text{(D.6)}$$

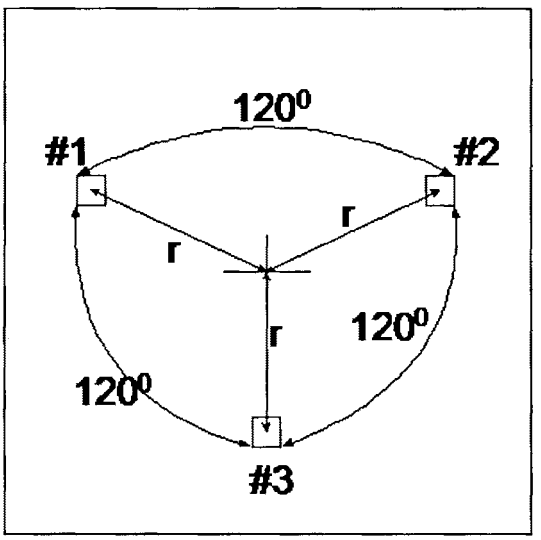

Figure D.2: Layout of an arbitrarily positioned Gaussian beam with three detectors

and

$$y_m = \frac{w^2}{6r} \ln\left(\frac{I_1 I_2}{I_3^2}\right) \tag{D.7}$$

D.2 Detectors in square configuration

Figure D.3 shows the detectors arranged in a square configuration. In such a configuration, the following relation still holds: $x_1^2 + y_1^2 = x_2^2 + y_2^2 = x_3^2 + y_3^2$. Further, we define $-x_1 = x_2 = -x_3 = y_1 = y_2 = -y_3 = a$. The resulting relations will be:

$$x_m = \frac{w^2}{2a} \ln\left(\frac{I_2}{I_1}\right) \tag{D.8}$$

and

$$y_m = \frac{w^2}{2a} \ln\left(\frac{I_1}{I_3}\right) \tag{D.9}$$

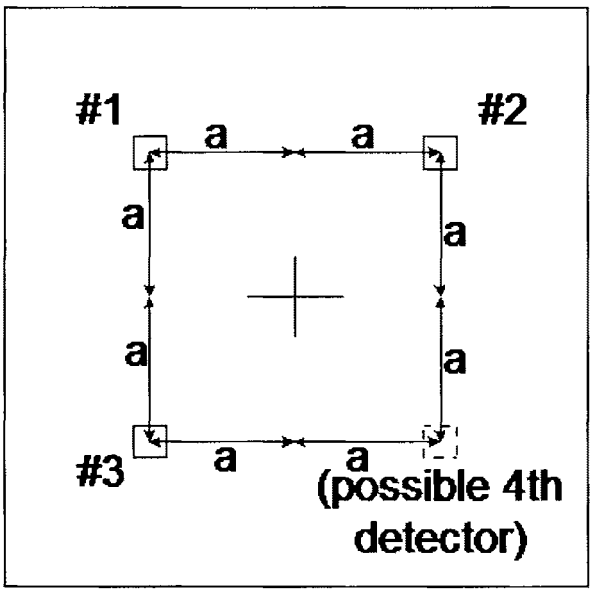

Figure D.3: Layout of an arbitrarily positioned Gaussian beam with three detectors

For the sake of symmetry, it may be preferable to have four detectors per hologram in such a configuration.

D.3 Detectors in "diamond" configuration

The diamond configuration is shown in Fig. D.4. As in the other configurations, this one also dictates that $x_1^2+y_1^2 = x_2^2+y_2^2 = x_3^2+y_3^2$. Further, we can set $-x_1 = x_3 = y_2 = -y_4 = r$ and $y_1 = y_3 = x_2 = x_4 = 0$. The resulting relations will then be:

$$x_m = \frac{w^2}{4r} \ln\left(\frac{I_3}{I_1}\right) \tag{D.10}$$

and

$$y_m = \frac{w^2}{4r} \ln\left(\frac{I_2}{I_4}\right) \tag{D.11}$$

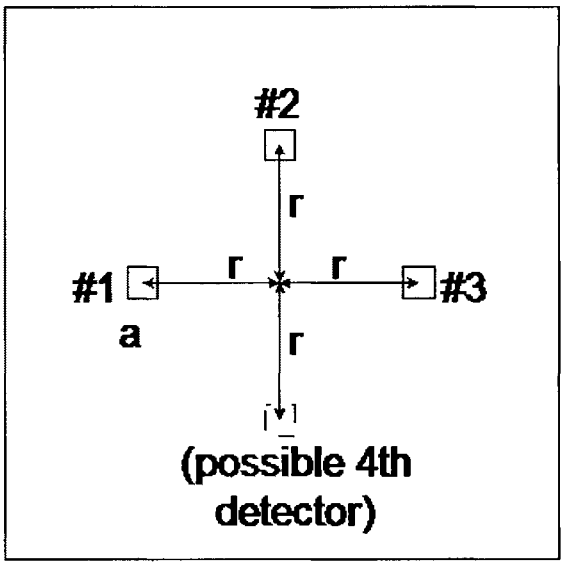

Figure D.4: Layout of an arbitrarily positioned Gaussian beam with three detectors

D.4 Conclusions

We described above three different configurations for detecting the center of the incident beam with respect to the center of the intended hologram, which can then be corrected by adjusting accordingly the steering angle of the holograms displayed. All three configurations seem to offer realizable simple solutions. However, the last "diamond" configuration, seems the easiest to implement.

Appendix E

Opto-VLSI processor specifications

Number of Pixels	16,384 (128 × 128)
Array Size	5.12 mm × 5.12 mm
Pixel Pitch	40μm
Flat Fill Factor	60%
Contrast	200:1
Modulation Uniformity	$\lambda/8$ or better
Optical Modulation	w/ FLC: variable polarization rotation w/ NLC: variable retardation change
Full Frame Loading	102.4μs
Optical Response (10%-90%)	w/ FLC: 50-150 μs w/ NLC: 0.2-1ms rise and 1-10 ms fall times - Depends on wavelength and temperature
Maximum Usable Frame Rate	$1/2(load + response + view)$ w/ FLC: 1627 Hz, load = 102.4μs response = 102.4μs view = 102.4μs w/ NLC: 300 Hz (at elevated temperature)
Electrical Addressing	16 8-bit DACs
Device Configuration	Reflective
Driver Memory	256 frames of SRAM, randomly selectable
Driver Interfaces	Full-length ISA-bus computer slot Dalsa CA-D1-0128A 736-Hz 8-bit camera port 32-bit external data-port loads full frame in 204.8μs Laser modulation signal Detector synchronization signal

Source: Boulder Nonlinear Inc., Boulder, Colorado, USA [121].

Appendix F

Definition of Terms and Abbreviations

CMOS (Complementary Metal Oxide Silicon circuits): Electronic circuit architecture, consisting of two complementary types of field effect transistors, in such a way that when one set of switches are on, the other set will turn off. CMOS circuits are typically used in VLSI systems.

Cross-talk Isolation: In optical switches, a measure of isolation from unintended signals (possibly adjacent signal paths) which add noise to the output port under investigation. Usually measured in decibels of the ratio of intended light intensity vs. the unintended "cross-talk" signal strength.

Dead-space: In a spatial light modulator, space between pixels which cannot be modulated.

Diffraction Efficiency: The efficiency of a diffractive optical element (such as a hologram) in steering a beam to a specified direction. Also measured in decibels, as a ratio of the optical power in the steered beam and the original beam.

Fiber, optical: An optical cable that can transmit light signals with little loss of energy over long distances by confining the light to a small area. Typically made of silica.

Holographic Systems, Holography: Any method of modifying the phase profile of a light beam propagating in free space.

Optical Axis: An imaginary line that connects the centers of the lens configuration in linear optical systems. The region around the optical axis, known as "paraxial" region, under certain circumstances exhibits characteristics of linear systems.

Opto-Electronic Systems: Any system that combines optical and electronic devices into a single system.

Opto-VLSI Processor (OVP): A class of spatially distributed phase modulators, which are controlled by a VLSI circuit. See also spatial light modulators.

Opto-VLSI Systems: A class of opto-electronic systems, integrating the great computing capacity of silicon VLSI technology, with integrated optical processing devices.

Pixel: In spatial light modulators, the unit building block that can modulate the wave characteristics of light impinging on it.

Spatial Light Modulators (SLMs): Devices consisting of a large number of independently controllable light modulating pixels, which, as a whole, can act as a holographic plate.

Very Large Scale Integrated Circuits (VLSI): Integrated circuit technology consisting of a massive number of circuit elements on a single silicon die. VLSI systems typically use CMOS technology for creating complex digital logic circuits as well as analog information processors.